Proton-Antiproton Annihilation at Rest into $\pi^0 K_L K_L$

Inaugural Dissertation

zur Erlangung der philosophischen Doktorwürde

vorgelegt der

Philosophischen Fakultät II

der

Universität Zürich

von

Sven von Dombrowski

aus Baden

begutachtet von Prof. Dr. Claude Amsler

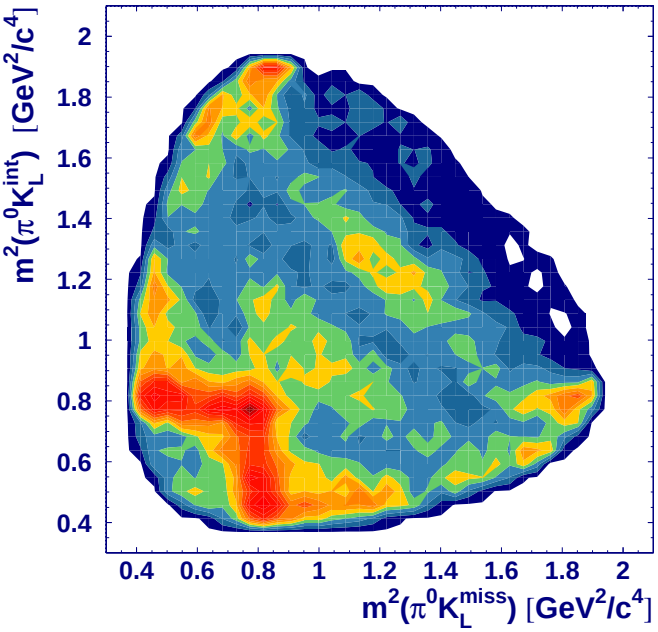

Zürich 1995

Abstract

The aim of this thesis was to search for the $f_0(1370)$ and $f_0(1500)$ mesons decaying into $K\overline{K}$ with high statistics data from the Crystal Barrel experiment at LEAR. These states have recently been discovered by the Crystal Barrel Collaboration in $\overline{p}p \to \pi^0\pi^0\pi^0$, $\pi^0\eta\eta$, and $\pi^0\eta\eta'$. It is believed that the $f_0(1500)$ is the scalar groundstate glueball mixed with nearby $q\overline{q}$ states.

The final state $\pi^0 K_L K_L$ from $\overline{p}p$ annihilation at rest in liquid hydrogen was reconstructed and analysed. The data selection required a reconstructed $\pi^0 \to \gamma\gamma$, a missing K_L and an interacting K_L for which the emission angle was measured by the CsI calorimeter. With this information it was possible to reconstruct the complete kinematics. About 37,000 $\pi^0 K_L K_L$ events have been selected which correspond to about 100 times the statistics of previous bubble chamber experiments. A partial wave analysis has been performed assuming $\overline{p}p$ annihilation from the $^1S_0$ $\overline{p}p$ initial state. The partial waves were parametrized by means of the K-matrix formalism in order to preserve unitarity for overlapping resonances of the same quantum numbers. The helicity formalism was used to calculate decay angular distributions.

The result of this analysis is the observation of two scalar resonances decaying into $K\overline{K}$. The first resonance has a mass of (1515 ± 12) MeV/c^2 and a width of (104 ± 12) MeV/c^2. These values agree with those of the $f_0(1500)$. One then finds a branching ratio of

$$B(\overline{p}p \to \pi^0 f_0(1500) \to \pi^0 K\overline{K}) \quad = \quad (5.0 \pm 0.5) \times 10^{-4}$$

from which the relative coupling

$$\frac{\gamma^2(f_0(1500) \to K\overline{K})}{\gamma^2(f_0(1500) \to \pi\pi)} \quad = \quad 0.24 \pm 0.09$$

can be deduced. Hence, $f_0(1500)$ is not the scalar $s\overline{s}$ state. The second resonance has a mass of (1378 ± 10) MeV/c^2 and a width of (361 ± 25) MeV/c^2. Its coupling to $K\overline{K}$ relative to $\pi\pi$ is small and consistent with a mainly $(u\overline{u} + d\overline{d})$ state. These results are relevant to the glueball interpretation of $f_0(1500)$ and the spectrum of scalar $q\overline{q}$ mesons.

From the $f_2'(1525)$ signal, observed for the first time in $\overline{p}p$ annihilation, the mixing angle in the 2^{++} $q\overline{q}$-nonet is determined to be $\theta_{2^{++}} = (26.2 \pm 1.1)^\circ$.

Zusammenfassung

Das Ziel dieser Arbeit war, den Zerfall der Mesonen $f_0(1370)$ und $f_0(1500)$ in $K\overline{K}$ mit hoher Statistik nachzuweisen. Die beiden Zustände wurden kürzlich von der Crystal Barrel Kollaboration in den Reaktionen $\overline{p}p \to \pi^0\pi^0\pi^0$, $\pi^0\eta\eta$, und $\pi^0\eta\eta'$ entdeckt. Der Zustand $f_0(1500)$ wird heute im Allgemeinen als der Grundzustand des skalaren 'Glue'-Balles angesehen, welcher mit naheliegenden $q\overline{q}$ Mesonen mischt.

Der Endzustand $\pi^0 K_L K_L$ aus der $\overline{p}p$ Annihilation in Ruhe in flüssigem Wasserstoff wurde rekonstruiert und analysiert. Die Datenselektion verlangte ein rekonstruiertes $\pi^0 \to \gamma\gamma$, ein nicht-detektiertes K_L sowie ein wechselwirkendes K_L, dessen Impulsrichtung mit dem CsJ Kalorimeter gemessen wurde. Diese Information war ausreichend, um die vollständige Kinematik des Ereignisses zu rekonstruieren. Etwa 37'000 $\pi^0 K_L K_L$ Ereignisse wurden selektiert. Dies entspricht etwa der 100-fachen Statistik der früheren Blasenkammer-Experimente. Eine Partialwellen-Analyse wurde durchgeführt unter der Annahme, dass ausschliesslich der Anfangszustand $^1S_0$ des Protoniums zur Annihilation in den untersuchten Endzustand beiträgt. Die Partialwellen wurden über den K-Matrix Formalismus parametrisiert, um die Unitarität bei überlappenden Resonanzen gleicher Quantenzahlen zu gewährleisten. Der Helizitätsformalismus diente zur Berechnung von Zerfallswinkelverteilungen.

Das Ergebnis dieser Analyse ist die Beobachtung zweier skalarer Resonanzen in ihrem Zerfall nach $K\overline{K}$. Die eine Resonanz besitzt eine Masse von (1515 ± 12) MeV/c^2 und eine Breite von (104 ± 12) MeV/c^2. Diese Werte stimmen gut mit denjenigen des $f_0(1500)$ überein. Das Verzweigungsverhältnis wurde zu

$$B(\overline{p}p \to \pi^0 f_0(1500) \to \pi^0 K\overline{K}) \quad = \quad (4.0 \pm 0.5) \times 10^{-4}$$

bestimmt, woraus die relative Kopplung

$$\frac{\gamma^2(f_0(1500) \to K\overline{K})}{\gamma^2(f_0(1500) \to \pi\pi)} \quad = \quad 0.24 \pm 0.09$$

abgeleitet werden kann. Folglich ist das $f_0(1500)$ nicht der skalare $s\overline{s}$ Zustand. Die zweite Resonanz hat eine Masse von (1378 ± 10) MeV/c^2 und eine Breite von (361 ± 25) MeV/c^2. Die entsprechende Kopplung an $K\overline{K}$ ist klein und konsistent mit der Erwartung eines hauptsächlich aus $(u\overline{u} + d\overline{d})$ bestehenden Mesons. Diese Ergebnisse sind bedeutend für die 'Glue'-Ball Interpretation des $f_0(1500)$ und das Spektrum der skalaren $q\overline{q}$ Mesonen.

Aus der erstmaligen Beobachtung des $f_2'(1525)$ in der $\overline{p}p$ Annihlation konnte der Mischungswinkel des 2^{++} $q\overline{q}$ Nonetts zu $\theta_{2^{++}} = (26.2 \pm 1.1)^\circ$ bestimmt werden.

Contents

1 Quarks, Gluons and QCD

'Gluons shine in their own light', F.E. Close

In the mid-sixties studies on the classification of hadrons and hadron mass spectra suggested that strong interacting particles were made up of more fundamental units, the quarks [1][2][3]. Hadrons could then be understood as compounds of three quarks (qqq) with half-integer spin (baryons such as protons and neutrons) and as quark-antiquark systems ($q\overline{q}$) with integer spin (mesons). Quarks had to have spin-1/2 in order to form baryons and fractional electric charge. Today six types (flavours) of quarks are known: up u, down d, charm c, strange s , top t and bottom b.

According to this scheme it was for example possible to identify the Δ^{++} with (uuu). The three quarks are in a symmetric state since all spins are aligned and relative angular momenta are $l = 0$. This contradicts the Pauli exclusion principle for fermions which could be saved by the introduction of a new degree of freedom, color. This was done by Han and Nambu [4] in 1965. Quarks carry any of three colors (red, blue and green) such that the three quarks in (uuu) are distinct and hence the problem to form an antisymmetric state vanishes. They formulated the origin of strong interactions by introducing a new symmetry $\mathrm{SU}(3)_c$ with eight gauge vector fields, the gluons. Although the interactions forming baryons and mesons act as an octet in $\mathrm{SU}(3)_c$, hadrons will be color-neutral.

The underlying group $\mathrm{SU}(3)_c$, its associated eight gauge vector fields, color-neutral hadrons and color-neutral electromagnetism are the basic ingredients of the quantum field theory of strong interactions, quantum chromodynamics (QCD).

In 1969, deep inelastic *ep* scattering revealed the first experimental evidence of quarks and gluons inside the proton. With increasing energy the electron seemed to scatter off free pointlike particles, the so-called partons. It became clear that partons can be identified with quarks but which carry only about 50% of the mass of the proton. Gluons which do not interact with electrons are responsible for the rest of the mass.

The fact that quarks move freely in the proton, known as asymptotic freedom, could be explained by the non-Abelian structure of $SU(3)_c$ [5][6][7]. Unlike photons, gluons carry the charge of strong interactions (color) and hence couple to each other; gluons emitted by quarks can fragment not only into pairs of $q\overline{q}$ but also into gluons. The first process leads to a shielding of the color-charge of the quark as vacuum polarisation does in QED. In the second process the color charge is spread out and yields an antishielding effect which overcompensates the shielding. The net result is that the coupling α_s of strong interactions decreases with decreasing r and quarks seem to move freely at short distances (< 0.1 fm).

On the other hand α_s increases with larger distances. The attractive potential between quarks grows with r and quarks (and gluons) cannot separate, they are confined. Single (colored) quarks and gluons cannot be observed.

Asymptotic freedom and confinement are intimately related to the self-interaction of gluons. Thus, if QCD is right then two or more gluons should be able to cluster together to form color-neutral and hence observable glueballs.

2 Search for Glueballs

Gluons, the gauge bosons of QCD, have spin 1. So glueballs will have integer spin like $q\overline{q}$ mesons. Since gluons do not carry electric charge, glueballs are isosinglets. For the groundstate of a two-gluon glueball, the two gluons are in a relative S-wave ($l = 0$) and the two spins couple to total spin $s = 0$ or $s = 2$. Thus the quantum numbers are $J^{PC} = 0^{++}$ or 2^{++} and $I = 0$.

Recent computer calculations of QCD (lattice QCD) in the quenched approximation, i.e. without $q\overline{q}$ loops, predict the scalar to be the lowest glueball state at a mass of 1.74 ± 0.07 GeV/c^2 [8]. A slightly lower value of 1.57 ± 0.09 GeV/c^2 is suggested by ref. [9]. These new values agree with previous calculations [10] which gave a mass of 1.55 ± 0.05 GeV/c^2.

Glueballs are expected to be produced in gluon-rich environments such as in radiative J/Ψ decay, in central production of pp and $\pi^- p$ scattering at low momentum transfer and in $\overline{p}p$ annihilations.

The Crystal Barrel Experiment at LEAR/CERN which investigates $\overline{p}p$ an-

nihilation up to a center of mass energy of $\sqrt{s} = 2.4$ GeV has reported the observation of a new scalar resonance, the $f_0(1500)$, decaying into $\pi\pi$ [11] [12] , $\eta\eta$ [13] and $\eta\eta'$ [14]. The masses and widths are consistent, giving the average of

$$\begin{aligned} m &= 1509 \pm 10 \text{ MeV}/c^2 \quad \text{and} \\ \Gamma &= 116 \pm 17 \text{ MeV}/c^2. \end{aligned} \tag{1}$$

The decay into $4\pi^0$ has also been reported [15]. A coupled channel analysis [16] of the final states $3\pi^0$, $\pi^0\eta\eta$ and $\pi^0\pi^0\eta$ gives a mass and a width of 1500 ± 10 MeV/c^2 and 154 ± 30 MeV/c^2, respectivley.

The experiment E760 at Fermilab, investigating $\overline{p}p$ annihilation at higher energies, also found a resonance decaying into $\pi^0\pi^0$ and $\eta\eta$ with masses and widths $(m, \Gamma) = (1508, 103)$ MeV/c^2 [17] and (1488,148) MeV/c^2 [18], respectively. A spin-parity analysis is in progress [20].

In central production, the GAMS collaboration observed a 180 MeV/c broad resonance at 1590 MeV/c^2, called $f_0(1590)$, in the decay modes $\eta\eta$, $\eta\eta'$ and 4π [19]. The WA91 collaboration finds in pp central production an $I = 0$ scalar resonance at 1446 MeV/c^2 with a narrow width of 56 MeV/c^2 decaying into 4π [21]. The mass and width depend on the detailed prescriptions used in the partial wave analysis and therefore the 1590 and 1446 MeV/c^2 states are probably identical to the Crystal Barrel $f_0(1500)$.

A re-analysis of MARKIII data on radiative J/Ψ decay [22] revealed as well a scalar resonance at 1505 MeV/c^2 decaying into 4π. The same state has also been seen in $J/\Psi \to \gamma(\pi\pi)$[23].

All these new $I = 0$, $J^{PC} = 0^{++}$ states were observed in reactions where glueballs are expected, with masses around 1500 MeV/c^2 and comparable widths. They might be the same resonance as the $f_0(1500)$ eventhough quantitative examination still needs to be done. This is in particular important for the relative branching ratios since they play an essential role in identifying the $f_0(1500)$ as the groundstate glueball.

The branching ratios of $f_0(1500)$ production and decay in $\overline{p}p$ annihilation at rest in liquid hydrogen measured by the Crystal Barrel Experiment are ([24]

based on [12],[14] and [16]):

$$\begin{aligned} B(\overline{p}p \to f_0\pi^0, f_0 \to \pi^0\pi^0) &= (8.1 \pm 2.8) \times 10^{-4} \\ B(\overline{p}p \to f_0\pi^0, f_0 \to \eta\eta) &= (5.5 \pm 1.3) \times 10^{-4} \\ B(\overline{p}p \to f_0\pi^0, f_0 \to \eta\eta') &= (1.6 \pm 0.4) \times 10^{-4} \end{aligned} \quad (2)$$

where the errors reflect the uncertainties in the various assumptions made in the fitting procedures. Amsler and Close [24][25] deduced the relative couplings corrected for phase space times a model dependent form factor and find

$$\pi\pi \ : \ K\overline{K} \ : \ \eta\eta \ : \ \eta\eta' = 1 \ : < 0.16 \ : \ 0.27 \pm 0.11 \ : \ 0.19 \pm 0.08 \quad (3)$$

which is in contradiction to what is expected from naive, flavour blind glueball decays assuming equal coupling of u, d and s quarks to gluons [26]:

$$\pi\pi \ : \ K\overline{K} \ : \ \eta\eta \ : \ \eta\eta' = 1 \ : \ 4/3 \ : \ 1/3 \ : \ 0. \quad (4)$$

The most striking difference is the coupling to $K\overline{K}$ for which only an upper limit exists from a bubble chamber experiment [27].

The $s\overline{s}$ member of the $J^{PC} = 0^{++}$ nonet has not yet been identified although two candidates exist, the $f_0'(1525)$ [28] and $f_J(1720)$ [29] with a still controversial spin assignment of 0 or 2. The dominant decay mode for an $s\overline{s}$ state would be $K\overline{K}$ which is not the case for the $f_0(1500)$. Hence, $f_0(1500)$ is not dominantly $s\overline{s}$.

The measured relative couplings of $f_0(1500)$ (eqn. 3) are incompatible with the expectations of an $n\overline{n} \equiv 1/\sqrt{2}(u\overline{u} + d\overline{d})$ state unless a strong violation of flavour symmetry in $SU(3)_f$ is allowed. This is illustrated in figure 1 where the $s\overline{s}/(u\overline{u} + d\overline{d})$ production ratio ρ in meson decay is plotted versus the scalar nonet mixing angle α (defined such that ideal mixing occurs at $\alpha = 0°(90°)$). Exact flavour symmetry means $\rho = 1$. The full and the dashed curves show the couplings relative to $\pi\pi$ for $\eta\eta$ and $\eta\eta'$ at 5 and 10% C.L. upper and lower limit. The dotted curves give various relative couplings to $K\overline{K}$. The black region is the allowed range for α and ρ using the experimental upper limit of [27]. Clearly, a larger branching ratio for $K\overline{K}$ would change this conclusion eventhough the

Figure 1: *ρ as a function of α. The black region shows the range allowed by the experimental data on $f_0(1500)$ decay into $\pi\pi$, $\eta\eta$, $\eta\eta'$ and the upper limit for $K\overline{K}$ (from [25]).*

narrow width of $f_0(1500)$ and the existence of the broad $f_0(1370)$, believed to be the $n\overline{n}$ member of the 0^{++} nonet, still isolates this resonance from a $n\overline{n}$ state that belongs to the scalar $q\overline{q}$ meson nonet.

The fact that the scalar glueball is predicted at a mass close to the several hundred MeV/c^2 broad $f_0(1370)$ suggests that mixing of a glueball G with quarkonium $q\overline{q}$ might play an important role in the decay dynamics. Amsler and Close [24][25] show that $G - q\overline{q}$ mixing can indeed suppress the $K\overline{K}$ while $\eta\eta'$ is enhanced if the glueball lies between the non-strange and strange member of the 0^{++} $q\overline{q}$ nonet. Since the mass of the $s\overline{s}$ state is not known it is not possible to make predictions for the relative couplings.

The quantification of the branching ratio of $f_0(1500)$ decaying into $K\overline{K}$ would not only affect the interpretation but would also allow to predict the mass of the scalar $s\overline{s}$ state. If an $s\overline{s}$ candidate is found at the predicted mass then this would give a self-consistent picture of a scalar $q\overline{q}$ nonet mixed with the groundstate glueball.

3 Previous Measurements of $\overline{p}p \to \pi K\overline{K}$

Armenteros et al. [30] collected first data on $\overline{p}p \to \pi K\overline{K}$ using stopping antiprotons from the CERN PS annihilating in a hydrogen bubble-chamber. They obtained 1,145 events for the reaction $\overline{p}p \to \pi^{\pm}K^{\mp}K^0_S$ and 199 events of the type $\overline{p}p \to \pi^0 K^0_S K^0_S$. The main result was the determination of the branching ratios of these two final states:

$$B(\overline{p}p \to \pi^{\pm}K^{\mp}K^0_S) = (28.2 \pm 1.1) \times 10^{-4}, \quad (5)$$

$$B(\overline{p}p \to \pi^0 K^0_S K^0_S) = (7.8 \pm 0.6) \times 10^{-4}. \quad (6)$$

Based on the same experiment but with increased statistics, Conforto et al. [31] analyzed 2,000 events $\overline{p}p \to \pi^{\pm}K^{\mp}K^0_S$ and 364 events $\overline{p}p \to \pi^0 K^0_S K^0_S$. A partial wave analysis was performed on the first channel. Apart from the dominant K^*K production they needed $a_0(980)$ and $a_2(1320)$ decaying into $K\overline{K}$ in order to describe the data. These results were used to check for consistency in the $\pi^0 K^0_S K^0_S$ data which could not be fitted independently due to the low statistics. A good agreement was found except for the $a_0(980)$. The absence of a threshold enhancement in $K_S K_S$ was interpreted by possible interference effects between the $I = 1$ and $I = 0$ $K\overline{K}$ channels ($a_0(980)$, $f_0(980)$).

Barash et al. collected data on the same final states with a hydrogen bubble-chamber at BNL [32]: 182 events for $\overline{p}p \to \pi^0 K^0_S K^0_S$ and 851 events for $\overline{p}p \to \pi^{\pm}K^{\mp}K^0_S$ were reconstructed and analysed. They found branching ratios of

$$B(\overline{p}p \to \pi^{\pm}K^{\mp}K^0) = (4.25 \pm 0.55) \times 10^{-3}, \quad (7)$$

$$B(\overline{p}p \to \pi^0 K^0_S K^0_S) = (7.3 \pm 1.0) \times 10^{-4}. \quad (8)$$

The branching ratio for the latter reaction is consistent with ref. [30] (eqn. 6). The analysis concentrated only on the $K^*K = K^*\overline{K} + \overline{K^*}K$ production. Possible structures in the $K\overline{K}$ system were not investigated.

Motivated by the observation of an isoscalar resonance at 1525 MeV/c^2 decaying into $\pi\pi$ in the reaction $\overline{p}N \to 3\pi$, for which $J^{PC} = 0^{++}$ was suggested, Gray et al. [27] were looking for the same resonance decaying into $K\overline{K}$. The

analysis was based on their own data on antiproton annihilation in deuterium into $\pi^- K_S K_S$ and $\pi^- K^+ K^-$ as well as on the old data of $\overline{p}p \to \pi^0 K_S K_S$ from Armenteros et al. [30]. No signal around 1525 MeV/c^2 in $K_S K_S$ was found. An upper limit for the f' production was deduced by counting the number of events in the $K_S K_S$ mass projection of the $\pi^0 K_S K_S$ Dalitz plot from ref. [30] (199 events) in the range from 2.2 to 2.4 GeV$^2/c^4$:

$$B(\overline{p}p \to \pi^0 f_0(1500), f_0(1500) \to K\overline{K}) \;<\; 3.4 \times 10^{-4} \quad (95\%\ \text{C.L.}) \qquad (9)$$

No partial wave analysis has been performed, however.

It is interesting to note that all data on $\overline{p}p$ annihilation at rest into $\pi^0 K^0 \overline{K}^0$ with positive C parity of $K^0\overline{K}^0$ to which literature refers were taken about 30 years ago. Clearly, new high statistics data on $\pi K\overline{K}$ have to be collected and analysed such that detailed information about the $K\overline{K}$ system can be obtained from a partial wave analysis. This is the goal of this work.

4 The Crystal Barrel Experiment at LEAR

The Crystal Barrel Experiment at LEAR/CERN was designed to study antiproton annihilations in liquid and gaseous hydrogen and in liquid deuterium, to search for new resonances and to obtain high precision data on known mesons.

The aim was to detect charged and neutral particles with high momentum resolution such that rare annihilation channels could be reconstructed with low background.

The possibility of an online event selection on the basis of charged and neutral multiplicities of the final state particles was required to enhance the statistics of annihilation channels with a low branching ratio and to reduce dead-time of the read-out. In particular, about 18×10^6 events with exclusively neutral final state particles (γ's from π^0, η, η' and ω decays) have been recorded to tape since the beginning of data taking in December 1989, which corresponds to about 450×10^6 antiproton annihilations at rest in liquid hydrogen.

The following description of the detector concentrates on the experimental setup with which the data presented in this thesis were taken.

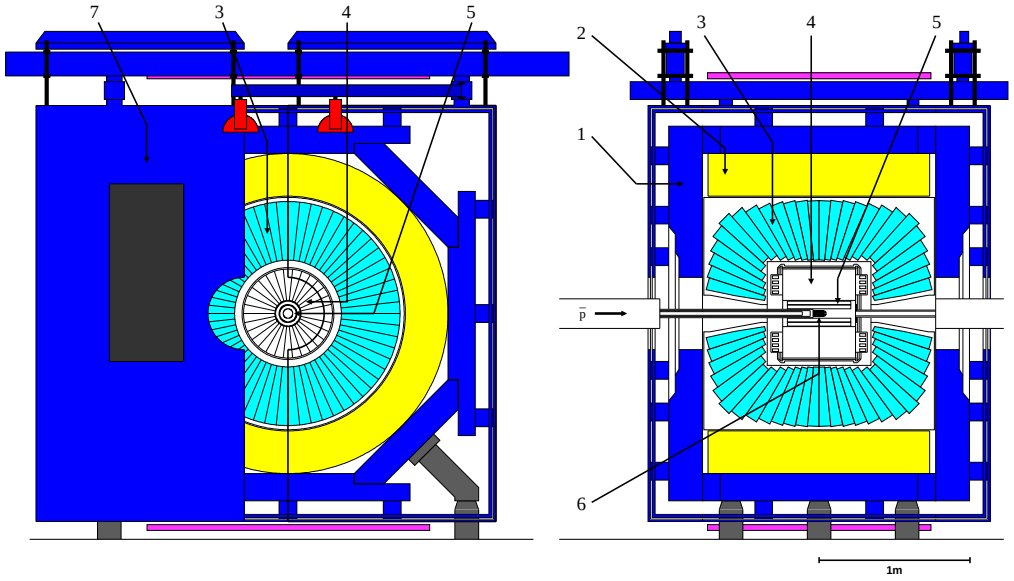

Figure 2: *Overall layout of the Crystal Barrel detector showing (1) magnet yoke, (2) magnet coils, (3) CsI barrel (4) jet drift chamber, (5) proportional chambers, (6) liquid hydrogen target, (7) one half of the endplate.*

4.1 Overall Description of the Detector

The Crystal Barrel Detector [33] consists of a liquid hydrogen target surrounded by two cylindrical multi-wire proportional chambers and a jet drift chamber for the tracking of charged particles. An electromagnetic calorimeter, the crystal barrel, surrounds the inner parts of the detector and covers a solid angle of 97% of 4π. The crystals are read out by photodiodes since the whole detector is located in a solenoid magnet which produces a magnetic field of 1.5 T in the center of the inner volume. The apparatus is shown in figure 2.

4.2 Antiproton Beam

Antiprotons are produced by the bombardment of a tungsten target with 26 GeV/c protons from the proton synchrotron (PS). The momentum distribution peaks at 3.5 GeV/c. Antiprotons around this momentum are selected and sent to

the Antiproton Accumulator (AA). About 10^{12} $\overline{p}$/day are produced and stored. Batches of 2-3$\times 10^9$ antiprotons are returned to the PS where they are decelerated to 600 MeV/c before they enter the Low Energy Antiproton Ring (LEAR). Antiprotons can either be further slowed down to 100 MeV/c or re-accelerated to about 2 GeV/c. A relative momentum spread of $\Delta p/p \approx 10^{-4}$ can be reached by stochastic and electron cooling of the antiproton beam.

Antiprotons at 200 MeV/c are extracted from LEAR for annihilations in liquid hydrogen at rest. Spills can last up to 3 h, after which refilling from the Antiproton Accumulator is necessary. Typical beam intensities are in the range of 10^4 to 10^6 $\overline{p}/s$ depending on whether measurements for stopping antiprotons or interactions in flight are being made. The antiproton flux at the target of the Crystal Barrel experiment does not exceed a few 10^4 $\overline{p}/s$ when the beam is shared with other experiments.

4.3 Entrance Counters and Liquid Hydrogen Target

A segmented silicon diode just before the liquid hydrogen target operates as $\overline{p}$ transmission counter which gives the start signal for the data acquisition. The Si counter consists of four 3×3 mm^2 PIN diodes located 28 mm in front of the target. An additional Si counter with the same dimensions is placed 5 mm before the group of four counters to restrict the beam impinging on the target.

The liquid hydrogen target is 17 mm in diameter and 44 mm long. At a momentum of 200 MeV/c, the incident antiprotons stop in the center of the target with a longitudinal spread of about 0.6 cm.

4.4 The Proportional Wire Chambers (PWC)

Two cylindrical proportional wire chambers surround the target and are used to trigger on the final-state charged multiplicity. Both chambers have a wire length of 35 cm. The anode wires of the inner chamber are at radius 25.5 mm from the magnetic field axis while those of the outer chamber are at radius 43 mm. They cover 99 % and 97 %, respectively, of the full solid angle. The efficiency reaches more than 99%.

Parameter	CsI(Tl)
Density [g/cm^2]	4.53
Radiation length [cm]	1.86
Molière radius [cm]	3.8
Light output	0.85 relative to Na(Tl)
Maximum emission	at 550 nm
Decay times [μs]	0.9 and 7
Photon yield/MeV	4.5×10^4

Table 1: *Properties of the CsI(Tl) scintillator.*

4.5 Jet Drift Chamber (JDC)

Tracking of charged particles is done by a cylindrical jet drift chamber which is divided into 30 azimuthal sectors and 23 radial layers. The inner (outer) sense wires are at a radius of 63 mm (239 mm). With a sensitive length of 399 mm, 95% of 4π solid angle is covered by the inner layers of the JDC.

4.6 The Electromagnetic Calorimeter

A high-efficiency photon detection with a good energy and spatial resolution is needed to enable the reconstruction of neutral decays of π^0, η and η' produced in $\overline{p}p$ annihilations.

The electromagnetic calorimeter consists of 1380 individual CsI(Tl) crystals arranged in a vertex pointing geometry. It covers polar angles from 12° to 168°. The crystals have a length of 300 mm (16.1 radiation lengths) and cover 6° in both polar and azimuthal angles. For crystals at small and large polar angles ($\theta < 30°$ and $\theta > 150°$) the angular range is increased to 12°. The whole calorimeter covers a solid angle of 97% of 4π. The distance from the annihilation vertex to the crystals varies from about 270 mm to 380 mm due to the barrel configuration of the calorimeter. A compilation of the CsI(Tl) properties is given in table 1.

Since the calorimeter is operating in a 1.5 T magnetic field the scintillation light of the crystals is read out by photodiodes. The spectral emission of CsI(Tl) peaks around 550 nm which is already reasonably matched to the sensitivity of the photodiodes, but there is an order of magnitude mismatch between the light

General layout	Barrel configuration
Polar angle range [deg]	12-168
Solid angle	97% of 4π
Cavity length [mm]	540
Cavity radius [mm]	270
Number of elements	1380
Scintillator	CsI(Tl)
Active length [mm]	300(16.1 L_R)
Readout	WLS and photodiode
Total mass [kg]	3,800

Table 2: *Specifications of the Crystal Barrel calorimeter.*

emitting area of a crystal and the sensitive area of a photodiode. Therefore a wavelength shifter consisting of a 3 mm thick Plexiglas tile doped with an optical active pigment is used to collect the light from the surface of the crystal. This tile absorbs light at 520 nm and re-emits it at a longer wavelength. The photodiode is glued onto one lateral face of the tile while the other faces are painted with a white diffuser to increase the light collection efficiency. The photodiodes are read out by a charge integrating amplifier with integration time of order 1 μs. The shaping amplifier then generates an approximately gaussian pulse with a width of ≈ 4 μs.

After shaping, the analog signals are digitized by two ADC systems operating in parallel. The LeCroy 2282 system with 4096 channels covers the low energy range from 0 to 400 MeV/c^2 with a high sensitivity of 0.1 MeV/channel. The LeCroy 4300-B FERA system with 2048 channels covers the full energy range from 0 to 2000 MeV (1 MeV/channel).

An offline calibration is required to calculate the deposited energy from the ADC's of each crystal. Using $\pi^0 \rightarrow \gamma\gamma$ decays, the calibration factors of each crystal are adjusted to match the correct π^0 mass.

Table 2 summarizes the technical specifications of the calorimeter.

4.7 Trigger System

A multi-level trigger system has been designed such that different types of data can be recorded and the effects of dead time are minimized.

The level 0 trigger gives the timing for the electronics and is defined by the incoming antiproton transversing the central Si entrance counters.

The level 1 trigger uses the information from the two subdetectors PWC, JDC in order to accept events with a particular charged multiplicity. The logic to detect the number of charged annihilation products in the PWC is based on the analog sum of the hits in each of the two chambers which is digitized and compared in a PLU[1] with a predefined multiplicity. Only six layers are used to define the multiplicity in the JDC, the inner layers 2,3,4,5 and the outer layers 20 and 21. This configuration enables triggering on long tracks in the drift chamber to improve on the momentum resolution. The determination of the charged multiplicity for the PWC and the JDC is done in parallel. The final decision to accept an event is taken 6 μs after the start signal from the level 0 trigger. The 'all neutral' trigger demands a charged multiplicity of zero in both PWC's and any multiplicity in the JDC. Due to the high efficiencies of the two PWC's, this trigger is very selective. Only about 4% of all annihilations are of this type. Events with no charged particles are recorded on tape at an acquisition speed of about 80 Hz.

The level 2 trigger contains a hardware total energy sum and the Fast Cluster Encoding (FACE) of the CsI calorimeter. The latter is used to determine the cluster multiplicity in the calorimeter which allows, together with the level 1 trigger, to select events with a defined charged and neutral multiplicity. The decision time of the level 2 trigger is 43 μs and thus the level 2 trigger is the slowest part of the complete hardware trigger.

A software trigger has been developed in order to trigger on a specific final state. After an event has been accepted by the hardware trigger, the software trigger uses the information from the crystals of the calorimeter to search for $\gamma\gamma$ combinations which fall in a π^0, η or η' mass window. This trigger was successfully

[1] Programable Logic Unit

used in the analysis of $\overline{p}p \to \pi^+\pi^-\pi^0\pi^0\eta$ [34] for which the decision time was 1-2 ms. With a different event topology it was also possible to take data of $\overline{p}p$ annihilations into $\pi^0\eta\eta$ with high statistics [13].

4.8 Photon Reconstruction

The electromagnetic shower of a photon entering the CsI calorimeter spreads out over several crystals. The size of such a cluster depends on the energy of the incident photon and varies from one up to about 20 crystals. The reconstruction of photons is done by searching for clusters of neighbouring crystals with energy deposits of at least 1 MeV. Then, local maxima within a cluster are searched. In the case of one local maximum, the photon energy is defined as the cluster energy. The same is valid for clusters where none of the crystals has enough energy to be counted as local maximum. The direction is given by the center of gravity of the crystals weighted by their energies. If several local maxima are found inside a cluster, then the cluster is considered to consist of more than one photon. In this case the cluster energy E_C is shared between the photons. Each local maximum crystal and its eight neighbours can be considered as a subcluster. The energy of the ith photon associated to each subcluster is then calculated as

$$E_{\gamma,i} = \frac{E_{9,i}}{\sum_{j=1}^{n} E_{9,j}} E_C \,, \tag{10}$$

where $E_{9,j}$ is the energy of each subcluster j. If more than one local maximum is found then the direction of a photon is defined by the center of the central crystal of a subcluster.

The energy resolution for a photon is

$$\sigma(E)/E = 2.5\% \ (E[GeV])^{-1/4}. \tag{11}$$

The angular resolution is also energy dependent and is typically 25 mrad in θ and ϕ (see eqn. 21 below).

Since apart from photons, also charged particles and interacting K_L deposit energy in the calorimeter, a reconstructed subcluster is referred to as PED (Particle Energy Deposit).

Run Period	Cluster [MeV]	PED [MeV]
July 1990	10	10
November 1990	20	20
May 1991	4	10
June 1991	4	10

Table 3: *Minimum energy for a cluster and a PED.*

The minimum energy required for a cluster and the central crystal of a PED was slightly different for each run period which has been analysed in this work (see table 3). Note that if none of the crystals has an energy above the central crystal energy cut, the whole cluster is considered to be one PED.

5 The Reaction $\overline{p}p \rightarrow \pi K\overline{K}$

A comprehensive study of the $K\overline{K}$ system produced in $\overline{p}p \rightarrow \pi K\overline{K}$ includes all of the following reactions:

1. $\overline{p}p \rightarrow \pi^{\pm}K^{\pm}K^0$ with $I_{K\overline{K}} = 1$ and $K^0 = K_L$ or K_S,
2. $\overline{p}p \rightarrow \pi^0 K^- K^+$ with $I_{K\overline{K}} = 0, 1$ and $C_{K\overline{K}} = \pm 1$,
3. $\overline{p}p \rightarrow \pi^0 K^0 \overline{K}^0$ with $I_{K\overline{K}} = 0, 1$ and $C_{K\overline{K}} = +1$, i.e. $K^0\overline{K}^0 = K_S K_S$ or $K_L K_L$, and
4. $\overline{p}p \rightarrow \pi^0 K_L K_S$ with $I_{K\overline{K}} = 0, 1$ and $C_{K\overline{K}} = -1$.

The search for the $(I^G)J^{PC} = (0^+)0^{++}$ $f_0(1500)$ decaying into $K\overline{K}$ requires positive C-parity and isospin $I = 0$ of the $K\overline{K}$ system. Reactions 2 and 3 fulfill these conditions.

Apart from the additional $C = -1$ configuration of the K^+K^- system, reaction 2 poses serious problems in the data reconstruction. The seperation of charged kaons from pions by the measurement of the energy loss dE/dx in the JDC is possible for momenta up to about 400 MeV/c. Kaons from $\overline{p}p \rightarrow \pi K\overline{K}$ have a maximum momentum of 750 MeV/c and hence $\pi^0 K^+ K^-$ cannot be distinguished from $\pi^0\pi^+\pi^-$ over a large region of phase space. This and the fact

that $\overline{p}p$ initial states with any C-parity can contribute to the final state $\pi^0 K^+ K^-$ lead to the conclusion that reaction 2 is not appropriate to study $\overline{p}p \to \pi K \overline{K}$ [2].

The C-parity of the $K_S K_S$ and $K_L K_L$ system is positive and $J^{PC} = 0^{++}$, 2^{++}, 4^{++} etc.. But both isospin states $I = 0$ and $I = 1$ are possible. In order to separate the two isospin contributions in reaction 3, independent information on the $I = 1$ $K\overline{K}$ system from reaction 1 might be helpful.

Reaction 3 with $K_S K_S$ can be reconstructed using different decay modes of the K_S. With both K_S decaying into $\pi^0\pi^0$ it would be neccessary to select data with 10 PEDs from all-neutral triggered events from $\overline{p}p$ annihilations at rest. There are 945 (!) $\gamma\gamma$ combinations that may form $5\pi^0$ and another 15 combinations to form $\pi^0 K_S K_S$. The combinatorics makes it difficult to select $\pi^0 K_S K_S$ events with low background. In addition, the two secondary vertices for $K_S \to \pi^0\pi^0$ (and hence the γ directions) cannot be measured precisely.

In order to reduce the combinatorics, one or even both K_S could be selected via their charged decay into $\pi^+\pi^-$. The channel $\pi^0 K_S K_S$ has then to be reconstructed from $\pi^+\pi^-\pi^0\pi^0\pi^0$ or $\pi^+\pi^-\pi^+\pi^-\pi^0$ events. Using the branching ratio $B(\pi^+\pi^-3\pi^0) = (97 \pm 6) \times 10^{-3}$ of the $\pi^+\pi^-3\pi^0$ final state [35], the branching ratio $B(\pi^0 K_S K_S) = (7.3 \pm 1.0) \times 10^{-4}$ of $\overline{p}p \to \pi^0 K_S K_S$ from [32] and the $\pi^+\pi^-$ and $\pi^0\pi^0$ decay ratios of K_S, the relative contribution of $\pi^0 K_S K_S$ is

$$\frac{B(\pi^0 K_S K_S)}{B(\pi^+\pi^-3\pi^0)} = 3.2 \times 10^{-3}. \qquad (12)$$

It is therefore impossible to isolate $\pi^0 K_S K_S$ events without large background contamination from other channels that contribute to 5π.

However, the decay length of K_S is typically a few centimeters ($\sim$2 cm at 400 MeV/c) and hence long enough that high energy K_S decaying into $\pi^+\pi^-$ can be tagged by the change of the charged multiplicity from the inner PWC to the JDC.

The Crystal Barrel collaboration has taken such data by asking for no hits in the inner PWC but two tracks in the JDC. About 12,000 $\pi^0 K_S K_S$ events could be

[2] Recent improvements on the tracking of charged particles in the JDC made the separation of $\pi^0 K^+ K^-$ from $\pi^0\pi^+\pi^-$ possible on the basis of energy and momentum conservation.

0 PEDs	1 PED	2 PEDs	$\geq$3 PEDs
43%	28%	16%	13%

Table 4: *K_L interaction probabilities for producing n PEDs (from [36]).*

reconstructed and the analysis is in progress. Since the sense wires of the PWC are at 2.5 cm radial distance from the beam axis the trigger acceptance depends strongly on the momentum and direction of the K_S. In order to reduce this bias, the two PWC's were replaced by a silicon vertex detector. The minimum radial distance from the primary vertex could be reduced to 1.2 cm. Data using the vertex detector have also been taken and are currently analyzed.

The final state $\pi^0 K_L K_L$ is an alternative $\pi^0 K_S K_S$ with no bias on slow K^0's. The reconstruction and analysis of this final state are subject of this thesis.

6 The Channel $\pi^0 K_L K_L$ in the 3-PED Final State

In contrast to most of the hadrons observed with the Crystal Barrel Experiment K_L have a relatively long lifetime of $\tau = (5.17 \pm 0.04) \times 10^{-8}$ s. The survival probability for a particle of mass m after a travel distance d depends on its momentum p and lifetime:

$$P(d) \quad = \quad e^{-\frac{md}{\tau p}} \tag{13}$$

For a typical momentum of 400 MeV/c and a distance of 0.4 m, about 96% of all K_L reach the calorimeter where they either decay or interact hadronically. The interaction probability was measured in the analysis of $\overline{p}p \rightarrow K_S K_L$ [36] and a value of $(57.2 \pm 2.7\%)$ for a K_L of 795 MeV/c was found. The K_L-interaction can be seen as an energy deposit in the crystals giving one or more PEDs. The probabilities for finding $n = 0, 1, 2, \geq 3$ PEDs are given in table 4. PEDs or clusters from interacting K_L and photons are hardly distinguishable eventhough a K_L produces in general larger clusters [36]. In the case of a K_L producing

one PED the opening angle between the K_L and its PED is close to zero. This correlation can be used in $\pi^0 K_L K_L$ to identify the direction of the interacting K_L with the one of the PED.

There are several ways to analyze $\pi^0 K_L K_L$. The simplest one is to select 2-PED events where only one π^0 is found. The missing mass spectrum contains information about the $K_L K_L$ system. But this spectrum is only a projection of the two-dimensional Dalitz plot and therefore the spin of a resonance decaying into $K_L K_L$ cannot be determined.

Another possibility to study $\overline{p}p \to \pi^0 K_L K_L$ is to select 3-PED events, where two PEDs belong to the π^0 and one PED to an interacting K_L. The second K_L is not interacting and hence missing. The opening angle between the π^0 and the PED can be used to reconstruct the full event, i.e. the energies of both K_L and the direction of the missing K_L. Contrary to the 2-PED case it is now possible to analyze the full Dalitz plot and hence to study the $K\overline{K}$ system in detail.

A third possibility is to look at 4-PED events. Assuming two PEDs coming from two interacting K_L's it would be possible to use this additional constraint in the analysis.

The 3-PED and the 4-PED final states can be used to determine the spin of resonances in $K\overline{K}$. Using the probabilities for a K_L not being detected ($P_0 = 0.43$) and a K_L producing one PED ($P_1 = 0.28$) [36] one obtains the relative rate of these two final states[3]:

$$R = \frac{\pi^0 K_L K_L \to 3 \text{ PED}}{\pi^0 K_L K_L \to 4 \text{ PED}} = \frac{2 P_0 P_1}{P_1^2} \simeq 3. \tag{14}$$

This clearly favours the 3-PED final state when high statistics data is required. In addition, background from channels with a large branching ratio compared to $\pi^0 K_L K_L$, like 5-PED events from $\overline{p}p$ annihilation into $\omega\pi^0$ and $\omega\eta$ where $\omega \to \pi^0\gamma$ and $\pi^0, \eta \to \gamma\gamma$, and 6-PED events from annihilations into $3\pi^0$, $\pi^0\pi^0\eta$ and $\pi^0\eta\eta$ is expected to be small, since two or three photons have to escape detection.

[3]Here, it is assumed that the probabilities P_0 and P_1 are momentum independent.

6.1 Selection of π^0+1 PED Events

The present analysis is based on 13.2 million events which have been taken with the all-neutral trigger (see section 4.7) during the run periods of July 1990, November 1990, May 1991 and June 1991. Using the ratio $R(\text{0-prong}) = (3.9 \pm 0.3)\%$ of all-neutral (0-prong) events to the number $N_{\overline{p}p}$ of stopped antiprotons [37] one finds

$$N_{\overline{p}p} = 3.38 \pm 0.26 \times 10^8 \text{ annihilations}. \tag{15}$$

The data sample has been reduced to 158'413 events by requiring 3 PEDs of at least 20 MeV energy (Table 6 on *p.* 29 gives the number of events at each step of the selection).

The photon reconstruction associates with each maximum of energy deposit in a cluster of crystals a PED. This yields in general a good description of the multiplicity in the CsI calorimeter. However, since the development of an electromagnetic shower is a statistical process, about 5% of all photons produce more than one local maximum within a cluster or even several clusters. Such an additional PED is called split-off which has in general much less energy than the parent PED. The opening angle between the two is typically less than $\theta = 26°$, i.e. $\cos\theta = 0.90$. Events with split-offs can be efficiently recognized when a cut on the opening angle and the energy ratio $R < 1$ of two PEDs is applied. The cut has been chosen such that the fastest π^0 occuring from $\overline{p}p$ annihilations at rest which lead to nearby PEDs are not affected [38]. Split-offs are then defined as PED-PED combinations with an opening angle smaller than expected for a π^0 of 1 GeV/c ($\gamma = 7.47$) at a given energy ratio R. A 3-PED event was rejected whenever

$$\cos\theta \;>\; \max\left\{1 - \frac{1}{2R\gamma^2}(1+R)^2, 0.90\right\}. \tag{16}$$

The situation for 3-PED events is shown in figure 4 where $\cos\theta$ is plotted versus the energy ratio R of all PED-PED combinations. Split-offs are observed at small energy ratios and at small opening angles. The split-off cut of eqn. 16 is given by the curve. The curved structures are mainly due to $\pi^0\pi^0$ and $\eta\pi^0$ events

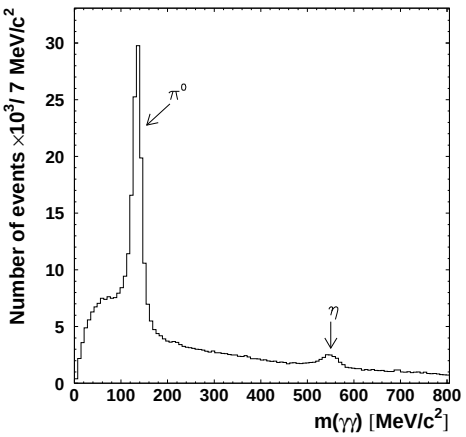

Figure 3: *PED-PED invariant mass of 3 PED events (3 entries per event).*

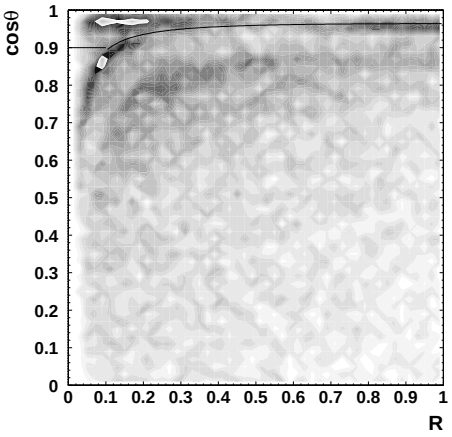

Figure 4: *Opening angle* $\cos\theta$ *versus energy ratio R of all PED-PED combinations. The curve shows the split-off cut. Events in the upper left corner are split-offs.*

where one photon is undetected. Figure 3 shows the PED-PED invariant mass spectrum for 3-PED events before the split-off cut (3 entries per event). Clear signals from $\pi^0 \to \gamma\gamma$ and $\eta \to \gamma\gamma$ can be observed. The π^0 signal was fitted using a Gaussian and a polynomial to describe the background. The fitted π^0 mass was 134.5 ± 0.2 MeV/c^2 but the width depended slightly on the choice of the order of the polynomial and the range in which the spectrum was fitted. Values of σ between 6.5 and 9 MeV/c^2 were found. A value of $\sigma = 7.5$ MeV/c^2 was adopted in order to define a π^0 mass window. Events were selected for which at least one PED-PED invariant mass combination m_{PP} satisfied

$$|m_{PP}[\mathrm{MeV}/c^2] - 135| \;<\; 30 \;\; (4\sigma). \tag{17}$$

From maximal 3 possible combinations that can be assigned to the π^0, the correct one was then assumed to be the one closest to the π^0 mass. 112,684 events were selected and 90,728 π^0+1 PED events survive also the cut on split-offs.

The distribution of these events in the p_{tot} vs. E_{tot} plot is shown in figure 5. Noteworthy regions are labelled with A, B, B1 and B2.

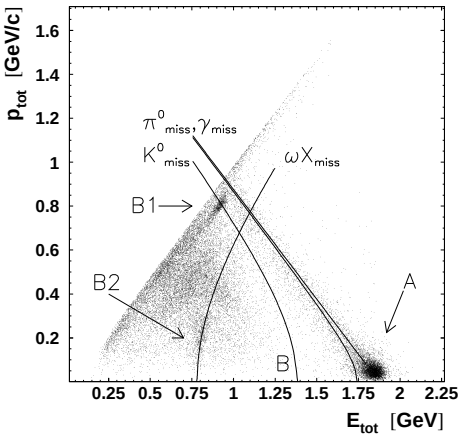

Figure 5: *Total momentum versus total energy for $\pi^0\gamma$ events. The regions A, B, B1 and B2 are explained in the text.*

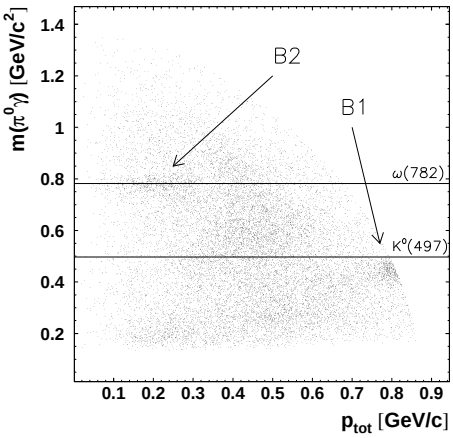

Figure 6: *Invariant $\pi^0\gamma$ mass versus total momentum for $\pi^0\gamma$ events in region B.*

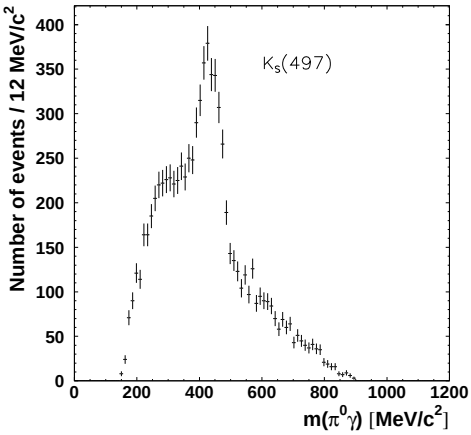

Figure 7: *$\pi^0\gamma$ invariant-mass spectrum for events in region B with $p_{tot} > 600$ MeV/c.*

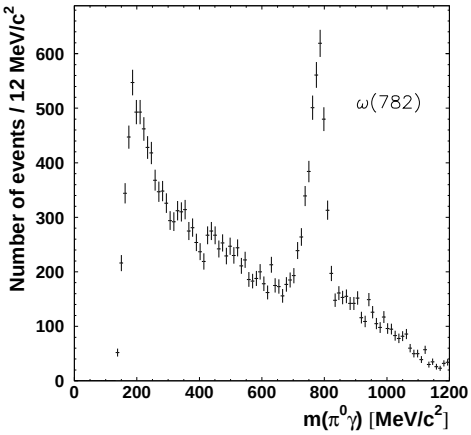

Figure 8: *$\pi^0\gamma$ invariant-mass spectrum for events in region B with $p_{tot} < 350$ MeV/c.*

Events where total energy and momentum are conserved are located in region A. The energy is about twice the proton mass m_p and the total momentum is close to zero. These are $\pi^0\gamma$ events and $\pi^0\pi^0$ events where one of the decay photons of $\pi^0 \to \gamma\gamma$ has an energy below the threshold of 20 MeV and hence is undetected. Photons can also escape detection if they leave the detector through the openings of the calorimeter. Energy and momentum balance is then clearly violated. If one photon is lost, e.g. from $\pi^0\pi^0$ and $\pi^0\eta$ events, then the event is located along the curve labelled γ_{miss}.

If both photons from a π^0 decay are undetected, e.g. one photon is below threshold and one is lost through the openings of the detector, then such events are distributed along the curve labelled π^0_{miss}. This might be the case for $\omega\pi^0$ events where $\omega \to \pi^0\gamma$. In particular, if the π^0 recoiling against the ω is undetected, the measured total energy and momentum are those of the ω. Events where the ω is the only detected particle are distributed along the curve labelled ωX_{miss}. One observes an accumulation of events, due to $\omega\pi^0_{miss}$ events, where ωX_{miss} crosses π^0_{miss}.

Events of the type $\pi^0 K_L K_L$ will be selected with one missing K_L. If the interacting K_L would deposit all its energy, the momentum of the missing K_L would be

$$p_{tot} = \sqrt{(2m_p - E_{tot})^2 - m_K^2)} \tag{18}$$

which is indicated in figure 5 by the curve labelled K^0_{miss}. But the interacting K_L does not deposit all its energy. Hence, these events are found <u>below</u> the curve defined by equation 18. This region is labelled with B. Requiring

$$p_{tot} \leq \sqrt{(2m_p - E_{tot})^2 - m_K^2)} \tag{19}$$

selects 60,983 events. This cut is equivalent to the requirement of a missing mass greater than m_K. In region B, striking structures marked with B1 and B2 are observed. The same accumulation of events can be observed in figure 6 where the $\pi^0\gamma$ invariant mass is plotted versus the total momentum of the event. The mass positions for ω and K_S are indicated.

In figure 5, region B1 is close to the curve for missing K_L; the total momentum is about 800 MeV/c. Kaons from the annihilation $\overline{p}p \rightarrow K_L K_S$ at rest have a momentum of 795 MeV/c. The $\pi^0\gamma$ invariant mass spectrum (fig. 7) for events in the region B with $p_{tot} > 600$ MeV/c shows a K_S signal which is shifted to lower mass since one photon from $K_S \rightarrow \pi^0\pi^0 \rightarrow 4\gamma$ is not detected. Thus, region B1 contains a substantial contribution of $K_S K_L^{miss}$ events.

Events at B2 accumulate on the curve for ωX_{miss}. Figure 6 shows that the ω signal is visible up to a momentum of about 350 MeV/c. The maximum momentum for an ω from the reaction $\overline{p}p \rightarrow \omega K_L K_L$ is 300 MeV/c which suggests that events in region B2 stem partially from $\omega K_L K_L$ events with both K_L missing. Figure 8 shows the ω signal in the $\pi^0\gamma$ invariant mass spectrum for $p_{tot} < 350$ MeV/c.

$K_L K_S$ and $\omega K_L K_L$ events will be discussed in detail in section 7 when dealing with background in $\pi^0 K_L K_L$.

6.2 Reconstruction of $\pi^0 K_L K_L$ Events

6.2.1 Kinematic Fit

So far, potential $\pi^0 K_L K_L$ events were selected by requiring at least one PED-PED combination in a rather large (8σ) window centered at the π^0 mass and a missing mass larger than m_K (region B in figure 5). In order to determine the unknown variables (energy and momentum of both K_L and the direction of the missing K_L), the possibility of a kinematic fit was studied.

There are 12 variables which determine a $\gamma\gamma K_L K_L$ event: 3 variables for each photon (E_γ, θ_γ and ϕ_γ) and 3 variables for each K_L (E_{K_L}, θ_{K_L}, ϕ_{K_L}). Energies and angles of both photons and the direction of one K_L are measured (8 variables). Thus, the 4 equations needed to determine the unknown variables are given by energy and momentum conservation. As two photons form a π^0, there is an additional constraint and hence, a 1C kinemetic fit would be possible.

A fit to the π^0 mass should improve in the measured energies and angles of the two decay photons and therefore in the momentum of the recoiling $K_L K_L$ system.

Generated momentum p_{π^0} [MeV/c]	Before 1C fit: π^0 Mass resolution σ_m [MeV/c^2]	Momentum resolution σ_p [MeV/c]	After 1C fit: π^0 Momentum resolution σ_p [MeV/c]
300	6.5 ± 0.2	9.2 ± 0.4	8.8 ± 0.4
400	6.7 ± 0.3	11.2 ± 0.5	10.8 ± 0.5
500	7.6 ± 0.3	13.7 ± 0.6	12.3 ± 0.5
600	8.7 ± 0.3	15.2 ± 0.7	14.3 ± 0.6

Table 5: *Results from the 1C fit to the π^0 mass.*

It was tested to what extent the momentum resolution of the π^0 can be improved by fitting its mass. Monochromatic $\pi^0 \to \gamma\gamma$ events at momenta 300, 400, 500 and 600 MeV/c were generated. The detector performance was simulated by smearing the energies and angles of the photons according to their experimental resolution (assuming gauss distributions):

$$\frac{\sigma_E}{E} = 2.5\%(E[\mathrm{GeV}])^{-1/4} \tag{20}$$

and

$$\sigma_{\theta,\phi}[\mathrm{mrad}] = \begin{cases} 35 & \text{for } E < 100 \\ 35 - 1.667\ 10^{-2}(E[\mathrm{MeV}] - 100) & \text{for } 100 < E < 1000 \\ 20 & \text{for } E > 1000 \end{cases} \tag{21}$$

The momentum resolution did not improve significantly (table 5). This is due to the parametrization of the constraint for the π^0 mass:

$$m^2_{\pi^0} = 2E^2_{\gamma,1}R(1 - \cos\theta) \tag{22}$$

where $R = E_{\gamma,2}/E_{\gamma,1}$. For a given opening angle θ, R depends on the unknown pion energy $E_{\pi^0} = E_{\gamma,2} + E_{\gamma,1}$. The fit iteration stopped as soon as an appropriate energy ratio R was found for which the constraint could be satisfied. In general, this happened before the generated values of the photon energies were found. The π^0 momentum resolution did not improve because the π^0 momentum is mainly determined by the photon energies and not by the opening angle θ.

6.2.2 Direct Method

Since a kinematic fit does not help significantly to reconstruct $\pi^0 K_L K_L$ events and would prevent the background subtraction under the π^0 peak, the events

were not fitted. The unknown variables had therefore to be deduced directly from the measured variables.

The reconstruction was done such that all $\pi^0 K_L K_L$ events were located within a well defined boundary of the Dalitz plot given by the masses of the final state particles π^0 and K_L. This means that the nominal masses were used for all three particles. The energy of the π^0 was recalculated using the measured momentum and the π^0 nominal mass (instead of summing the two photon energies). The large (8σ) π^0 mass window was divided into three sub-bins:

1. main window : (135 ± 15) MeV/c^2 ($\pm 2\sigma$)
2. lower side-bin (SL) : (112.5 ± 7.5) MeV/c^2 ($\pm 1\sigma$)
3. upper side-bin (SU) : (157.5 ± 7.5) MeV/c^2 ($\pm 1\sigma$).

Events with <u>at least one</u> PED-PED combination in the main window were considered as events with a real π^0 (51,954 events). Events with <u>no</u> entries in the main window but at least one entry in either of the sidebins (9,029 events) were used to describe the background under the π^0 peak. They were reconstructed in the following as $\pi^0 K_L K_L$ events, assuming the correct π^0 mass, to perform a background subtraction in the $\pi^0 K_L K_L$ Dalitz plot.

The systematic error introduced by the recalculation of the π^0 energy is small. It was found that the difference between the calculated and directly measured π^0 energies is typically smaller than 5 MeV, comparable to the intrinsic energy resolution (figure 9).

Figure 10 shows the π^0 momentum spectrum for events in region B of figure 5. The contribution of events from the π^0 side-bins representing the background is superimposed. The distribution for events from the π^0 main window shows prominent structures. The position of known resonances recoiling against a π^0 are indicated by arrows. These structures are missing in the background spectrum. The maximum momentum $p_{\pi^0}^{max}$ for a π^0 from $\overline{p}p \to \pi^0 K_L K_L$ is given by

$$p_{\pi^0}^{max} = \frac{\sqrt{(4m_p^2 - (2m_{K_L} + m_{\pi^0})^2)(4m_p^2 - (2m_{K_L} - m_{\pi^0})^2)}}{4m_p} = 666 \text{ MeV}/c. \quad (23)$$

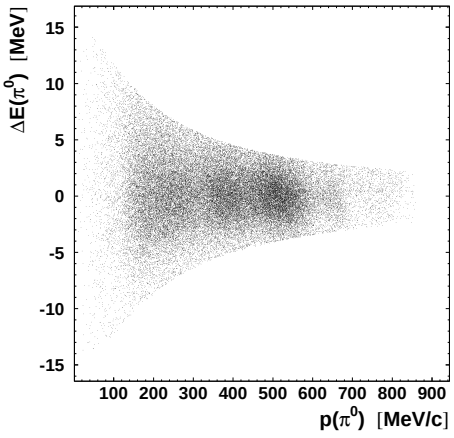

Figure 9: *Difference ΔE_{π^0} of calculated and measured pion energy versus π^0 momentum for events with at least one PED-PED invariant mass combination in the π^0 main window.*

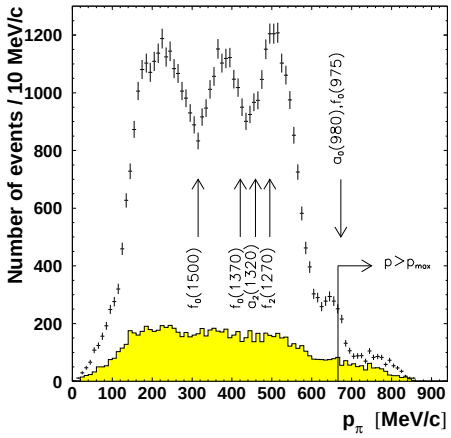

Figure 10: *π^0 momentum distribution for π^0+1 PED events with missing mass greater than m_K. The hatched histogram shows the background. Arrows mark the corresponding positions for known resonances. The maximum momentum of the π^0 from $\overline{p}p \to \pi^0 K_L K_L$ is indicated.*

Due to the finite momentum resolution the π^0 momentum spectrum extends over this kinematic limit. In order to calculate the unmeasured variables of both K_L, a cut on the π^0 momentum had to be applied since the nominal mass of the K_L was used for the reconstruction of the $\pi^0 K_L K_L$ events. As a consequence, part of the $a_0(980)/f_0(980)$ signal above the maximum momentum is lost.

The reconstruction of the unmeasured variables for the two K_L is described in the following. By requiring

$$p_{\pi^0} < p_{\pi^0}^{max}, \tag{24}$$

50,064[8,622] events were selected. The first number is the number of events from the π^0 main window and the number in the brackets the number of events from the side-bins.

The Lorentz transformation of the opening angle $\theta_{\pi^0,PED}$ into the rest frame of the $K_L K_L$ system yields the decay angle of the interacting K_L in the rest frame

of the $K_L K_L$ system:

$$p \sin\theta = p^* \sin\theta^* \qquad \text{and} \tag{25}$$

$$p \cos\theta = \gamma(p^* \cos\theta^* + \beta E^*) \tag{26}$$

where the asterisk denotes the variables in the $K_L K_L$ rest frame and β the velocity of the $K_L K_L$ system. Dividing these two equations leads to

$$\tan\theta = \frac{p^* \sin\theta^*}{\gamma(p^* \cos\theta^* + \beta E^*)} \tag{27}$$

which yields a quadratic equation for $\cos\theta^*$:

$$\cos^2\theta^* \left(1 + \frac{1}{(\gamma \tan\theta)^2}\right) + 2\frac{\beta}{\beta^*}\cos\theta^* + \left(\frac{\beta}{\beta^*}\right)^2 - \frac{1}{(\gamma\tan\theta)^2} = 0. \tag{28}$$

The two solutions can be written as

$$\cos\theta^* = \frac{-\frac{\beta}{\beta^*} \pm \frac{1}{|\gamma\tan\theta|}\sqrt{1 - (\frac{\beta}{\beta^*})^2 + \frac{1}{(\gamma\tan\theta)^2}}}{1 + \frac{1}{(\gamma\tan\theta)^2}}. \tag{29}$$

Figure 11 shows the functional relation between $\cos\theta^*$ and $\cos\theta$ for β and β^* corresponding to $K\overline{K}$ masses of 1400, 1125 and 1100 MeV/c^2. In the case of $\beta/\beta^* \leq 1$, the solution with the positive (negative) sign corresponds to forward (backward) emitted K_L's in the laboratory frame. There is an ambiguity in the case of $\beta/\beta^* > 1$ (hatched region in figure 12) since both K_L are boosted in forward direction ($\theta < \pi/2$) and it is not possible to decide whether the detected K_L goes in forward or backward direction in the $K\overline{K}$ rest frame if its energy is unknown. However, the probability P for finding $\cos\theta^*$ when $\cos\theta$ is measured can be used to attribute one of the two solutions to the measured angle. The probability is related to the Jacobian

$$\frac{d\cos\theta}{d\cos\theta^*} = \frac{1 + \beta/\beta^* \cos\theta^*}{\gamma^2[(\beta/\beta^* + \cos\theta^*)^2 + \sin^2\theta^*/\gamma^2]^{3/2}} \tag{30}$$

and can be defined as

$$P_i \equiv |\frac{d\cos\theta}{d\cos\theta^*}|^{-1}. \tag{31}$$

The probability P_i where $i = 1, 2$ was calculated for each solution of $\cos\theta^*$. A random number R was generated in the range from zero to one and the first

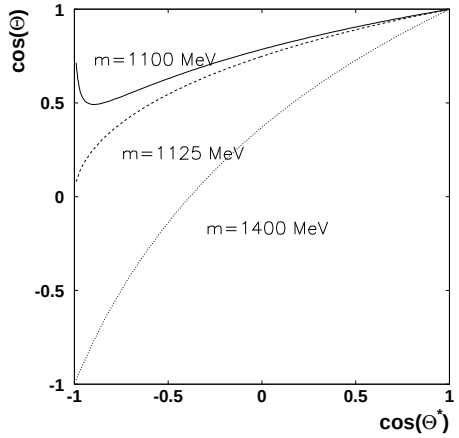

Figure 11: $\cos\theta$ *as a function of the decay angle* $\cos\theta^*$ *in the rest frame of a* $K\overline{K}$ *resonance of mass 1400, 1125 and 1100 MeV/*c^2*, respectively. For* $m < 1125$ *MeV/*c^2 *two solutions of* $\cos\theta^*$ *are possible for a fixed value of* $\cos\theta$*.*

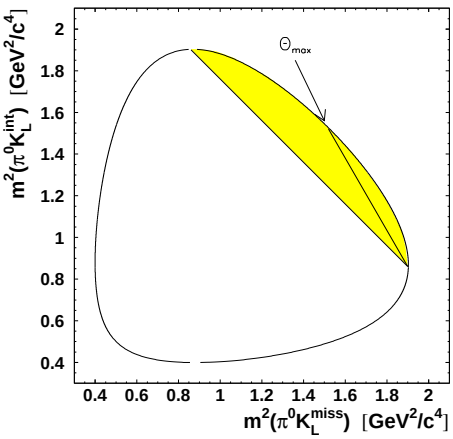

Figure 12: *Dalitz plot* $m^2(\pi^0 K_L^{int})$ *vs* $m^2(\pi^0 K_L^{miss})$*.* $\pi^0 K_L K_L$ *events are located within the curved boundary. The hatched region shows where both* K_L *are emitted in forward direction with respect to the flight direction of the* $K_L K_L$ *system (*$m_{K_L K_L} < 1125$ *MeV/*c^2*). The maximum decay angle for the interacting* K_L *in the laboratory frame is found along the line labelled with* θ_{max}*.*

solution was accepted if

$$R \;<\; \frac{P_1}{P_1 + P_2}. \tag{32}$$

The finite resolution is responsible for difficulties around the maximum decay angle of the interacting K_L in the laboratory frame. This critical region in the Dalitz plot $\pi^0 K_L K_L$ is marked with the curve θ_{max}. The mass of the $K_L K_L$ is given by the momentum of the π^0:

$$m^2_{K_L K_L} \;=\; (2m_p - E_{\pi^0})^2 - p^2_{\pi^0} \tag{33}$$

where $E_{\pi^0} = \sqrt{m^2_{\pi^0} + p^2_{\pi^0}}$. The error of the squared $K_L K_L$ mass is then

$$\sigma_{m^2} \;=\; 2p_{\pi^0}\left(\frac{E_{\pi^0} - 2m_p}{E_{\pi^0}} - 1\right)\sigma_{p_{\pi^0}} \tag{34}$$

from which the mass resolution

$$\sigma_m = \frac{1}{2m}\sigma_{m^2} \tag{35}$$

can be deduced. For a momentum of $p_{\pi^0} = 600$ MeV/c which corresponds to a recoiling mass of 1109 MeV/c^2 one obtains with $\sigma_p = 15$ MeV/c (table 5) a resolution of $\sigma_m \approx 25$ MeV/c^2. If the measured decay angle θ is larger than θ_{max} which is determined by the mass and momentum of the K_LK_L system then equation 29 yields no solution and the event is rejected. This was the case for 904[253] events. A depletion in the $\pi^0K_LK_L$ Dalitz plot around the maximum decay angle θ_{max} results of the loss of these events.

Equation 29 does not contain information about the sign of $\tan\theta$, and hence 167[55] events were found with $\beta/\beta^* > 1$ but $\theta > \pi/2$. These events had to be rejected since they cannot come from $\pi^0K_LK_L$. Thus, in total, 1,071[308] events were rejected.

The momenta of the K_L's were calculated using the Lorentz transformation back to the laboratory frame. For the interacting K_L one has

$$p_{K_L^{int}} = \sqrt{(p^*\sin\theta^*)^2 + (\gamma(p^*\cos\theta^* + \beta E^*))^2} \tag{36}$$

and for the missing K_L

$$p_{K_L^{miss}} = \sqrt{(p^*\sin(\pi-\theta^*))^2 + (\gamma(p^*\cos(\pi-\theta^*) + \beta E^*))^2}. \tag{37}$$

All kinematic variables in the laboratory frame are then known and thus, the full event has been reconstructed. In this way, 48,993[8,314] $\pi^0K_LK_L$ events were selected.

Table 6 summarizes the $\pi^0K_LK_L$ event selection by listing the number of events after each cut.

6.3 The Dalitz Plot $\pi^0K_LK_L$

The raw $\pi^0K_LK_L$ Dalitz plot is shown in figure 13 for events with at least one PED-PED invariant mass combination in the π^0 main window (48,993 events). No background has been subtracted yet. However, several structures can be observed. Three general features of the Dalitz plot shall be mentionned:

Event type	Number of Events
All-neutral triggered events	13.2×10^6
	$((3.38 \pm 0.26) \times 10^8$ $\overline{p}p$ annihilations)
3 PEDs with $E_{PED} > 20$ MeV	158,413
$\pi^0 + 1$ PED	112,684
After split-off cut	90,728
$m_{miss} > m_{K_L}$ (in region B of fig. 5)	60,983

	Events from π^0 main window	Events from π^0 side-bins (SL+SU)
$m_{miss} > m_{K_L}$ (in region B of fig. 5)	51,954	9,029
$p_{\pi^0} < 666$ MeV/c (or $m_{miss} > 2m_{K_L}$)	50,064	8,622
$\pi^0 K_L K_L$ successfully reconstructed	48,993	8,314

Table 6: *Summary of $\pi^0 K_L K_L$ event selection*

1. The border of the Dalitz plot is sharp because the π^0 was assumed to be at its nominal mass.

2. The Dalitz plot is not symmetric with respect to the two K_L. The difference is largest at high $\pi^0 K_L$ masses where the recoiling K_L is very slow. This can be explained by different detection probabilities for the missing and interacting K_L (section 8.1).

3. At low $K_L K_L$ masses a depletion is observed which is due to not succesfully reconstructed $\pi^0 K_L K_L$ events around the maximum decay angle for the interacting K_L.

Resonances appear as band structures in the Dalitz plot. The density distribution therein depends only on the initial state of the $p\overline{p}$ system and the spin of the resonances. In general, spinless resonances lead to a constant density distribution. The following structures are observed:

1. In $\pi^0 K_L$ the structure around 900 MeV/c^2 (line A) might be identified with the $K^{*0}(896)$ decaying into $\pi^0 K_L$.

2. The $K_L K_L$ system shows several bands indicated by the lines B to D which correspond to the peaks in the π^0 momentum distribution (fig. 10). Region B is located at a $K_L K_L$ mass of about 1300 MeV/c^2. A blob in the middle

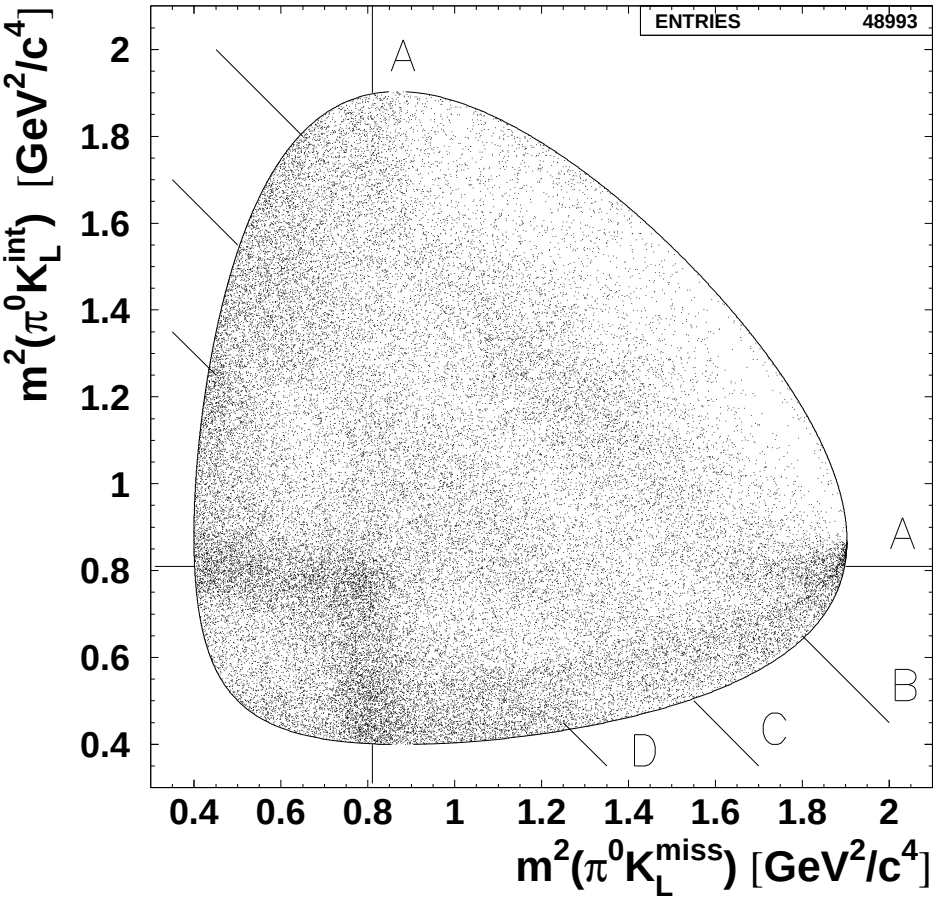

Figure 13: *$\pi^0 K_L K_L$ Dalitz plot where $m^2(\pi^0 K_L^{int})$ is plotted versus $m^2(\pi^0 K_L^{miss})$ (48,993 events). Background is not subtracted yet. The lines are explained in the text.*

and enhancements at both ends of the band indicate the presence of a resonance of spin 2 [4], possibly $f_2(1270)$ and/or $a_2(1320)$.

3. Around 1450 MeV/c^2 (line C) one also observes a band. This region is of particular interest since here one expects $f_0(1370)$ and/or $a_0(1450)$.

4. Region D (around 1520 MeV/c^2) is characterized by enhancements at the border of the Dalitz plot which are typical for a spin 2 resonance such as the $f_2'(1525)$.

Before a partial wave analysis could be done, the background had to be subtracted and the data had to be corrected for acceptance.

7 Background

Three types of background shall be discussed in the following which all concern the $\gamma\gamma$ invariant mass spectrum from which π^0's have been selected[5].

1. Real background consists of events with no real π^0 and is described as events with at least one $\gamma\gamma$ invariant mass combination in either of the two side-bins (SL and SU) but no combination in the π^0 main window.

2. Combinatorial background is due to events with multiple $\gamma\gamma$ combinations in the π^0 main window.

3. Feedthrough background is due to events with a real π^0 but which do not belong to $\pi^0 K_L K_L$.

The aim of this section is to quantify the background contributions to $\pi^0 K_L K_L$ and to subtract them from the $\pi^0 K_L K_L$ data.

[4] The expected angular distributions for resonances of different spin will be discussed in section 9.3.

[5] In the following, each PED is called a γ although it should be reminded that for $\pi^0 K_L K_L$ one PED stems from a K_L interaction and is not a photon.

7.1 Real Background

Figure 14 shows the $\gamma\gamma$ invariant mass spectrum for the combinations that have been assigned to the π^0, i.e. the combination closest to the nominal π^0 mass (one entry per event). A fit using a Gaussian and a fourth order polynomial was done in order to estimate the number of events which have a $\gamma\gamma$ combination in the π^0 main window but which are not π^0's. The results are given in table 7. Since

Fit function : $f = A\,exp(-\frac{(m-m_0)^2}{2\sigma^2}) + a + bm + cm^2 + dm^3$	
Range	105 to 165 MeV/c^2
Number of bins	60
χ^2	175/(60-7)=3.3
A	$2,352 \pm 17$
m_0	(135.03 ± 0.05) MeV/c^2
σ	(6.56 ± 0.05) MeV/c^2

Table 7: *Results of the fit to the $\gamma\gamma$ invariant mass spectrum in figure 14.*

always the $\gamma\gamma$ combination closest to the π^0 mass was assumed to be the real π^0, the width of 6.5 MeV/c^2 is smaller than expected from the experimental resolution (see table 5). The integration of the Gaussian yields about 38,675 genuine π^0's. The poor χ^2 is mainly due to the bad description of the background below 120 MeV/c^2. The number of events in the side-bins is

$$N_{BG}^{side-bins} = 8,314 \text{ events.} \tag{38}$$

Since the upper (lower) boundary of the lower (upper) side-bin is only at 2σ from the π^0 mass, also about 4.5% (or 1,740 events) of the real π^0's contribute to the number of events in the side-bins. However, despite of the fact that the fit does not describe perfectly the background, the integration of the polynomial yields 10,089 events, or 1,775 events more than it is found in the sid-bins. Hence, there is an uncertainty of about 20% on the actual background events under the π^0 peak. The Dalitz plot for the side-bin events (8,314 events) is shown in figure 16. A weak indication for the feedthrough from real $\pi^0 K_L K_L$ events is given where the $K^{*0}(896)$ is expected.

All events with at least one entry in the side-bins and none in the main window

were considered as background with no real π^0. The Dalitz plot based on this type of events was later used for background subtraction.

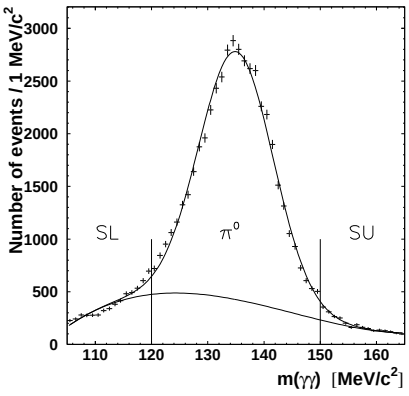

Figure 14: *$\gamma\gamma$ invariant mass spectrum for combinations which have been assigned to the π^0 (1 entry per event). The curve shows the fit. The polynomial decribing the background is superimposed.*

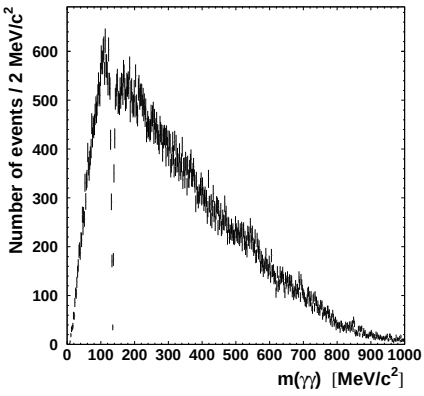

Figure 15: *$\gamma\gamma$ invariant mass spectrum for the other two combinations (2 entries per event).*

7.2 Combinatorial Background

The combinatorics in the π^0 main window and the side-bins is given in table 8: 88.2% of the events have only one $\gamma\gamma$ combination in the π^0 main window and only

Number of $\gamma\gamma$ combinations	Number of events in π^0 main window		Number of events in side-bins (SL+SU)	
	absolute	relative (in%)	absolute	realtive (in%)
≥ 1	48,993	100	8,314	100
1	43,202	88.2	7,258	87.3
2	5,440	11.1	1,009	12.1
3	351	0.7	47	0.6

Table 8: *Combinatorics in the π^0 main window and the side-bins.*

11.1 % have two combinations. The fraction of three combinations is negligible. From the missing events at the π^0 mass in the $\gamma\gamma$ invariant mass spectrum of

the combinations that have not been assigned to the π^0 (fig.15), it was estimated that for about 30 % of all events with $\geq$2 combinations in the main window, the wrong combination was taken. This means that for $30\% \times 11.8\% \approx 3.5\%$ of all $\pi^0 K_L K_L$ events, the π^0 was misidentified.

The Dalitz plots corresponding to 1, 2 and 3 $\gamma\gamma$ invariant mass combinations in the π^0 main window are shown in figures 17,18 and 19 where the combination closest to the π^0 mass has been entered. Events with multiple combinations accumulate at the lower border of the $\pi^0 K_L K_L$ Dalitz plot. This situation corresponds to an interacting K_L collinear to the π^0. Taking the most probable case where the π^0 decays into two photons through the minimum opening angle, the three PEDs would cluster in the same region of the calorimeter. This particular kinematic situation makes it much easier to find several π^0 combinations if the PED energies are about the same. Cleaning up the data sample in the sense by using only events with exactly one π^0 candidate would then distort the Dalitz plot. Therefore, a cut requiring only one π^0 combination in the main window was not applied.

7.3 Feedthrough from Other Channels

Feedthrough events are events with π^0+1 PED events which are not $\pi^0 K_L K_L$. Two contributions were already mentionned in section 6.1:

- $\overline{p}p \rightarrow \omega K_L K_L$ with $\omega \rightarrow \pi^0\gamma$ and both K_L undetected,
- $\overline{p}p \rightarrow K_S K_L^{miss}$ with $K_S \rightarrow 2\pi^0 \rightarrow 4\gamma$ with one γ undetected.

Some of these events also survive the reconstruction for $\pi^0 K_L K_L$ events. It shall now be discussed where these channels appear in the $\pi^0 K_L K_L$ Dalitz plot and which cuts were defined to reject them. Moreover, feedthrough from channels which have branching ratios B larger than the one for $\pi^0 K_L K_L$ was also studied. These are the reactions

- $\overline{p}p \rightarrow \omega\pi^0$, $B = (5.73 \pm 0.47)\,10^{-3}$ [37],
- $\overline{p}p \rightarrow \omega\eta$, $B = (15.1 \pm 1.2)\,10^{-3}$ [37]

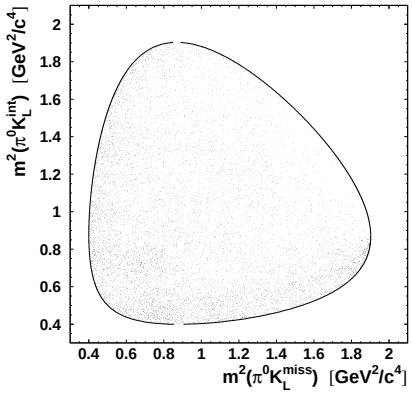

Figure 16: $\pi^0 K_L K_L$ *events with no* $\gamma\gamma$ *combination in the* π^0 *main window but at least one combination in either of the side-bins. This represents the situation of the background under the* π^0 *peak.*

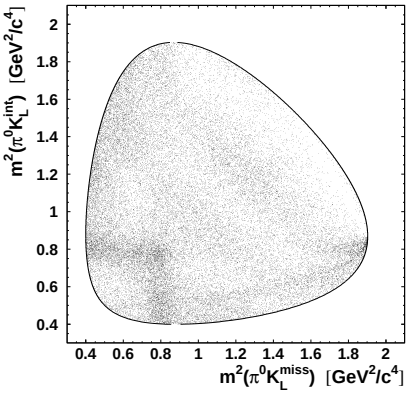

Figure 17: $\pi^0 K_L K_L$ *events with exactly one* $\gamma\gamma$ *combination in the* π^0 *main window.*

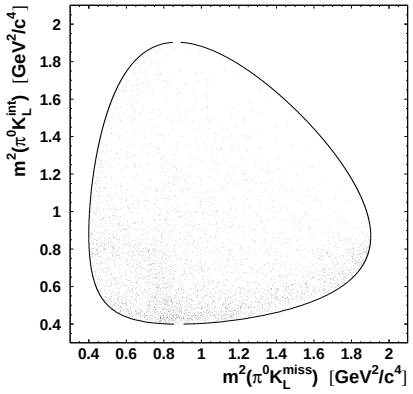

Figure 18: $\pi^0 K_L K_L$ *events with two* $\gamma\gamma$ *combinations in the* π^0 *main window.*

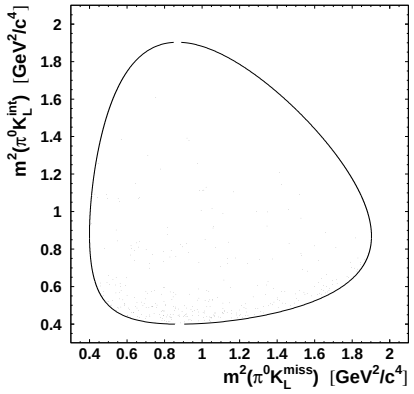

Figure 19: $\pi^0 K_L K_L$ *events with three* $\gamma\gamma$ *combination in the* π^0 *main window.*

- $\overline{p}p \to \pi^0\pi^0\pi^0$, $B = (6.2 \pm 1.0)\,10^{-3}$ [12] and
- $\overline{p}p \to \pi^0\pi^0\eta$, $B = (6.7 \pm 1.2)\,10^{-3}$ [14],

which were simulated with GEANT [39]. Feedthrough probabilities for being interpreted as $\pi^0 K_L K_L$ were deduced.

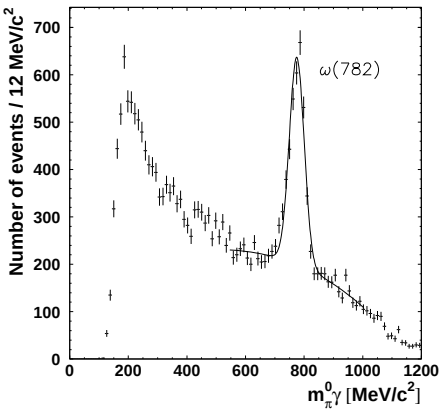

Figure 20: $\pi^0\gamma$ *invariant mass of selected* $\pi^0 K_L K_L$ *events with* $p(3\gamma) <$ 350 *MeV/c. The curve shows the fit.*

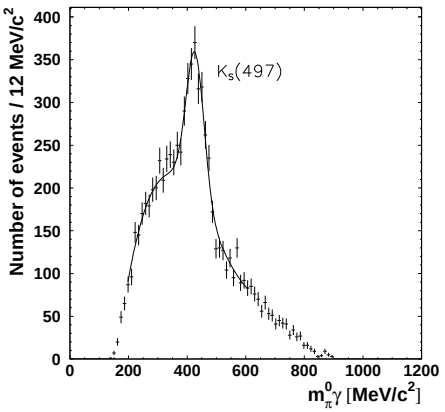

Figure 21: $\pi^0\gamma$ *invariant mass of selected* $\pi^0 K_L K_L$ *events with* $p(3\gamma) >$ 600 *MeV/c. The curve shows the fit.*

7.3.1 $\overline{p}p \to \omega K_L K_L$

From figure 6 one observes that ωX_{miss} events do not extend beyond $p(3\gamma) \approx 350$ MeV/c where $p(3\gamma)$ is the measured total momentum of the 3-PED event. The $\pi^0\gamma$ invariant mass spectrum for events surviving the full $\pi^0 K_L K_L$ reconstruction is shown in figure 20 for $p(3\gamma) < 350$ MeV/c. A fit using a Gaussian on a third order polynomial in the mass range 550 to 1000 MeV/c^2 was performed in order to define the position of the ω peak, the width and the number of ω's in the $\pi^0 K_L K_L$ data sample. The following parameters for the Gaussian were found:

- $m = 775 \pm 1$ MeV/c^2,
- $\sigma = 25 \pm 1$ MeV/c^2,
- $A = 438 \pm 15$ events/bin,

where A is the amplitude. The integration of the Gaussian gives (2287 ± 120) ω's. This is about 4% of the $\pi^0 K_L K_L$ data sample including the events from the π^0 side-bins. The fitted ω mass is 6 MeV/c^2 too low which is due to a slight asymmetry of the ω peak. Events were rejected whenever for a $\pi^0\gamma$ invariant mass $m_{\pi^0\gamma}$

$$\begin{aligned} |m_{\pi^0\gamma}[\mathrm{MeV}/c^2] - 775| &< 40 \text{ and} \\ p_{tot} &< 300 \text{ MeV}/c. \end{aligned} \tag{39}$$

This was true for 2,696[249] events. Again, the number in the brackets gives the number of events from the π^0 side-bins. The width of the mass window was chosen such that about 90% of the $\omega K_L K_L$ events were rejected by the cut. Thus there is a residual background of $10\% \times (2287 \pm 120) = 229 \pm 12$ $\omega K_L K_L$ events in the $\pi^0 K_L K_L$ data.

Figure 22 shows that $\omega K_L K_L$ events are located in a particular region of the $\pi^0 K_L K_L$ Dalitz plot. This is due to the fact that the ω decays into $\pi^0\gamma$ nearly at rest. Consider the case where $p_\omega = 300$ MeV/c for which the momentum range of the π^0 is 240 to 570 MeV/c. The average momentum of 405 MeV/c corresponds to a mass recoiling against the π^0 of 1391 MeV/c^2. The cosine of the minimum opening angle is about -0.7, or +0.7 if interpreted as decay angle of the interacting K_L in the $K_L K_L$ system. This explains the concentration of $\omega K_L K_L$ in a particular region of the $\pi^0 K_L K_L$ Dalitz plot. The decay angular distribution of K_L^{int} in the $K_L K_L$ system for $m(K_L K_L) = 1400 \pm 50$ MeV/c^2 is shown in figure 23. A clear forward/backward asymmetry is visible due to the $\omega K_L K_L$ events which disappears after rejection of these events. The peak at $\cos\theta = -1$ is partly explained by $K_S K_L$ events which will be the subject of the following section.

The ω momentum spectrum of $\omega K_L K_L$ shall be discussed next. It is the first time that such high statistics data are obtained for this channel. For this purpose, the data sample of 60,983 $\pi^0\gamma$ events (table 6) before the reconstruction of $\pi^0 K_L K_L$ events is considered.

In addition to the ω mass window given in eqn. 39, side-bins centered at 715 MeV/c^2 and 835 MeV/c^2, respectively, with a width of 40 MeV/c^2 were defined.

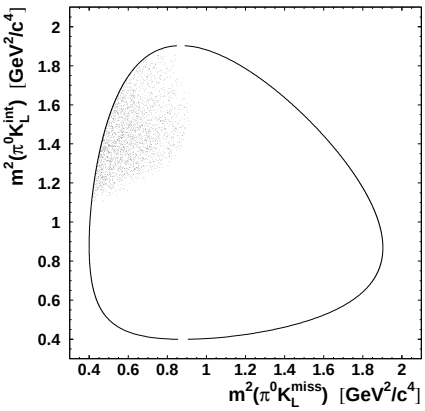

Figure 22: $\pi^0 K_L K_L$ *Dalitz plot for rejected* $\omega K_L K_L$ *events.*

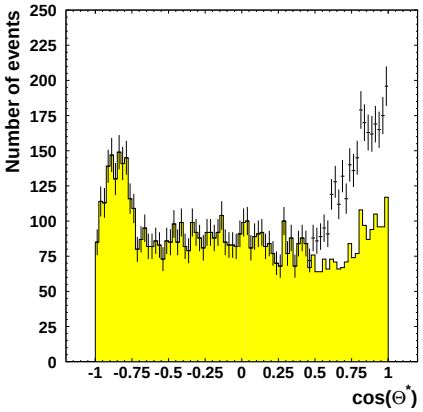

Figure 23: *Decay angular distribution of the interacting* K_L *for* $m(K_L K_L) = 1400 \pm 50$ *MeV/c*^{2}. *The hatched histogram shows the situation after rejection of* $\omega K_L K_L$ *events.*

The momentum distribution of events in the ω main window is shown in figure 24 with the side-bin contributions superimposed. Good agreement is observed above 300 MeV/c. Subtracting the background given by the side-bins yields the ω momentum distribution in the reaction $\overline{p}p \to \omega K_L K_L$ (figure 25). At high ω momenta there is no indication of $a_0(980)$ and/or $f_0(980)$ decaying into $K_L K_L$ although both states were observed in their decay into $\pi\eta$ and $\pi\pi$, respectively, in $\overline{p}p$ annihilation into $\omega\pi\eta$ [40] and $\omega\pi\pi$ [41]. Note, that signals for $a_0(980)$ and $f_0(980)$ were not observed either in the low statistics $\omega K_S K_S$ data of Bizzari et al. [42]. The observation of the absence of a threshold enhancement in the neutral $K\overline{K}$ system with positive C-parity is interesting with respect to the interpretation of the $\pi^0 K_L K_L$ data.

The channel $\omega K_L K_L$ could also contribute to the 3-PED final state if one K_L is undetected, the other K_L interacts giving one PED and the photon from $\omega \to \pi^0\gamma$ escapes through the openings of the calorimeter. Assuming a momentum

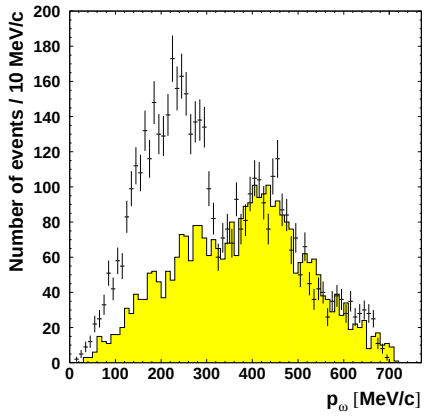

Figure 24: *Momentum distribution of $\pi^0\gamma$ events in the ω main window. The sum of the two side-bin contributions representing the background is superimposed.*

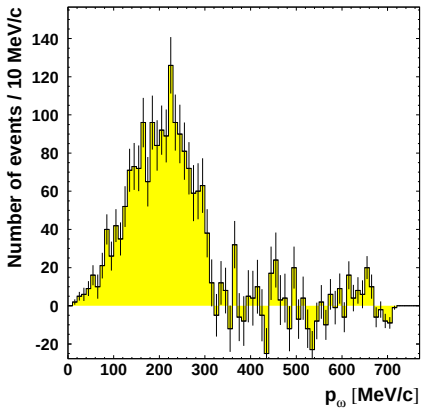

Figure 25: *Same as in figure 24 but after background subtraction. This spectrum corresponds to the momentum distribution of the ω in $\overline{p}p \rightarrow \omega K_L K_L$ at rest.*

independent K_L interaction probability one obtains

$$\frac{\omega K_L^{int} K_L^{miss}}{\omega K_L^{miss} K_L^{miss}} = \frac{2P_0P_1}{P_0^2} = 1.33, \tag{40}$$

where $P_0 = 0.43$ and $P_1 = 0.28$. Using a probability of 2% for loosing a photon due to the solid angle one estimates that

$$\frac{\omega K_L^{int} K_L^{miss} \rightarrow 3 \text{ PED}}{\omega K_L^{miss} K_L^{miss} \rightarrow 3 \text{ PED}} = 2.7 \times 10^{-2}, \tag{41}$$

which corresponds to about 60 events, negligible compared to 2,287 $\omega K_L^{miss} K_L^{miss}$ events.

7.3.2 $\overline{p}p \rightarrow K_S K_L$

The $\pi^0\gamma$ invariant mass spectrum for $\pi^0 K_L K_L$ events with $p_{tot} > 600$ MeV/c (figure 21) shows a K_S signal which was also fitted using a Gaussian and a third order polynomial:

- $m = 427 \pm 2$ MeV/c^2,
- $\sigma = 30 \pm 2$ MeV/c^2,

- $A = 169 \pm 11$ events/bin.

The integration of the signal peak yields $(1,059 \pm 99)$ $K_S K_L$ events. As for $\omega K_L K_L$ events, a K_S main window centered at the fitted mass with a total width of 120 MeV/c^2 and side-bins centered at 340 MeV/c^2 and 520 MeV/c^2 with a width of 60 MeV/c^2 were defined for the K_S momentum distribution shown in figure 26. The contribution of events in the K_S main window is shown with error bars. The sum of the two side-bin contributions is superimposed. The K_S momentum distribution is obtained by subtracting the background given by the side-bins (figure 27). The peak around 800 MeV/c is due to $K_S K_L$. One photon from the decay $K_S \to \pi^0\pi^0 \to 4\gamma$ is not detected which results in a smeared momentum distribution. The sharp cut-off above 800 MeV/c is due to the selection of $\pi^0 K_L K_L$ events with a missing mass larger than m_K. Since the K_S appears significantly only for momenta above 700 MeV/c, $K_S K_L$ events were rejected whenever

$$|m(\pi^0\gamma)[\mathrm{MeV}/c^2] - 430| < 50 \text{ and} \tag{42}$$

$$p_{tot} > 700 \text{ MeV}/c. \tag{43}$$

The width of the mass window in eqn. 42 was chosen such that about 90% of the K_S signal were rejected. Thus, the residual background contamination from $K_S K_L$ is $10\% \times (1,059 \pm 99) = 106 \pm 10$ events. In total 1144[270] events were rejected. The distribution of $K_S K_L$ events in the $\pi^0 K_L K_L$ Dalitz plot (figure 28) also affects the decay angular distribution of the $K_L K_L$ system in the region where $\cos\theta^* \approx -1$ (figure 29). After rejection of both $\omega K_L K_L$ and $K_S K_L$ events, the angular distribution is more symmetric. The remaining asymmetry which is still observed can be explained by the momentum dependent K_L interaction probability (section 8.1).

7.3.3 $\overline{p}p \to \omega\pi^0$

The reaction $\overline{p}p \to \omega\pi^0$, where $\omega \to \pi^0\gamma$ leads to a 5γ final state. This channel contributes to the 3-PED data if two photons escape detection. One can distinguish three possible configurations leading to a $\pi^0\gamma$ event:

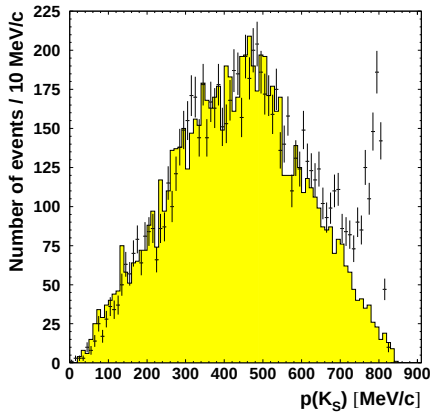

Figure 26: *Momentum distribution of $\pi^0\gamma$ events in the K_S main window. The sum of the two side-bin contributions is superimposed (dark area).*

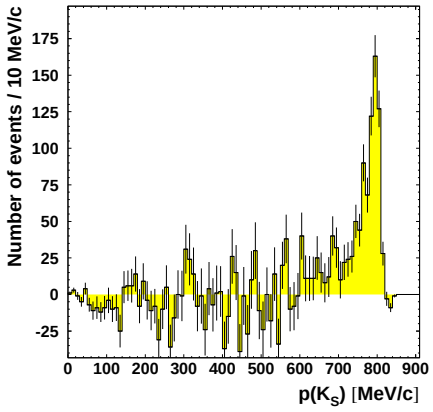

Figure 27: *Same as in figure 26 after background subtraction. The peak corresponds to K_S's from $\overline{p}p \rightarrow K_S K_L$.*

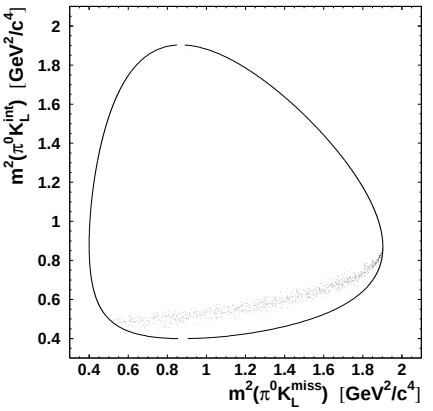

Figure 28: *$\pi^0 K_L K_L$ Dalitz plot for rejected $K_S K_L$ events.*

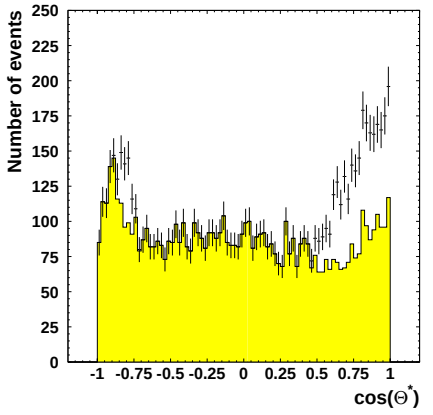

Figure 29: *Decay angular distribution of the interacting K_L for $m(K_L K_L) = 1400 \pm 50$ MeV/c^2. The hatched histogram shows the situation after rejection of $\omega K_L K_L$ and $K_S K_L$ events.*

1. The ω is fully detected while both γ's from the π^0 are lost through the openings of the calorimeter. The ω is monoenergetic and has a momentum of 768 MeV/c. Such an event lies outside the $\pi^0 K_L K_L$ allowed region and was therefore rejected in the selection of $\pi^0 K_L K_L$ events (section 6.1).

2. The ω is not fully detected as the decay π^0 is lost which leads to an event with a recoiling monoenergetic π^0 of 768 MeV/c. Also these events were rejected since the kinematics of $\pi^0 K_L K_L$ allows only π^0 with momenta below 666 MeV/c (section 6.1).

3. The decay photon from the ω and one photon from the π^0 which recoils against the ω are lost. Then, none of the detected particles is monoenergetic. Such an event is difficult to be recognized as originating from $\omega\pi^0$.

The third scenario is the only important case which can contribute to $\pi^0 K_L K_L$ in the 3-PED final state.

A sample of $N_{MC} = 75{,}000$ Monte Carlo $\omega\pi^0$ ($\omega \to \pi^0\gamma$) events was generated using GEANT. These events were reconstructed as $\pi^0 K_L K_L$ events with the same selection criteria as for real data. Cuts introduced for background rejection of $\omega K_L K_L$ and $K_S K_L$ were also applied. The feedthrough probability is calculated by

$$\epsilon(\omega\pi^0) \;=\; \frac{N-n}{N_{MC}} B(\omega \to \pi^0\gamma), \tag{44}$$

where N denotes the number of events found with at least one $\gamma\gamma$ combination in the π^0 main window and n the corresponding number of events from the π^0 side-bins. With $N[n] = 62[20]$ and $B(\omega \to \pi^0\gamma) = (8.5 \pm 0.5) \times 10^{-3}$[29], the branching ratio for ω decay into $\pi^0\gamma$, the feedthrough probability is

$$\epsilon(\omega\pi^0) \;=\; (4.76 \pm 1.06) \times 10^{-5}, \tag{45}$$

from which the absolute contamination in the $\pi^0 K_L K_L$ data sample is deduced:

$$N(\omega\pi^0) \;=\; N_{\overline{p}p} B(\overline{p}p \to \omega\pi^0)\epsilon(\omega\pi^0). \tag{46}$$

The number of $\overline{p}p$ annihilations is $N_{\overline{p}p} = (3.38 \pm 0.26) \times 10^8$ (see *p.*18) and $B(\overline{p}p \to \omega\pi^0) = (5.73 \pm 0.47) \times 10^{-3}$ is the branching ratio of $\overline{p}p$ annihilations at rest into $\omega\pi^0$ [37]. With the numbers given above, this gives

$$N(\omega\pi^0) \;=\; (92 \pm 23) \text{ events.} \tag{47}$$

The feedtrough from $\omega\pi^0$ events is small and does not accumulate significantly in any particular region of the $\pi^0 K_L K_L$ Dalitz plot. Hence, this background is neglegible.

7.3.4 $\overline{p}p \to \omega\eta$

In the same way as for $\omega\pi^0$, feedthrough from $\omega\eta$ was studied on the basis of $N_{MC} = 35{,}000$ GEANT events where $\omega \to \pi^0\gamma$ and $\eta \to \gamma\gamma$: 38[15] events survived the $\pi^0 K_L K_L$ selection. The feedthrough probability for $\omega\eta$ is given by

$$\epsilon(\omega\eta) \;=\; \frac{N-n}{N_{MC}} B(\omega \to \pi^0\gamma) B(\eta \to \gamma\gamma), \tag{48}$$

which yields with $B(\eta \to \gamma\gamma) = (38.8 \pm 0.5) \times 10^{-2}$

$$\epsilon(\omega\eta) \;=\; (2.15 \pm 0.68) \times 10^{-5}. \tag{49}$$

The absolute contamination of $\omega\eta$ events in $\pi^0 K_L K_L$ is

$$N(\omega\eta) \;=\; N_{\overline{p}p} B(\overline{p}p \to \omega\eta) \epsilon(\omega\eta). \tag{50}$$

With $B(\overline{p}p \to \omega\eta) = (15.1 \pm 1.2) \times 10^{-3}$ [37] one obtains

$$N(\omega\eta) \;=\; (110 \pm 37) \text{ events.} \tag{51}$$

Feedthrough events from $\omega\eta$ are randomly distributed over the $\pi^0 K_L K_L$ Dalitz plot and can therefore also be neglected.

7.3.5 $\overline{p}p \to \pi^0\pi^0\pi^0$

To investigate the feedthrough from $3\pi^0$ events, $N_{MC} = 130{,}000$ events were generated using GEANT assuming phase space distribution: 37[6] events survived the full $\pi^0 K_L K_L$ reconstruction. The feedthrough probability is simply

$$\epsilon(3\pi^0) \;=\; \frac{N-n}{N_{MC}}, \tag{52}$$

which yields

$$\epsilon(3\pi^0) \;=\; (2.38 \pm 0.50) \times 10^{-4}, \tag{53}$$

from which the absolute contamination can be derived. With

$$N(3\pi^0) \;=\; N_{\overline{p}p} B(\overline{p}p \to 3\pi^0) \epsilon(3\pi^0) \tag{54}$$

and $B(\overline{p}p \to 3\pi^0) = (6.2 \pm 1.0) \times 10^{-3}$ [12] the number of $3\pi^0$ events in $\pi^0 K_L K_L$ are expected to be

$$N(3\pi^0) \;=\; (500 \pm 138) \text{ events}. \tag{55}$$

This is a substantial amount of feedthrough events but the number of reconstructed events is still too small in order to observe an accumulation in a particular region of the $\pi^0 K_L K_L$ Dalitz plot. In the following it shall be discussed which $3\pi^0$ events can contribute to $\pi^0 K_L K_L$ and how these events are distributed over the $\pi^0 K_L K_L$ Dalitz plot given that these events are <u>not</u> phase space distributed[6] [12].

To be detected as $\pi^0\gamma$ event, one photon from a π^0 decay and one π^0 have to escape detection. For π^0 with momenta $p_{\pi^0} > 635$ MeV/c, the minimum opening angle is smaller than 24° and hence photons from such π^0's can leave the calorimeter through its forward or backward beam openings. The corresponding recoiling mass is about 1050 MeV/c^2. It is found that more than 99% of all phase space distributed $3\pi^0$ events have at least one π^0 with $p_{\pi^0} > 635$ MeV/c and 52% of the events have even two π^0's above this momentum. The momentum range of the third π^0 reaches about 560 MeV/c and peaks around 300 MeV/c. The corresponding recoiling mass distribution ranges from about 1175 MeV/c^2 to the maximum mass of 1741 MeV/c^2. The peak position is around 1520 MeV/c^2.

If feedthrough comes from one undetected π^0 above 635 MeV/c, then the detected π^0 can have a broad momentum distribution. Hence, feedthrough events are scattered over the $\pi^0 K_L K_L$ Dalitz plot. Since the $\pi^0 K_L K_L$ Dalitz plot for

[6] A simulation of $3\pi^0$ events according to the true dynamics [12] would be extremely time consuming due to the low feedthrough probability.

37,358 events (table 9) will be divided into 895 bins in the following analysis, even 500 $3\pi^0$ events in $\pi^0 K_L K_L$ are negligible.

Consider now feedthrough from events having two π^0's with momenta above 635 MeV/c. Since 52% of all $3\pi^0$ events are of this type, the feedthrough probability for these events is $\epsilon'(3\pi^0) \equiv \epsilon(3\pi^0)/0.52$. Figure 30 shows where these events are located in the $3\pi^0$ Dalitz plot. One notices that these are the regions where the $f_0(1500)$ appears in real $3\pi^0$ data [12]. About 1/3 of all real events are found here. The maximum intensity occurs at 1520 MeV/c^2. With these numbers, it is then estimated that the number of real $3\pi^0$ events in $\pi^0 K_L K_L$ is

$$N(3\pi^0, \text{real}) = N_{\overline{p}p} B(\overline{p}p \to 3\pi^0) \epsilon'(3\pi^0) \frac{1}{3} \approx 330 \text{ events.} \tag{56}$$

About 100 bins will be used for the description of the $\pi^0 K_L K_L$ data in the $K\overline{K}$ mass region around 1500 MeV/c^2. This means that $3\pi^0$ events contribute with 3 to 4 entries per bin. For $\pi^0 K_L K_L$ data (37,358 events), the number of entries in these bins varies between 50 to 180 and hence feedthrough from $3\pi^0$ is statistically not significant. Therefore, real $3\pi^0$ events would contribute less feedthrough background than phase space distributed $3\pi^0$ events, hence $N(3\pi^0) = 500$ events is an upper limit.

7.3.6 $\overline{p}p \to \pi^0\pi^0\eta$

Correspondingly, 50,000 $\pi^0\pi^0\eta$ events with η and π^0 decaying into $\gamma\gamma$ were generated with GEANT assuming phase space distribution from which 20[6] events were reconstructed as $\pi^0 K_L K_L$. For the feedthrough probability,

$$\epsilon(\pi^0\pi^0\eta) = \frac{N-n}{N_{MC}} B(\eta \to \gamma\gamma), \tag{57}$$

a value of

$$\epsilon(\pi^0\pi^0\eta) = (1.08 \pm 0.39) \times 10^{-4} \tag{58}$$

was obtained. With

$$N(\pi^0\pi^0\eta) = N_{\overline{p}p} B(\overline{p}p \to \pi^0\pi^0\eta) \epsilon(\pi^0\pi^0\eta), \tag{59}$$

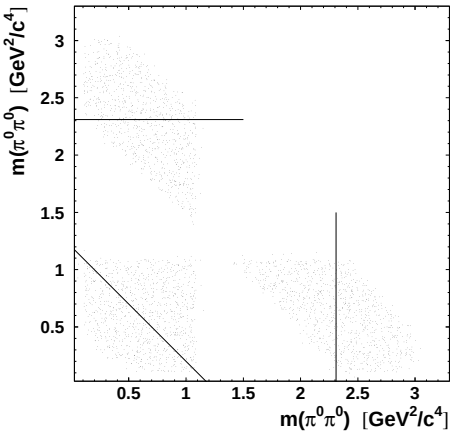

Figure 30: *MC $3\pi^0$ Dalitz plot for events where two pions have momenta above 635 MeV/c. The lines indicate the position of the $f_0(1500)$ in real $3\pi^0$ data.*

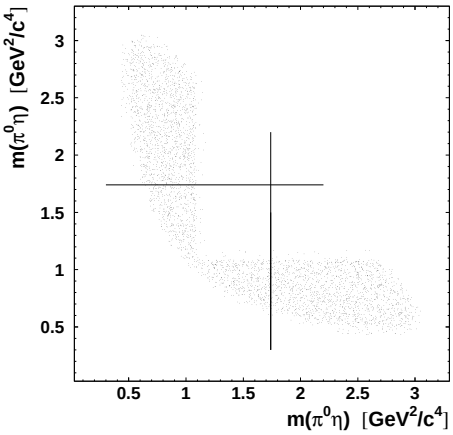

Figure 31: *MC $\pi^0\pi^0\eta$ Dalitz plot for events where one pion has a momentum above 635 MeV/c. The lines indicate the position of the $a_2(1320)$ in real $\pi^0\pi^0\eta$ data.*

where $B(\overline{p}p \to \pi^0\pi^0\eta) = (6.7 \pm 1.2) \times 10^{-3}$ [43], the expected number of feedthrough events from $\pi^0\pi^0\eta$ is

$$N(\pi^0\pi^0\eta) \quad = \quad (245 \pm 100) \text{ events.} \tag{60}$$

As in the case of $3\pi^0$, one photon and one fast π^0 have to be lost which, using the same arguments as above, reduces the critical region of the $\pi^0\pi^0\eta$ Dalitz plot to $\pi^0\eta$ masses below 1050 MeV/c^2 (fig. 31) where in real data only reflections from $a_2(1320)$ contribute significantly [43]. It should be noted that in this particular case, the decay π^0 of the $a_2(1320) \to \pi^0\eta$ is lost while the recoiling π^0 is detected and hence, such an event is interpreted as a $\pi^0 K_L K_L$ event with a $K_L K_L$ mass corresponding to a mass of the $a_2(1320)$. As 58% of the phase space distributed events have one π^0 above 635 MeV/c and assuming that only these events contribute to the feedthrough, the feedthrough probability is $\epsilon'(\pi^0\pi^0\eta) = \epsilon(\pi^0\pi^0\eta)/0.58 = 1.85 \times 10^{-4}$. Using the fraction of $a_2(1320)\pi^0$ events in $\pi^0\pi^0\eta$ ($R = 0.285$) [43] of which about half of them are in the critical region,

it is estimated that the number of real feedthrough events from $\pi^0\pi^0\eta$ events is

$$N(\pi^0\pi^0\eta, \text{real}) = N_{\overline{p}p} B(\overline{p}p \to \pi^0\pi^0\eta)\epsilon'(\pi^0\pi^0\eta)\frac{R}{2} \approx 60 \text{ events}, \qquad (61)$$

which is even less than for $\pi^0\pi^0\eta$ phase space distributed events.

Event type	Number of events in π^0	
	main window	side-bins
$\pi^0 K_L K_L$ (table 6)	48,993	8,314
$\pi^0 K_L K_L$ after cut on $\omega K_L K_L$ events	46,297	8,065
$\pi^0 K_L K_L$ after cut on $K_S K_L$ events	45,153	7,795
$\pi^0 K_L K_L$ after side-bin subtraction [a]	$37,358 \pm 1,575$	
Residual background	absolute	relative
$\omega K_L K_L$	229 ± 12	6.1×10^{-3}
$K_S K_L$	106 ± 10	2.8×10^{-3}
$\omega\pi^0$	92 ± 23	2.5×10^{-3}
$\omega\eta$	110 ± 37	2.9×10^{-3}
$3\pi^0$ (upper limit)	500 ± 138	1.3×10^{-2}
$\pi^0\pi^0\eta$ (upper limit)	245 ± 100	6.6×10^{-3}
Total background contamination in $\pi^0 K_L K_L$	$1,282 \pm 177$	$(3.4 \pm 0.5) \times 10^{-2}$

[a] The error includes the uncertainty of 20% on the actual number of background events from the π^0 side-bins (section 7.1).

Table 9: *Summary of background in* $\pi^0 K_L K_L$.

7.4 Background Subtraction

The contribution of background to $\pi^0 K_L K_L$ is summarized in Table 9. It is reminded that pure phase space was assumed for background channels which have been studied with GEANT. The total residual background is about $(3.4 \pm 0.5)\%$ which is expected not to contribute significantly to any region of the $\pi^0 K_L K_L$ Dalitz plot.

The $\pi^0 K_L K_L$ Dalitz plot for events in the π^0 main window was divided into bins of size (0.045×0.045) $(\text{GeV}^2/c^4)^2$. This gave 895 bins with non-zero entries. The binned Dalitz plot and the corresponding one for π^0 side-bin events (background) are shown in figures 32 and 33. The number of events per bin after

background subtraction is therefore simply given by

$$n = n_S - n_{BG}, \tag{62}$$

where n_S is the number of entries per bin in the signal Dalitz plot and n_{BG} the number of events per bin in the background Dalitz plot. The statistical error on a bin is therefore

$$\sigma_n = \sqrt{n_S + n_{BG}}. \tag{63}$$

The background subtracted $\pi^0 K_L K_L$ Dalitz plot is shown in figure 34.

8 Acceptance Correction of $\pi^0 K_L K_L$ Events

8.1 K_L Interaction in CsI and Survival Probability

Hadronic cross sections for K_L in CsI are not known and hence GEANT simulations are based on model dependent calculations. The K_L interaction in CsI was studied [44] with the two available hadronic packages FLUKA [45] and GHEISHA [46]. The cross sections for K_L diverge for energies below 1 GeV and the interaction probabilities from FLUKA and GHEISHA are incompatible. Although FLUKA seems to give reasonable results for momenta above 300 MeV/c it is definitively wrong at very low momenta [44]. Hence, GEANT was not used to deduce reconstruction efficiencies and acceptance corrections for the $\pi^0 K_L K_L$ data.

In principle, the K_L interaction probability in CsI could be measured directly from Crystal Barrel data:

The reaction $\overline{p}p \to K_S K_L$ was used to determine the K_L interaction probability in CsI [36]. Since the K_L is monoenergetic, this gives only one measurement at 795 MeV/c (see section 6).

The K_L in the three body final state $\pi^0 K_S K_L$ (analogous to $\pi^0 K_L K_L$) has a momentum range between zero and 747 MeV/c. This channel allows the measurement of the interaction probability as a function of momentum. The K_S serves as a tag for K_L. The difficulty lies in the lack of statistics (only 2,834 reconstructed events out of 107×10^6 $\overline{p}p$ annihilations at rest where the K_L is not interacting [47]).

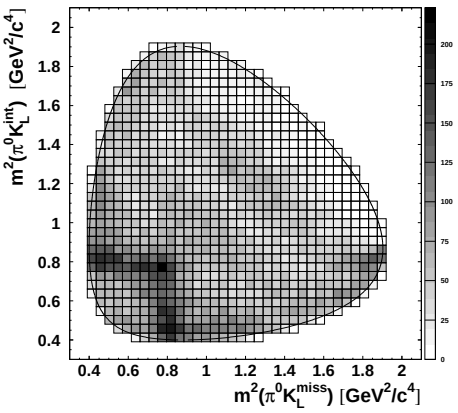

Figure 32: *Binned $\pi^0K_LK_L$ Dalitz plot for signal events (from π^0 main window).*

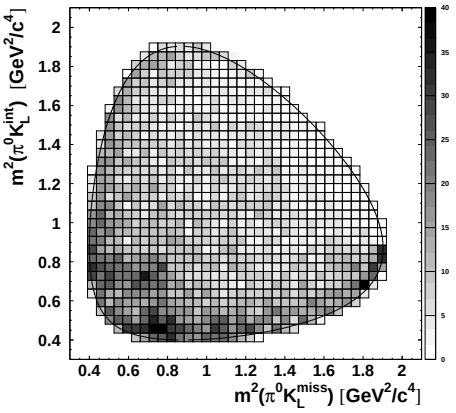

Figure 33: *Binned $\pi^0K_LK_L$ Dalitz plot for background events. (from π^0 side-bins).*

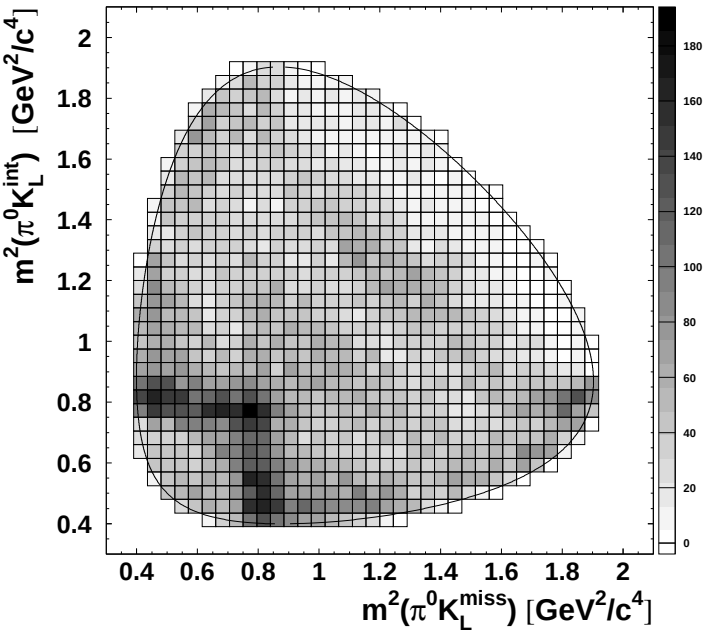

Figure 34: *Dalitz plot $\pi^0K_LK_L$ after background (π^0 side-bin) subtraction.*

The annihilation into $\pi^{\pm}K^{\mp}K_L$ could also be used but the difficulty is the separation of charged kaons and pions at momenta larger than 400 MeV/c. This ambiguity therefore affects the low momentum region of the K_L which is of particular interest.

In this analysis, the variation of the K_L interaction probability with momentum in CsI from was derived directly from data on $\pi^0 K_L K_L$. Since one K_L is interacting and produces one PED with probability P_1 and the other K_L is not detected (probability P_0), the relative K_L interaction probability can be measured[7]:

$$P^{int} = \frac{P_1}{P_1 + P_0}. \tag{64}$$

The momentum distributions of the K_L in the two K^* bands (in a mass window 897$\pm$25 MeV/c^2) were used to determine the interaction probablity. These bands cross the whole Dalitz plot and, hence, the full momentum range is covered. The recoiling K_L has a fixed momentum. Figure 35 shows the background subtracted spectrum of the interacting K_L, superimposed on the spectrum for the missing K_L. The peak around 620 MeV/c is due to K^*K self-interference. The two distributions perfectly agree for momenta above 300 MeV/c which means that the probability to detect a K_L is equal to the probability to miss it, hence $P^{int} \approx 50\%$. At low momenta one observes more events for the interacting K_L than for the missing K_L. The ratio of the momentum spectrum of the interacting K_L to the summed spectrum yields the interaction probability according to eqn. 64. This is shown in figure 36. The K_L decay probability and the π^0 detection efficiency cancel out since they are the same for both the interacting and the missing K_L. The spectrum in figure 36 was fitted by an exponential function and a constant background:

$$P^{int} = A + (1 - A)\, e^{-p(K_L)/B}. \tag{65}$$

The fit gives $A = 0.49 \pm 0.01$ and $B = 145 \pm 28$ MeV/c. This result can be

[7]The determination of the absolute interaction probability including also K_L's producing $\geq$ 2 PEDs was not attempted since the seperation of $\pi^0 K_L K_L$ from background is then very difficult.

compared with the values found in the analysis of $\overline{p}p \to K_S K_L$ [36] where

$$P^{int}(795\,\mathrm{MeV}/c) = \frac{P_1}{P_1 + P_0} = \frac{0.28}{0.28 + 0.43} = 0.39 \pm 0.03. \quad (66)$$

In contrast, here it is found

$$P^{int}(795\,\mathrm{MeV}/c) = \frac{P_1}{P_1 + P_0} = 0.49 \pm 0.01, \quad (67)$$

which agrees with GEANT simulations of K_L interactions using FLUKA [44]. The discrepancy of the two results might be explained by using different cluster definitions between eqn. 67 and eqn. 66.

The full detection probability for a K_L includes the survival probability

$$P_{surv} = e^{-r_0/c\gamma\beta\tau}, \quad (68)$$

where $r_0 = 0.4$ m is the mean distance from the target to the crystals, β the K_L velocity and $\tau = 5.1 \times 10^{-8} s$ its lifetime.

The detection probability $P_{K_L K_L}$ for the system $K_L^{int} K_L^{miss}$ is then

$$P_{K_L K_L} = P_{K_L K_L}(p_{K_{L,1}}, p_{K_{L,2}}) = P^{int}_{K_{L,1}} \times P^{surv}_{K_{L,1}} \times P^{miss}_{K_{L,2}} \times P^{surv}_{K_{L,2}}. \quad (69)$$

The curves of constant detection probability over the $\pi^0 K_L K_L$ Dalitz plot are shown in figure 37.

8.2 π^0 Reconstruction Efficiency

The reconstruction efficiency for $\pi^0 \to \gamma\gamma$ has to be included to correct the $\pi^0 K_L K_L$ data for acceptance. A sample of 10,000 π^0 events was generated with a flat momentum distribution momentum between 0 and 800 MeV/c using GEANT. 2-PED events were selected by requiring PED energies of at least 20 MeV. Events were accepted as π^0's if the $\gamma\gamma$ invariant mass was between 120 and 150 MeV/c^2 which is the π^0 main window used in the $\pi^0 K_L K_L$ data selection. A comparison of the measured π^0 momentum spectrum with the generated box-spectrum yields the momentum dependent π^0 reconstruction efficiency. The result is that the

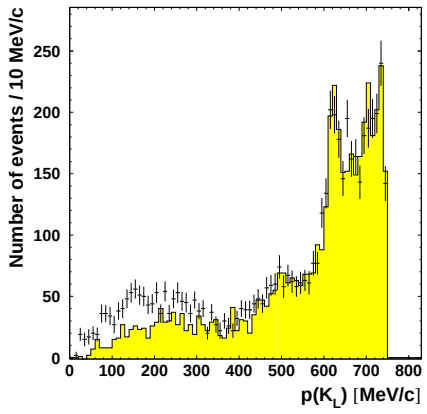

Figure 35: *Momentum distribution of the K_L in the K^* band with error bars for the interacting K_L and hatched for the missing K_L.*

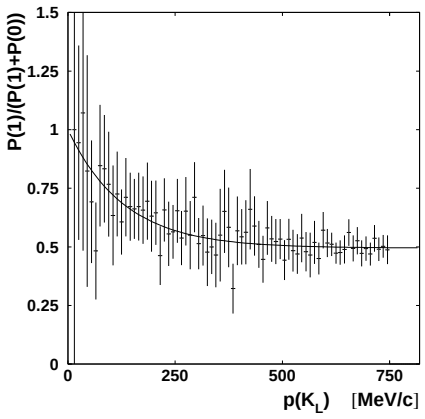

Figure 36: *Interaction probability for K_L in CsI.*

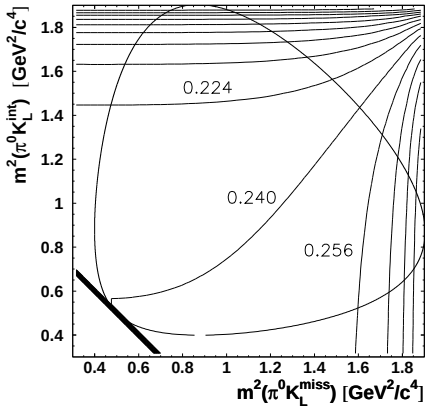

Figure 37: *Curves of constant detection*
probability over the $\pi^0 K_L K_L$ Dalitz plot considering only the two K_L.

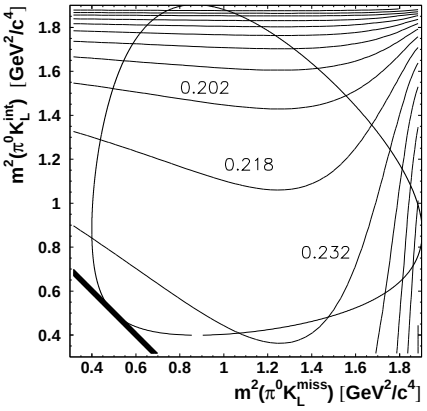

Figure 38: *Same as fig. 37 but including the correction for π^0 probability.*

reconstruction efficiency decreases in good approximation linearly with momentum:

$$\epsilon_{\pi^0}/\epsilon(0) = 1 - a\, p_{\pi^0}[\mathrm{MeV}/c] \quad \text{with} \tag{70}$$

$$a = (2.0 \pm 0.7) \times 10^{-4}\ (\mathrm{MeV}/c)^{-1}. \tag{71}$$

Figure 38 shows the curves of constant acceptance $P_{K_L K_L} \times \epsilon_{\pi^0}$ including both the $K_L K_L$ detection probability and the π^0 reconstruction efficiency. The correction function c for the acceptance is then

$$c = c(p_{K_{L,1}}, p_{K_{L,2}}, p_{\pi^0}) = [P_{K_L K_L} \times \epsilon_{\pi^0}]^{-1}. \tag{72}$$

Since the background subtracted $\pi^0 K_L K_L$ Dalitz plot was divided into bins, the correction function was applied to the center of each bin for which the momenta of the three particles were calculated.

The background subtracted and acceptance corrected Dalitz plot $\pi^0 K_L K_L$ is shown in figure 39. The same Dalitz plot is shown as con plot in figure 40. The scale is 12 events per level.

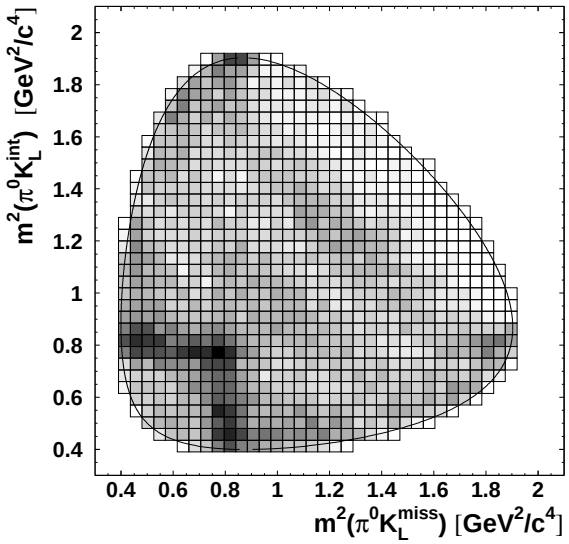

Figure 39: $\pi^0 K_L K_L$ *Dalitz plot after background subtraction and acceptance correction.*

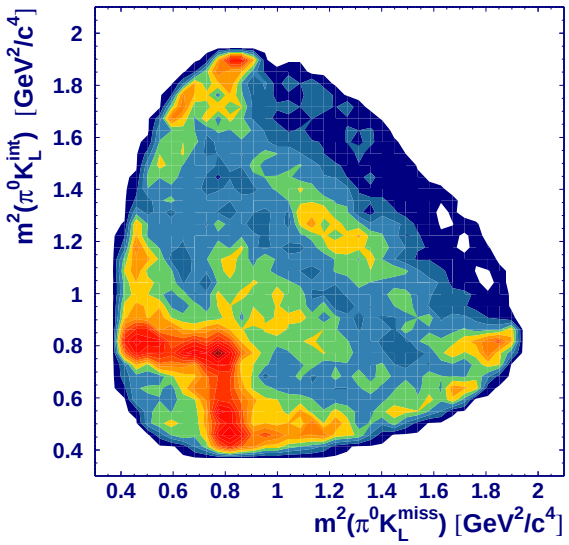

Figure 40: *Same as fig. 39 but as contour plot.*

9 Partial Wave Analysis of $\overline{p}p \to \pi^0 K_L K_L$

9.1 Isospin Decomposition for $\overline{p}p \to \pi K \overline{K}$

The internal symmetries of the $\pi^0 K_L K_L$ final state are discussed on the basis of isospin decomposition. The main feature is the self-interference of K^*K intermediate states. Therefore, the isospin decomposition of the $\pi K \overline{K}$ final state according to the $K\pi$ coupling scheme is given from which the self interference of the K^*K amplitudes can be deduced. The discussion is restricted to the $I = 1/2$ $K\pi$ states since only the corresponding $I = 1/2$ resonances $K^*(892)$ and $K_0^*(1430)$ will be relevant for the fit of the $\pi^0 K_L K_L$ Dalitz plot.

The isospin dubletts for the kaons are:

$$\begin{pmatrix} K^+ \\ K^0 \end{pmatrix} \quad \begin{pmatrix} \overline{K}^0 \\ -K^- \end{pmatrix} \quad \begin{matrix} i_3 = \frac{1}{2} \\ i_3 = -\frac{1}{2}. \end{matrix} \tag{73}$$

The coupling of $K\pi$ to K^* with $I = 1/2$ is considered first. The total wave function is a superposition of all possible charge combinations with couplings given by the Clebsch-Gordan coefficients $\langle J\, M | j_1\, j_2\, m_1\, m_2 \rangle$:

- $|K^{*+}\rangle = \alpha |K^+\pi^0\rangle + \beta |K^0\pi^+\rangle$
  $\alpha = \langle \frac{1}{2}\,\frac{1}{2} | \frac{1}{2}\,1\,\frac{1}{2}\,0 \rangle = +\sqrt{1/3}$
  $\beta = \langle \frac{1}{2}\,\frac{1}{2} | \frac{1}{2}\,1\,-\frac{1}{2}\,1 \rangle = -\sqrt{2/3}$

$$|K^{*+}\rangle \;=\; \frac{1}{\sqrt{3}}(|K^+\pi^0\rangle - \sqrt{2}|K^0\pi^+\rangle), \tag{74}$$

- $|K^{*-}\rangle = \alpha |K^-\pi^0\rangle + \beta |\overline{K}^0\pi^-\rangle$
  $\alpha = \langle \frac{1}{2}\,-\frac{1}{2} | \frac{1}{2}\,1\,-\frac{1}{2}\,0 \rangle = -\sqrt{1/3}$
  $\beta = \langle \frac{1}{2}\,-\frac{1}{2} | \frac{1}{2}\,1\,\frac{1}{2}\,-1 \rangle = +\sqrt{2/3}$

$$|K^{*-}\rangle = \frac{1}{\sqrt{3}}(-|K^-\pi^0\rangle + \sqrt{2}|\overline{K}^0\pi^-\rangle), \tag{75}$$

- $|K^{*0}\rangle = \alpha |K^+\pi^-\rangle + \beta |K^0\pi^0\rangle$
  $\alpha = \langle \frac{1}{2}\,-\frac{1}{2} | \frac{1}{2}\,1\,\frac{1}{2}\,-1 \rangle = +\sqrt{2/3}$

$\beta = \langle \frac{1}{2}\ -\frac{1}{2} | \frac{1}{2}\ 1\ -\frac{1}{2}\ 0 \rangle = -\sqrt{1/3}$

$$|K^{*0}\rangle = \frac{1}{\sqrt{3}}(-|K^0\pi^0\rangle + \sqrt{2}|K^+\pi^-\rangle), \tag{76}$$

- $|\overline{K}^{*0}\rangle = \alpha|K^-\pi^+\rangle + \beta|\overline{K}^0\pi^0\rangle$
  $\alpha = \langle \frac{1}{2}\ \frac{1}{2} | \frac{1}{2}\ 1\ -\frac{1}{2}\ 1 \rangle = -\sqrt{2/3}$
  $\beta = \langle \frac{1}{2}\ \frac{1}{2} | \frac{1}{2}\ 1\ \frac{1}{2}\ 0 \rangle = +\sqrt{1/3}$

$$|\overline{K}^{*0}\rangle \ = \ \frac{1}{\sqrt{3}}(|\overline{K}^0\pi^0\rangle - \sqrt{2}|K^-\pi^+\rangle). \tag{77}$$

Next are the couplings to the intermediate states $K^*\overline{K}$ and $\overline{K}^*K$, which is either $I = 0$ or $I = 1$. Since the analysis is based on data from $\overline{p}p$ annihilations, only couplings to $i_3 = 0$ are considered:

- $|K^*\overline{K}\rangle_I = \alpha|K^{*+}K^-\rangle_I + \beta|K^{*0}\overline{K}^0\rangle_I$
  $I = 0$: $\alpha = \langle 0\,0 | \frac{1}{2}\ \frac{1}{2}\ \frac{1}{2}\ -\frac{1}{2} \rangle = +\sqrt{1/2}$
  $\beta = \langle 0\,0 | \frac{1}{2}\ \frac{1}{2}\ -\frac{1}{2}\ \frac{1}{2} \rangle = -\sqrt{1/2}$

  $I = 1$: $\alpha = \langle 1\,0 | \frac{1}{2}\ \frac{1}{2}\ \frac{1}{2}\ -\frac{1}{2} \rangle = +\sqrt{1/2}$
  $\beta = \langle 1\,0 | \frac{1}{2}\ \frac{1}{2}\ -\frac{1}{2}\ \frac{1}{2} \rangle = +\sqrt{1/2}$

$$|K^*\overline{K}\rangle_I \ = \ \frac{1}{\sqrt{2}}(|K^{*+}K^-\rangle_I + (-1)^{I+1}|K^{*0}\overline{K}^0\rangle_I), \tag{78}$$

- $|\overline{K}^*K\rangle_I = \alpha|K^{*-}K^+\rangle_I + \beta|\overline{K}^{*0}K^0\rangle_I$
  $I = 0$: $\alpha = \langle 0\,0 | \frac{1}{2}\ \frac{1}{2}\ -\frac{1}{2}\ \frac{1}{2} \rangle = -\sqrt{1/2}$
  $\beta = \langle 0\,0 | \frac{1}{2}\ \frac{1}{2}\ \frac{1}{2}\ -\frac{1}{2} \rangle = +\sqrt{1/2}$

  $I = 1$: $\alpha = \langle 1\,0 | \frac{1}{2}\ \frac{1}{2}\ -\frac{1}{2}\ \frac{1}{2} \rangle = +\sqrt{1/2}$
  $\beta = \langle 1\,0 | \frac{1}{2}\ \frac{1}{2}\ \frac{1}{2}\ -\frac{1}{2} \rangle = +\sqrt{1/2}$

$$|\overline{K}^*K\rangle_I \ = \ \frac{1}{\sqrt{2}}((-1)^{I+1}|K^{*-}K^+\rangle_I + |\overline{K}^{*0}K^0\rangle_I). \tag{79}$$

Since the $\overline{p}p$ system has definite C-parity it is necessary to consider C eigenstates of K^*K. With $I_{K^*} = 1/2$ and $I = I_{K^*K} = I_{\overline{p}p} = 0, 1$ the eigentstates $\Phi^C_{I,I_{K^*}}$ are

$$\begin{aligned}\Phi^C_{0,\frac{1}{2}} &= |K^*\overline{K}\rangle_{I=0} + C|\overline{K}^*K\rangle_{I=0} \\ &= \frac{1}{\sqrt{6}}\left\{\begin{array}{c} |K^+\pi^0K^-\rangle + |K^0\pi^0\overline{K}^0\rangle \\ -\sqrt{2}(|K^0\pi^+K^-\rangle + |K^+\pi^-\overline{K}^0\rangle) \\ +C[|K^-\pi^0K^+\rangle + |\overline{K}^0\pi^0K^0\rangle \\ -\sqrt{2}(|\overline{K}^0\pi^-K^+\rangle + |K^-\pi^+K^0\rangle)] \end{array}\right\} \end{aligned} \tag{80}$$

and

$$\begin{aligned}\Phi^C_{1,\frac{1}{2}} &= |K^*\overline{K}\rangle_{I=1} + C|\overline{K}^*K\rangle_{I=1} \\ &= \frac{1}{\sqrt{6}}\left\{\begin{array}{c} |K^+\pi^0K^-\rangle - |K^0\pi^0\overline{K}^0\rangle \\ -\sqrt{2}(|K^0\pi^+K^-\rangle - |K^+\pi^-\overline{K}^0\rangle) \\ +C[-|K^-\pi^0K^+\rangle + |\overline{K}^0\pi^0K^0\rangle \\ -\sqrt{2}(-|\overline{K}^0\pi^-K^+\rangle + |K^-\pi^+K^0\rangle)] \end{array}\right\}. \end{aligned} \tag{81}$$

The $\pi K\overline{K}$ final state is symmetric with respect to the interchange of the kaons if the G parity of the $\overline{p}p$ system is $G = (-1)^I C = +1$ or it is antisymmetric if $G = -1$. For a particular charge configuration of the $\pi K\overline{K}$ final state one has therefore

- constructive interference between the $K^*\overline{K}$ and $\overline{K}^*K$ amplitudes if $G_{\overline{p}p} = +1$, or
- destructive interference between the $K^*\overline{K}$ and $\overline{K}^*K$ amplitudes if $G_{\overline{p}p} = -1$.

The relative phase between the two amplitudes then is $\phi = 0°$ or $\phi = 180°$, respectively.

The isospin decomposition of $\pi K\overline{K}$ can also be done according to the $K\overline{K}$ coupling scheme. With $I_{K\overline{K}}$ the isospin of the $K\overline{K}$ system, the C eigenstates $\Psi^C_{I,I_{K\overline{K}}}$ are given by

$$\Psi^C_{0,1} = -\frac{1}{\sqrt{6}}\left\{\begin{array}{c} |\pi^0K^+K^-\rangle + |\pi^0K^0\overline{K}^0\rangle \\ -\sqrt{2}(|\pi^+K^0K^-\rangle + |\pi^-K^+\overline{K}^0\rangle) \\ +C[|\pi^0K^-K^+\rangle + |\pi^0\overline{K}^0K^0\rangle \\ -\sqrt{2}(|\pi^-\overline{K}^0K^+\rangle + |\pi^+K^-K^0\rangle)] \end{array}\right\}, \tag{82}$$

$$\Psi^C_{1,0} = \frac{1}{\sqrt{2}} \left\{ \begin{array}{c} |\pi^0 K^+ K^-\rangle - |\pi^0 K^0 \overline{K}^0\rangle \\ +C(|\pi^0 K^- K^+\rangle - |\pi^0 \overline{K}^0 K^0\rangle) \end{array} \right\}, \quad (83)$$

$$\Psi^C_{1,1} = \frac{1}{\sqrt{2}} \left\{ \begin{array}{c} |\pi^+ K^0 K^-\rangle - |\pi^- K^+ \overline{K}^0\rangle \\ +C(|\pi^- \overline{K}^0 K^+\rangle - |\pi^+ K^- \overline{K}^0\rangle) \end{array} \right\}. \quad (84)$$

The results of the isospin decomposition are summarized for the particular case of $\overline{p}p(^1S_0) \to \pi^0 K_L K_L$:

- The G parity of the $\overline{p}p$ initial state $^1S_0(J^{PC} = 0^{-+})$ is $G = (-1)^{I_{\overline{p}p}}$.
- The self-interference of the K^*K amplitudes (with the same quantum numbers J^{PC}) is constructive for $I_{\overline{p}p} = 0$ and destructive for $I_{\overline{p}p} = 1$.
- $K\overline{K}$ resonances with $I_{K\overline{K}} = 0$ are produced from the $I_{\overline{p}p} = 1$ initial state.
- $K\overline{K}$ resonances with $I_{K\overline{K}} = 1$ are produced from the $I_{\overline{p}p} = 0$ initial state.

9.2 Transition Amplitudes

The $\pi^0 K_L K_L$ data were analyzed in the helicity formalism [48] in terms of the isobar model [49], in which the $\overline{p}p$ system is assumed to decay to the 3-body final state $\pi^0 K_L K_L$ through a two-body intermediate state:

$$\overline{p}p \to AB,\ A \to A_1 A_2. \quad (85)$$

In the helicity formalism an isobar A of spin J decays into two daughters A_1, A_2 of spin S_1 and S_2. The daughters have total spin S and relative angular momentum L. The decay amplitude for $A \to A_1 A_2$ is given by the matrix:

$$A(J, LS) = D^J_{\lambda M}(\theta, \phi) < J\lambda | LS0\lambda >< S\lambda | S_1 S_2 \lambda_1, -\lambda_2 > \hat{F}(m). \quad (86)$$

The row index $\lambda = \lambda_1 - \lambda_2$ runs over $(2S_1 + 1)(2S_2 + 1)$ final state helicities while the column index M runs over $(2J + 1)$ magnetic substates of the isobar. The angles θ and ϕ refer to the decay angles in the isobar rest frame. The total transition amplitude A_i of a whole decay chain i is the product of the matrices $A(J, LS)$ of each two-body decay [50], hence one matrix for $\overline{p}p \to AB$ and one

matrix for $A \to A_1 A_2$. $\hat{F}(m)$ is the dynamical function, usually a Breit-Wigner amplitude [38][41]. In this work, the P-vector approach [51][52] in the K-matrix formalism was used to describe resonances of the same quantum numbers within a partial wave.

Assuming dominance of annihilation from $\overline{p}p$ S-states in liquid hydrogen [53], only the ${}^1S_0(J^{PC} = 0^{-+})$ initial state contributes to $\pi^0 K_L K_L$. Thus, the total transition probability for an event j is the coherent sum of the transition amplitudes A_i:

$$w_j \;=\; tr\,|\sum_i \alpha_i A_{ij}({}^1S_0)|^2 \times w_{j,PS}, \tag{87}$$

where $w_{j,PS}$ is the phase space weight of the final state and $\alpha_i = a_i\, e^{i\phi_i}$ are unknown coefficients which have to be determined by the fit.

9.2.1 Dynamical Function: P-Vector Approach

In the isobar model, a resonance α couples directly to the $\overline{p}p$ vertex and decays into a two-body state i with a probability proportional to the partial width $\Gamma_{\alpha i}$. Following Aitchison [51] the dynamical function is given by

$$\hat{F} \;=\; (I - i\rho\hat{K})^{-1}\hat{P}, \tag{88}$$

where the K-matrix is defined as a sum of poles describing all contributing resonances:

$$\hat{K_{ij}} \;=\; \sum_\alpha \frac{g_{\alpha i} g_{\alpha j}}{m_\alpha^2 - m^2}\, \frac{B_L(q_i(m))}{B_L(q_i(m_\alpha)}\, \frac{B_L(q_j(m))}{B_L(q_j(m_\alpha)}. \tag{89}$$

The couplings g_{α_i} are given by the partial widths $\Gamma_{\alpha i}$:

$$g_{\alpha i}^2 \;=\; \frac{m_\alpha \Gamma_{\alpha i}}{\rho_i(m_\alpha)}, \tag{90}$$

where $\rho_i = 2q_i/m$ is the dimensionless two-body phase space factor for the decay into a particular channel i, $B_L(q)$ are the Blatt-Weisskopf damping factors suppressing decays at high angular momenta [54]:

$$B_0(q) \;=\; 1,$$

$$B_1(q) = \sqrt{\frac{2z}{z+1}},$$
$$B_2(q) = \sqrt{\frac{13z^2}{(z-3)^2+9z}}, \tag{91}$$

where $z = (q[\mathrm{MeV}/c]/197.3)^2$ and q is the break-up momentum of the daughter particles at the mass m. The total width Γ_α is the sum of the partial widths:

$$\Gamma_\alpha = \sum_i \Gamma_{\alpha i}. \tag{92}$$

The production vector $\hat{P}$ has the same poles as the K-matrix but the couplings $g_{\alpha i}$ to the initial channels are replaced by a coupling β_α^0 to the the annihilation vertex of the $\overline{p}p$ system:

$$\hat{P}_j = \sum_\alpha \frac{\beta_\alpha^0 g_{\alpha j}}{m_\alpha^2 - m^2} \frac{B_L(q_j(m))}{B_L(q_j(m_\alpha)}. \tag{93}$$

With

$$\beta_\alpha^0 = \beta_\alpha \sqrt{\textstyle\sum_i g_{\alpha i}^2}\,, \tag{94}$$

the coupling or production amplitude β_α is dimensionless.

The dynamical functions $\hat{F}$ for the cases of (i) one resonance coupling to one decay channel, (ii) one resonance coupling to two decay channels and (iii) two resonances both coupling to one decay channel are given explicitely since they are relevant for the analysis of $\overline{p}p \to \pi^0 K_L K_L$.

(i) For one resonance with mass m_0 and width Γ_0 decaying into one channel, one has

$$\hat{K} = \frac{B_L^2(q)}{B_L^2(q_0)} \frac{m_0\Gamma_0/\rho_0}{m_0^2 - m^2}, \tag{95}$$
$$\hat{P} = \beta \frac{B_L(q)}{B_L(q_0)} \frac{m_0\Gamma_0/\rho_0}{m_0^2 - m^2} \tag{96}$$

which yields for the dynamical function

$$\hat{F} = \beta \frac{B_L(q)}{B_L(q_0)} \frac{m_0\Gamma_0/\rho_0}{m_0^2 - m^2 - i m_0\Gamma(m)}, \tag{97}$$

where the mass dependent width is given by

$$\Gamma(m) = \Gamma_0 \frac{\rho}{\rho_0} \frac{B_L^2(q)}{B_L^2(q_0)}. \quad (98)$$

This is the usual relativistic Breit-Wigner amplitude as obtained from the T-matrix $\hat{T} = (I - i\rho\hat{K})^{-1}\hat{K}$. In the formulation of the transition amplitudes, the production amplitude β and $B_L(q_0)$ in eqn. 97 are absorbed in the complex coefficient α of eqn. 87.

(ii) For one resonance and two open decay channels the resulting dynamical function is the the Flatté formula [55]. The example is given for the case where the daughter particles are in a relative S-wave ($L = 0$), i.e. $B_0(q) = 1$. The resonance couples to the two-body final state with couplings proportional to the partial widths Γ_1 and Γ_2. If the resonance is observed in channel 1, one obtains

$$\hat{F}_1 = \beta \frac{m_0\Gamma_1/\rho_1^0}{m_0^2 - m^2 - i\rho_1 m_0(\Gamma_1/\rho_1^0 + \Gamma_2/\rho_2^0)}. \quad (99)$$

For resonances above thresholds the phase space factors ρ_i become 1. In this case, the sum of partial witdths in the denominator of eqn. 99 is the total width and the Flatté formula is equivalent to the Breit-Wigner amplitude of eqn. 97.

(iii) For two resonances with masses m_1 and m_2 and widths Γ_1 and Γ_2 both coupling to one channel it is assumed that the final state particles are in a relative S-wave. The K-matrix and the P-vector are

$$\hat{K} = \frac{m_1\Gamma_2/\rho_1^0}{m_0^2 - m^2} + \frac{m_2\Gamma_2/\rho_2^0}{m_2^2 - m^2}, \quad (100)$$

$$\hat{P} = \beta_1 \frac{m_1\Gamma_1/\rho_1^0}{m_1^2 - m^2} + \beta_2 \frac{m_2\Gamma_2/\rho_2^0}{m_2^2 - m^2}. \quad (101)$$

The production amplitude is then

$$\hat{F} = \beta_1 \frac{m_1\Gamma_1/\rho_1^0}{m_1^2 - m^2 - i\rho_1(m_1\Gamma_1/\rho_1^0 + \Delta_{12})} + \beta_2 \frac{m_2\Gamma_2/\rho_2^0}{m_2^2 - m^2 - i\rho_2(m_2\Gamma_2/\rho_2^0 + \Delta_{21})}, \quad (102)$$

where an overlap term for the two resonances has been introduced:

$$\Delta_{12} = \frac{m_1^2 - m^2}{m_2^2 - m^2}\frac{m_2\Gamma_2}{\rho_2^0},$$

$$\Delta_{21} = \frac{m_2^2 - m^2}{m_1^2 - m^2}\frac{m_1\Gamma_1}{\rho_1^0}. \quad (103)$$

The production amplitude in eqn. 102 reduces to the sum of two Breit-Wigner amplitudes if the resonances are wide apart and/or the resonances are narrow such that the overlap is small ($\Delta_{12} = \Delta_{21} \approx 0$).

It is important to note that, in general, the K-matrix poles correspond to the masses where the intensity $|\hat{F}|^2$ has its maxima and not necessarily to the masses of the resonances. The widths of these maxima are related to Γ_1 and Γ_2. The resonance parameters m_R and Γ_R are given by the complex poles of of the T-matrix

$$\hat{T} \;=\; (I - i\rho\hat{K})^{-1}\hat{K} \tag{104}$$

in the complex energy plane [56]. It is shown below how the determination of the resonance parameters is done in practice.

The advantage of the K-matrix formalism is that unitarity of the S-matrix is always preserved.

9.3 Transition Amplitudes for $\overline{p}p(^1S_0) \to \pi^0 K_L K_L$

9.3.1 $\overline{p}p(^1S_0) \to (\pi^0 K_L)_P K_L$

The $K^{*0}(896)$ decays into $\pi^0 K_L$ in a relative P-wave ($l = 1$). It is the only resonance which occurs in the $(\pi^0 K_L)_P$ wave and hence a relativistic Breit-Wigner amplitude was used for the dynamical function (eqn. 97). The quantum numbers of the $K^{*0}(896)$ are $J^P = 1^-$ and in order to couple to the $^1S_0(J^{PC} = 0^{-+})$ initial $\overline{p}p$ state, the relative angular momentum between the K^* and the recoiling $K_L(J^P = 0^-)$ is $L = 1$. Since the $\overline{p}p$ initial state has $J = 0$, only amplitudes with helicities $\lambda = 0$ contribute to the total transition amplitude. With $A(J, LS)$ and $A'(j, ls)$ describing the decay of the $\overline{p}p$ system and the resonance, respectively, one obtains for the total transition amplitude:

$$\begin{aligned} A(\overline{p}p(^1S_0) \to K^*K) \;&=\; A'(1,10)A(0,10) \\ &=\; -\frac{1}{\sqrt{3}}\cos\theta B_1(Q)B_1(q)\frac{m_0\Gamma_0/\rho_0}{m_0^2 - m^2 - im_0\Gamma(m)} \end{aligned} \tag{105}$$

where θ is the decay angle in the rest frame of the resonance. The break-up momenta for the $\overline{p}p$ system and the resonance are given by Q and q. It is noted

that the dynamical function for the decay of the $\overline{p}p$ system is simply given by $\hat{F}_{\overline{p}} = B_L(Q)$.

From the isospin decomposition of the $\pi K\overline{K}$ final state follows constructive interference between the K^*K and KK^* amplitudes for $I_{\overline{p}p} = 0$ and destructive interference for $I_{\overline{p}p} = 1$, i.e.

$$A(\overline{p}p(^1S_0, I = 0) \to K^*K) = A(\overline{p}p(^1S_0, I = 0) \to KK^*) \text{ and} \quad (106)$$

$$A(\overline{p}p(^1S_0, I = 1) \to K^*K) = -A(\overline{p}p(^1S_0, I = 1) \to KK^*). \quad (107)$$

9.3.2 $\overline{p}p(^1S_0) \to (\pi^0 K_L)_S K_L$

The phase shift for $K\pi$ scattering has been determined by the LASS experiment in the reaction $K^-p \to K^-\pi^+n$ [57]. The phase shift δ and the scattering amplitude $|T|$ for the $I = 1/2$ $(K\pi)_S$ wave from [57] are shown in figures 41 and 42. The errors correspond approximately to the size of the points. The $I = 1/2$ $(K\pi)_S$ wave includes the $K^*(1430)$ with a mass and width of 1429 ± 6 MeV/c^2 and 287 ± 23 MeV/c^2[57], respectively, and the low energy $(K\pi)_S$ interaction which is described in the effective range approximation

$$q \cot \delta = \frac{1}{a} + \frac{bq^2}{2}\ , \quad (108)$$

where q denotes the break-up momentum in the $K\pi^0$ channel, a the scattering length and b the effective range. Aston et al. [57] found for the scattering length $a = (2.02 \pm 0.86)$ $(\mathrm{GeV}/c)^{-1}$ and for the effective range $b = (0.65 \pm 0.47)$ $(\mathrm{GeV}/c)^{-1}$.

To include the $(K\pi)_S$ wave in the F-vector, the $I = 1/2$ $(K\pi)_S$ phase shift from Aston et al. [57] was refitted by using the K-matrix formalism. With

$$K = \rho\hat{K} = \tan\delta, \quad (109)$$

the effective range approximation in the K-matrix formalism can be written as

$$\hat{K}^{-1} = \rho \cot \delta = \frac{2}{am} + \frac{bq^2}{m}, \quad (110)$$

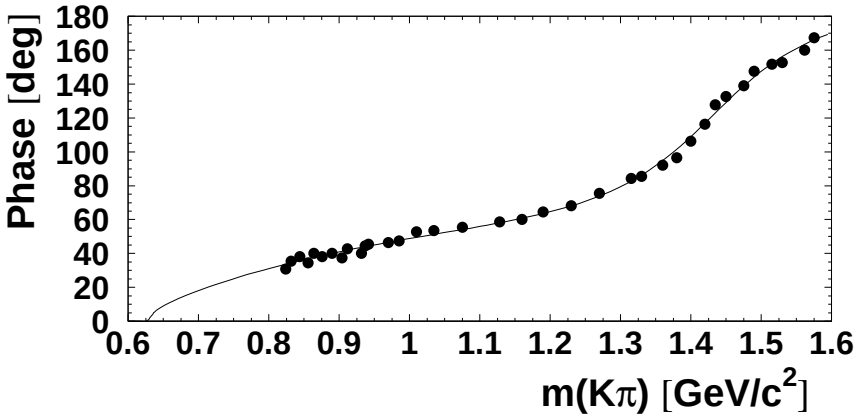

Figure 41: *Phase shift for the $K\pi$ scattering from ref. [57]. The curve shows the fit using the K-matrix formalism with one resonance and the effective range approximation.*

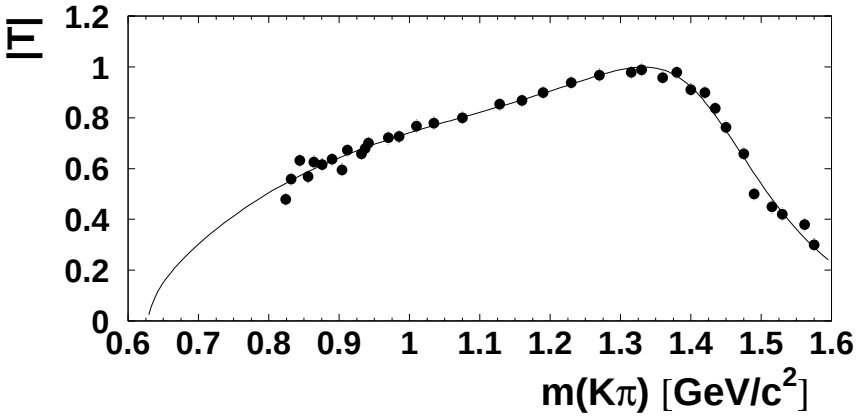

Figure 42: *The amplitude $|T|$ from [57] as a function of $K\pi$ invariant mass. The curve shows the fit.*

Parameter	Fit to the phase shift δ	Fit to the scattering amplitude $\|T\|$	Results from ref. [57]
m_0 [MeV/c^2]	1344 ± 4	1332 ± 5	
Γ_0 [MeV/c^2]	404 ± 22	401 ± 16	
m_R [MeV/c^2]	1432 ± 5	1414 ± 5	$1429 \pm 4 \pm 5$
Γ_R [MeV/c^2]	268 ± 15	286 ± 15	$287 \pm 10 \pm 21$
a [GeV/c^{-1}]	2.58 ± 0.21	2.46 ± 0.14	$2.02 \pm 0.86 \pm 0.30$
b [GeV/c^{-1}]	1.81 ± 0.25	2.16 ± 0.19	$0.65 \pm 0.32 \pm 0.34$
χ^2/N_{dof}	15.3/(36-4)=0.48	44.7/(36-4)=1.40	

Table 10: *Results of the fit to the $I = 1/2$ $(K\pi)_S$ wave scattering data from Aston et al. [57].*

from which it follows that

$$\hat{K} = \frac{am}{2 + abq^2}. \tag{111}$$

By adding the resonance term assuming elastic $K\pi$ scattering, one obtains the Lorentz invariant K-matrix

$$\hat{K} = \frac{am}{2 + abq^2} + \frac{m_0\Gamma_0/\rho_0}{m_0^2 - m^2}. \tag{112}$$

The scattering amplitude given by

$$T = \rho(1 - i\rho\hat{K})^{-1}\hat{K} = e^{i\delta}\sin\delta \tag{113}$$

was used to fit the phase shift δ or the scattering amplitude $|T|$ from the scattering data of ref. [57]. The K-matrix pole gives the position where the amplitude $|T|$ has its maximum (or, where the phase passes $\delta = \pi/2$).

The fit results are given in table 10. The resonance parameters m_R and Γ_R of $K^{*0}(1430)$ are obtained by replacing m^2 in eqn. 112 by the complex energy $s = (m_R + i\Gamma_R/2)^2$ and determining s for which $|T|^2 = \infty$. The resonance parameters from the fit to the phase shift and the fit to the scattering amplitude are slightly different. However, the average values for the mass and the width are in agreement with ref. [57]:

$$m_R = (1423 \pm 10)\,\mathrm{MeV}/c^2, \tag{114}$$

$$\Gamma_R = (277 \pm 17)\,\mathrm{MeV}/c^2. \tag{115}$$

The error includes both the sytematic and statistical error. The scattering length a is also compatible, while the effective range b is larger. Aston et al. [57] used a different parametrization for T (eqn. 113). In particular, they fitted also an offset phase δ_0 which, in the fit using the K-matrix formalism, introduces large correlations between δ_0 and the effective range b. However, in this case the effective range is then compatible with ref. [57].

The result of the fit to the phase shift was used to define the K-matrix for the dynamical function $\hat{F}$. The total transition amplitude for the $I = 1/2$ $(K\pi)_S$ wave is

$$\begin{aligned} A(\overline{p}p(^1S_0) \to (\pi^0 K_L)_S K_L) &= A'(0,00)A(0,00) \\ &= \hat{F}_{(K\pi)_S}. \end{aligned} \tag{116}$$

It is noted that the same symmetry properties with respect to the exchange of the K_L are valid for $\overline{p}p(^1S_0) \to (\pi^0 K_L)_S K_L$ as for $\overline{p}p(^1S_0) \to K^*(896)K$.

9.3.3 $\overline{p}p(^1S_0) \to \pi^0(K_L K_L)_S$

The possible contributions to the $(K\overline{K})_S$ wave are $a_0(980)$ and $a_0(1450)$ in the $I = 1$ channel and $f_0(980)$, $f_0(1370)$ and $f_0(1500)$ in the $I = 0$ channel. $a_0(980)$ and $f_0(980)$ definitively require a (2×2) K-matrix with couplings to the $K\overline{K}$, $\eta\pi$ and $\pi\pi$ channels, in order to describe the behaviour at the $K\overline{K}$ threshold. The other scalar resonances are far from threshold and therefore a (1×1) K-matrix was used. The transition amplitude is

$$\begin{aligned} A(\overline{p}p \to \pi^0(K_L K_L)^I_S) &= A'(0,00)A(0,00) \\ &= \hat{F}^I_{(K\overline{K})_S}, \end{aligned} \tag{117}$$

where I denotes the isospin of the $K\overline{K}$ system. The best fit to the $\pi^0 K_L K_L$ data will determine how many poles are finally needed.

9.3.4 $\overline{p}p(^1S_0) \to \pi^0(K_L K_L)_D$

Possible contributions to the $(K_L K_L)_D$ wave are $a_2(1320)$, $f_2(1270)$ and $f_2'(1525)$. Since $a_2(1320)$ is $I = 1$ while $f_2(1270)$ and $f_2'(1525)$ are $I = 0$ and $f_2(1270)$ and

$f_2'(1525)$ are well separated in mass, relativistic Breit-Wigner functions were used for the dynamical functions for all three tensor resonances. Thus the transition amplitudes are

$$\begin{aligned} A(\overline{p}p \to \pi^0(K_L K_L)_D) &= A'(2,20)A(0,22) \\ &= \frac{1}{2\sqrt{5}}(3\cos^2\theta - 1)B_2(Q)B_2(q)\frac{m_0\Gamma_0/\rho_0}{m_0^2 - m^2 - im_0\Gamma(m)}. \end{aligned} \tag{118}$$

9.4 Fit Procedure

The $\pi^0 K_L K_L$ Dalitz plot was fitted using the χ^2 minimization method based on the MINUIT [60] program package. The χ^2 function was defined by

$$\chi^2 = \sum_i \frac{(W_i - N_i^0)^2}{\sigma_i^2}, \tag{119}$$

where the sum extends over all bins in the $\pi^0 K_L K_L$ Dalitz plot. N_i^0 is the experimental number of events of each bin after background subtraction and acceptance correction:

$$N_i^0 = (N_i - n_i)\, c_i, \tag{120}$$

where N_i is the number of $\pi^0 K_L K_L$ events from the π^0 main window, n_i is the number of events from the π^0 side-bins (background) and c_i is the accpetance correction function given in section 8.1. The error σ_i is given by

$$\sigma_i^2 = (N_i + n_i)\, c_i^2. \tag{121}$$

The bin size of (0.045×0.045) $(\mathrm{GeV}^2/\mathrm{c}^4)^2$ is about twice the experimental resolution (≈ 0.020 GeV^2/c^4). Hence, each bin was divided into 4 sub-bins for which the transition probability was calculated at the center of each sub-bin. The spacing between these points is 0.0225 GeV^2/c^4. It could be shown that increasing the number of sub-bins does not change the fit results. The theoretical weight in bin i is then given by the average transition probability of the 4 sub-bins:

$$W_i = \frac{1}{4}\sum_{j=1}^{4}\sum_{l=1}^{n} |\alpha_l A_{lij}|^2, \tag{122}$$

where l runs over all decay chains.

The transition amplitudes A_{lj} were normalized to the data such that $|\alpha_l|^2$ give the relative contributions of the partial wave in $\pi^0 K_L K_L$ [8]. For each partial wave it is required that

$$f_l \sum_{j=1}^{4\times N_{\rm bins}} |A_{lj}|^2 = \sum_{i=1}^{N_{\rm bins}} N_i^0 = N^0 \tag{123}$$

where $N_{\rm bins}$ is the number of bins in the Dalitz plot, f_l is the normalization factor for the partial wave l and N^0 is the total number of background subtracted events in the acceptance corrected Dalitz plot $\pi^0 K_L K_L$. The normalization is given by

$$A_{lj} \rightarrow \sqrt{f_l} A_{lj} = \sqrt{\frac{N^0}{\sum_{j=1}^{4\times N_{\rm bins}} |A_{lj}|^2}} A_{lj}. \tag{124}$$

Since masses and widths were varied during the fit, the transition amplitudes had to be normalized after each iteration.

The $\pi^0 K_L K_L$ Dalitz plot has <u>not</u> been symmetrized with respect to the two K_L due to their different systematics in the detection and reconstruction. The depletion around the maximum decay angle $\theta_{\rm max}$ of the interacting K_L is a particular example (see section 6.2.2). The transition amplitudes of $\pi^0 K_L K_L$ require a symmetric Dalitz plot and therefore a χ^2 test of pairs of symmetric bins was performed. Only pairs of bins with number of entries N_i^0 and N_j^0 for which

$$\chi^2 = \frac{(N_i^0 - N_j^0)^2}{\sigma_i^2 + \sigma_j^2} < 9 \tag{125}$$

were considered in the fit to the $\pi^0 K_L K_L$ data. In addition, bins at the boundary of the $\pi^0 K_L K_L$ Dalitz plot were rejected.

The mask of the 788 bins bins which had been accepted is shown in figure 43. The Dalitz plot in figure 44 was used for the partial wave analysis of $\overline{p}p \rightarrow \pi^0 K_L K_L$.

[8] If the decay chain l was the only one that contributes to $\pi^0 K_L K_L$, then $|\alpha_l|^2 = 1$ and hence the branching ratio B_l would be $B_l = B(\overline{p}p \rightarrow \pi^0 K_L K_L)$.

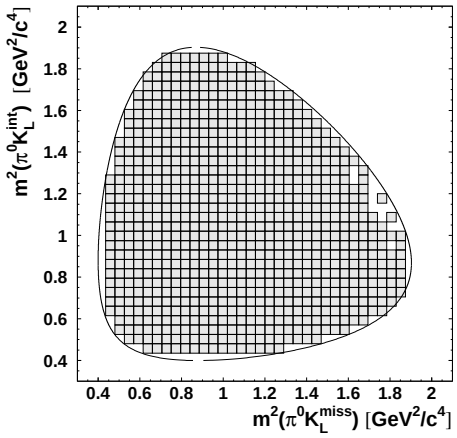

Figure 43: *Mask of accepted bins.*

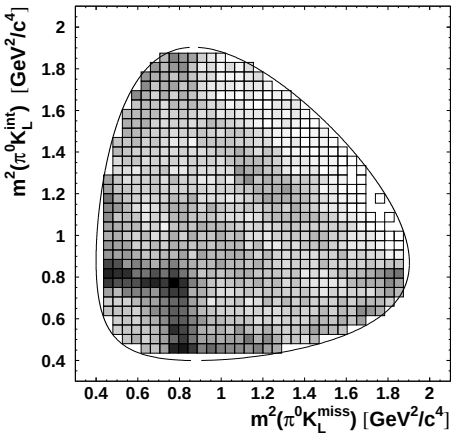

Figure 44: *Data Dalitz plot of $\pi^0 K_L K_L$ which was used for the χ^2 fit*

9.5 Fit Results

9.5.1 The Minimum Hypothesis

The minimum hypothesis includes resonances which are known to decay into $K\pi$ or $K\overline{K}$ (except $a_0(980)$ and $f_0(980)$) and which are obviously observed in figure 44.

The accumulation of events in the crossing region of the two K^* bands suggests constructive interference between the two K^*K amplitudes, hence $G = +1$. Thus K^*K production from the $I = 0$ $^1S_0$ $\overline{p}p$ initial state was assumed and hence the relative phase between the two amplitudes was fixed to $\delta\phi = 0$. The measured width of $K^{*0}(892)$ is a convolution of the natural width of 50 MeV/c^2 and the experimental resolution. Hence, it was decided to fit the width. Also the mass was fitted in order to check the behaviour of the fit.

For these fits, the relative phase between the amplitudes for the $K\pi$ S-wave was also fixed to $\delta\phi_{(K\pi)_S} = 0$ although the $(K\pi)$ S-wave is not directly seen in the data which would allow to conclude on the self-interference.

Both the $f_2(1270)$ and the $a_2(1320)$ were included in the minimum hypothesis to describe the enhancement around 1300 MeV/c^2 albeit with fixed masses and

widths according to the PDG [29] since otherwise correlations occur due to strong overlap of the two states.

To account for the enhancements at the border of the $\pi^0 K_L K_L$ Dalitz plot around a $K\overline{K}$ mass of 1520 MeV/c^2, an additional tensor resonance was included. As start values for the mass and the width, the resonance parameters of the $f_2'(1525)$ [29] were taken ($m = 1525$ MeV/c^2 and $\Gamma = 76$ MeV/c^2).

The $K\overline{K}$ S-wave was parametrized by a (1×1) K-matrix with one pole hence a Breit-Wigner amplitude. The aim was to describe the intensity at the center of the $\pi^0 K_L K_L$ Dalitz plot which corresponds to a $K\overline{K}$ mass of about 1450 MeV/c^2. Both isospins $I = 0$ and $I = 1$ for the $K\overline{K}$ S-wave are possible.

One phase of the complex coefficients $\alpha = |\alpha|\, e^{i\phi}$ (eqn. 87) is arbitrary and can be set to $\phi = 0$. This was done for the $K^{*0}(896)K$ amplitude. Thus for the minimum hypothesis 17 parameters had to be determined by the fit: 6 coefficients $|\alpha|$, 5 phases ϕ, 3 masses and 3 widths for $K^{*0}(896)$, $f_2'(1525)$ and the resonance around 1400 MeV/c^2. The symmetric amplitudes for K^*K and KK^* were described by same amplitude $|\alpha|$.

The fit converged to a χ^2 per degree of freedom of $\chi^2/N_{\mathrm{dof}} = 1255/(788-17) = 1.63$. The fitted parameters are given in table 11 (fit A). The resulting Dalitz plot $\pi^0 K_L K_L$ is shown in figure 45. Figure 46 shows the χ^2 per bin. Large deviations between fit and data are observed in the region around a $K\overline{K}$ mass of 1500 MeV/c^2, indicated by the line, and at low $K\overline{K}$ masses. This descrepancy is very striking in the invariant mass squared spectrum of $K\overline{K}$ (figure 47) where the minimum hypothesis failed completely to describe the dip around $m = 1500$ MeV/c^2.

The mass of the $K^{*0}(896)$ is also somewhat too high (table 11). The larger width of 78 MeV/c^2 compared to the PDG value of 51 MeV/c^2 suggests that the $K^{*0}(896)K$ amplitudes tried to compensate for missing information.

The $K\pi$ S-wave is significant. Due to the constructive self-interference of the two symmetric amplitudes $(K\pi)_S K'$ and $(K'\pi)_S K$, the $K\pi$ S-wave contributes not only to low $K\overline{K}$ masses but also to any region of the $\pi^0 K_L K_L$ Dalitz plot (see section 9.6).

The resonance parameters of the high mass tensor were consistent with $f_2'(1525)$ for which the PDG gives mass and width 1525 ± 5 MeV/c^2 and 76 ± 10 MeV/c^2, respectively. Thus this state was identified with $f_2'(1525)$. Due to the decay angular distribution, $f_2'(1525)$ manifests itself significantly only at the border of the $\pi^0 K_L K_L$ Dalitz plot.

The $(K\overline{K})_S$ wave contributes about $|\alpha_{(K\overline{K})_S}|^2 \approx 80\%$ to the $\pi^0 K_L K_L$ Dalitz plot. Note that the number of produced events per $\overline{p}$ in a given channel i is $|\alpha_i|^2 \times B(\overline{p}p \to \pi^0 K_L K_L)$ which is not necessarily the number of observed events due to interference effects. Therefore in general $\sum_i |\alpha_i|^2 \neq 1$. With a mass of 1318 MeV/c^2 and a width of 317 MeV/c^2, this state could not be identified with any known scalar resonance auch as $f_0(1370)$ or $a_0(1450)$ and in fact, the $K\overline{K}$ description was poor (fig. 47).

Intermediate state	$\|\alpha\|$	Phase ϕ [rad]	Mass [MeV/c^2]	Width [MeV/c^2]
$K^{*0}(896)K^0$	0.261 ± 0.005	0.	903 ± 2	78 ± 2
$K_0^{*0}(1430)K^0$	0.267 ± 0.006	1.25 ± 0.03	$K\pi$ S-wave	
$f_2(1275)\pi^0$	0.391 ± 0.016	1.85 ± 0.08	1275	185
$a_2^0(1320)\pi^0$	0.390 ± 0.017	4.95 ± 0.06	1320	105
$f_2'(1525)\pi^0$	0.138 ± 0.010	5.51 ± 0.09	1523 ± 5	84 ± 8
$(K\overline{K})_S^a\pi^0$	0.904 ± 0.011	4.78 ± 0.04	1318 ± 12	317 ± 4
$\chi^2/N_{dof} = 1255/(788-17) = 1.63$				

Table 11: *Fit A: Results for the minimum hypothesis.*

9.5.2 Two Scalar Resonances in $K\overline{K}$

The bad description at $K\overline{K}$ masses around 1500 MeV/c^2 required an extension of the minimum hypothesis by adding an additional scalar $K\overline{K}$ resonance.

Since in this case both resonances have $J^{PC} = 0^{++}$ the only quantum number which distinguishes them is isospin but which cannot be determined from the $\pi^0 K_L K_L$ data alone.

The two possibilities for different or equal isospins were tested for which the the $(K\overline{K})_S$ wave was parametrized as follows:

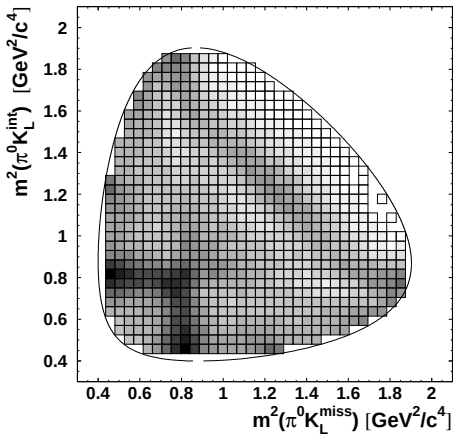

Figure 45: *Fit A: $\pi^0 K_L K_L$ Dalitz plot showing the fit with the minimum hypothesis.*

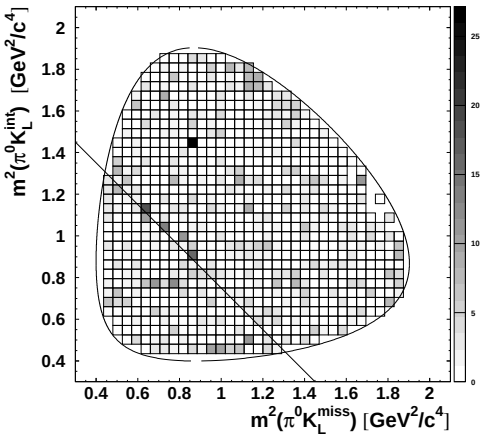

Figure 46: *Fit A: Distribution of χ^2 per bin. The badly described region around $m(K_L K_L) = 1500\ MeV/c^2$ is indicated by the line. Also the region at low $K\overline{K}$ masses contributes significantly to the total χ^2.*

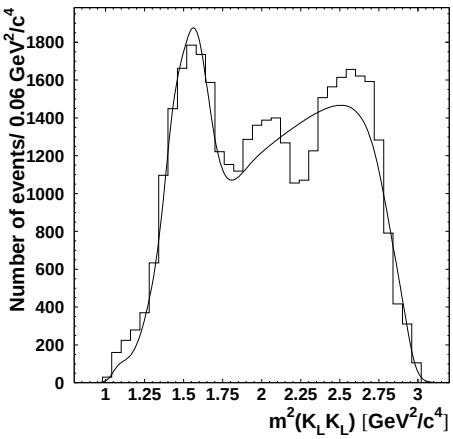

Figure 47: *Fit A: Invariant mass $m^2(K_L K_L)$. The data is shown as histogram. The curve is the fit.*

For two resonances of different isospins, the (1×1) K-matrices are given by

$$\hat{K}_1(I=0) = \frac{m_1\Gamma_1/\rho_1^0}{m_1^2 - m^2} \tag{126}$$

and

$$\hat{K}_2(I=1) = \frac{m_2\Gamma_2/\rho_2^0}{m_2^2 - m^2}. \tag{127}$$

The total transition amplitude $A_{(K\overline{K})_S}$ of the $(K\overline{K})_S$ wave is then the coherent sum of two Breit-Wigner amplitudes for each isospin state:

$$\begin{aligned} A_{\rm tot}(\overline{p}p \to \pi^0(K\overline{K})_S &= \alpha_1 A(\overline{p}p \to \pi^0(K\overline{K})_S^{I=0}) + \\ &\quad \alpha_2 A(\overline{p}p \to \pi^0(K\overline{K})_S^{I=1}) \qquad (128) \\ &= \alpha_1 \hat{F}_1^{I=0} + \alpha_2 \hat{F}_2^{I=1} \\ &= \alpha_1 \frac{m_1\Gamma_1/\rho_1^0}{m_1^2 - m^2 - i m_1\Gamma_1(m)} + \\ &\quad \alpha_2 \frac{m_2\Gamma_2/\rho_2^0}{m_2^2 - m^2 - i m_2\Gamma_2(m)}, \qquad (129) \end{aligned}$$

where the production amplitudes β are absorbed in the complex coefficients α.

If the two resonances have the same isospin I then the K-matrix is

$$\hat{K} = \frac{m_1\Gamma_1/\rho_1^0}{m_1^2 - m^2} + \frac{m_2\Gamma_2/\rho_2^0}{m_2^2 - m^2}. \tag{130}$$

With the overlap terms

$$\Delta_{12} = \frac{m_1^2 - m^2}{m_2^2 - m^2}\,\frac{m_2\Gamma_2}{\rho_2^0} \quad \text{and} \quad \Delta_{21} = \frac{m_2^2 - m^2}{m_1^2 - m^2}\,\frac{m_1\Gamma_1}{\rho_1^0},$$

the total transition amplitude of the $(K\overline{K})_S$ wave becomes

$$\begin{aligned} A_{\rm tot}(\overline{p}p \to \pi^0(K\overline{K})_S^I) &= \alpha A(\overline{p}p \to \pi^0(K\overline{K})_S^I) \\ &= \alpha \hat{F}^I \\ &= \alpha \begin{pmatrix} \frac{m_1\Gamma_1/\rho_1^0}{m_1^2 - m^2 - i\rho(m_1\Gamma_1/\rho_1^0 + \Delta_{12})} + \\ \\ \beta_r \frac{m_2\Gamma_2/\rho_2^0}{m_2^2 - m^2 - i\rho(m_2\Gamma_2/\rho_2^0 + \Delta_{21})} \end{pmatrix}, \qquad (131) \end{aligned}$$

where $\beta_r = |\beta_r| e^{i\delta_r}$ is the relative (complex) production amplitude between the two states and α gives the production amplitude of the complete $K\overline{K}$ S-wave.

First, the results of the fit assuming two scalar $K\overline{K}$ resonances of different isospin are discussed (fit B). The total χ^2 decreased by 244 to 1011 giving a χ^2 per degree of freedom of $\chi^2/N_{\rm dof} = 1011/(788-21) = 1.32$. The dip at 1500 MeV/$c^2$ in the $K\overline{K}$ squared invariant mass spectrum could be perfectly described (fig. 50). This improvement is also seen in the $\pi^0 K_L K_L$ Dalitz plot showing the χ^2 per bin (figure 49).

As a result, the resonance parameters of $K^*(896)$ also became compatible with the PDG values: The mass of 899 ± 2 MeV/c^2 agrees perfectly while the width of 67 ± 3 MeV/c^2 is still somewhat too large due to experimental resolution. Assuming that the squared Breit-Wigner amplitude is approximated by a Gaussian, its FWHM is given by $\Gamma_0 = \sigma_0 \, 2\sqrt{2ln2}$. The measured width is then approximately $\Gamma_{\rm mes} = 2\sqrt{2ln2}\sqrt{\sigma_r^2 + \sigma_0^2}$ where $\sigma_0 = 21.4$ MeV/c^2 for $\Gamma_0 = 50.5$MeV/c^2. Hence, the measured width is consistent with a resolution of $\sigma_r \approx 20$ MeV/c^2, which is resonable (see $p.$ 27). Note that the spacing of the points at which the transition amplitudes were calculated is about 12 MeV/c^2 at the K^{*0} mass.

The width of $f_2'(1525)$ increased by 10 MeV/c^2 but was still in good agreement with the PDG value. The production amplitude α_{f_2} did not change significantly.

The masses and widths of the two scalar $K\overline{K}$ resonances were

- $X_0(1)$: $m = (1409 \pm 9)$ MeV/c^2, $\Gamma = 337 \pm 12$ MeV/c^2,
- $X_0(2)$: $m = (1517 \pm 7)$ MeV/c^2, $\Gamma = 97 \pm 10$ MeV/c^2.

The parameters for the low mass resonance suggested the identification with the $f_0(1370)$ and the values for the high mass object were in perfect agreement with those of $f_0(1500)$. However, these two states are $I = 0$, in contradiction to the hypothesis of two resonances of different isospin. The identification of the low mass state with the $I = 1$ $a_0(1450)$ ($m = 1470$ MeV/c^2, $\Gamma = 265$ MeV/c^2) [43] is possible but unlikely since both fitted mass and the width are quite different. The fit results are summarized in table 12.

The two resonances were then described within the same K-matrix (eqn. 130), thus assuming equal isospin (fit C). The fit converged to the same $\chi^2/N_{\rm dof}$ of $1010/(788-21) = 1.32$. All parameters except those which belong to the $(K\overline{K})_S$

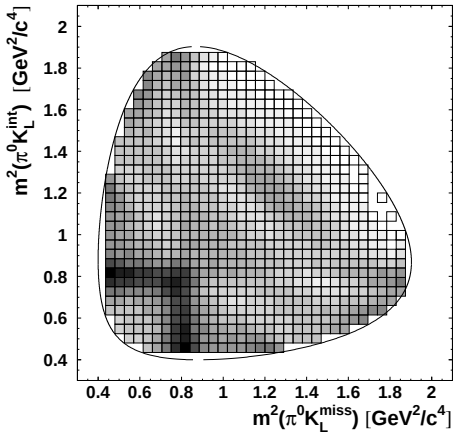

Figure 48: *Fit B,C: $\pi^0 K_L K_L$ Dalitz plot showing the fit with two scalar resonances.*

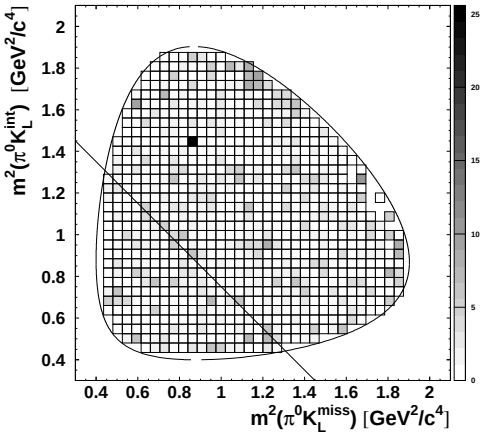

Figure 49: *Fit B,C: χ^2 per bin.*

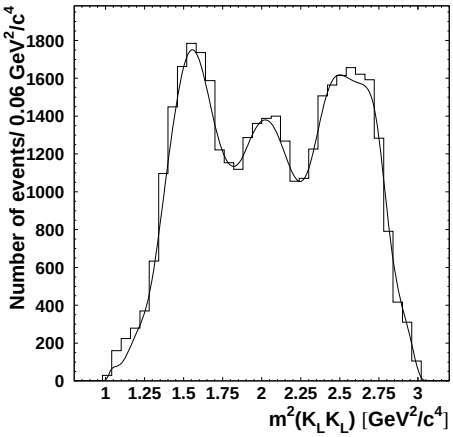

Figure 50: *Fit B,C: Invariant mass $m^2(K_L K_L)$. The data is given as histogram. The curve shows the fit.*

Intermediate state	$\|\alpha\|$	Phase ϕ [rad]	Mass [MeV/c^2]	Width [MeV/c^2]
$K^{*0}(896)K^0$	0.242 ± 0.007	0.	899 ± 2	67 ± 3
$K_0^{*0}(1430)K^0$	0.178 ± 0.007	1.24 ± 0.09	$K\pi$ S-wave	
$f_2(1275)\pi^0$	0.241 ± 0.021	2.11 ± 0.08	1275	185
$a_2^0(1320)\pi^0$	0.293 ± 0.015	4.71 ± 0.10	1320	105
$f_2'(1525)\pi^0$	0.149 ± 0.011	5.20 ± 0.12	1526 ± 5	99 ± 11
$(K\overline{K})_S^a\pi^0$	0.956 ± 0.038	5.42 ± 0.05	1409 ± 9	337 ± 12
$(K\overline{K})_S^b\pi$	0.219 ± 0.025	3.66 ± 0.23	1517 ± 7	97 ± 10
$\chi^2/N_{dof} = 1011/(788-21) = 1.32$				

Table 12: *Fit B: Results for the hypothesis of two scalar states having different (but unknown) isospins. The superscripts a and b for the $(K\overline{K})_S$ wave denote the different isospin states.*

wave remained within errors, which shows that the intensity distribution of the $(K\overline{K})$ wave could be equally good described in two ways. The K-matrix poles of 1361 ± 6 MeV/c^2 and 1571 ± 5 MeV/c^2 give the positions where the intensity of the $(K\overline{K})_S$ wave reaches its maxima and the K-matrix width give an idea of how broad these distributions are. The resonance parameters given by the complex poles of T-matrix in the complex energy plane were:

- $X_0(1)$: $m = (1404 \pm 10)$ MeV/c^2, $\Gamma = (342 \pm 25)$ MeV/c^2,
- $X_0(2)$: $m = (1517 \pm 12)$ MeV/c^2, $\Gamma = (96 \pm 12)$ MeV/c^2.

The errors were obtained by varying the K-matrix parameters within the errors from the fit. These resonance parameters are consistent with those found under the assumption of different isospin. Table 13 summarizes the fit results.

The χ^2 was the same for both hypotheses and hence it could not be decided whether the two states have the same isospin or not. It was found that the contributions of all other partial waves were independent of the assumptions made on the $(K\overline{K})_S$ wave and hence, the total contribution of the $(K\overline{K})_S$ is the same. Due to the good agreement of the resonance parameters with $f_0(1370)$ and $f_0(1500)$ the 2-pole K-matrix parametrization of the $(K\overline{K})_S$ wave was adopted for the following tests concerning correlations between the partial waves. Possible contributions of $a_0(1450)$ are discussed later (section 9.5.5).

Intermediate state	$\|\alpha\|$	Phase ϕ [rad]	Mass [MeV/c^2]	Width [MeV/c^2]
$K^{*0}(896)K^0$	0.241 ± 0.006	0.	899 ± 2	67 ± 3
$K_0^{*0}(1430)K^0$	0.175 ± 0.008	1.21 ± 0.08	$K\pi$ S-wave	
$f_2(1275)\pi^0$	0.238 ± 0.016	2.10 ± 0.09	1275	185
$a_2^0(1320)\pi^0$	0.291 ± 0.016	4.78 ± 0.12	1320	105
$f_2'(1525)\pi^0$	0.149 ± 0.011	5.19 ± 0.10	1527 ± 5	99 ± 11
$(K\overline{K})_S\pi^0$	0.842 ± 0.020	5.08 ± 0.04	K-matrix pole 1:	
			1361 ± 6	264 ± 10
			K-matrix pole 2:	
	$\|\beta_r\| = 0.895 \pm 0.014$	$\delta_r = 0.71 \pm 0.04$	1571 ± 5	162 ± 6
$\chi^2/N_{dof} = 1010/(788-21) = 1.32$				

Table 13: *Fit C: Results for the hypothesis of two scalar states having the same isospin.*

9.5.3 $a_2 - f_2$ Interference

Five $K\overline{K}$ resonances are needed to obtain a good fit to the data: three tensor states, $a_2(1320)$, $f_2(1275)$ and $f_2'(1525)$ and two scalars. The mass and width of $a_2(1320)$ and $f_2(1275)$ are very similar and thus interference between these two states is important. It was tested to what extent the fit was able to find the correct description of $a_2 - f_2$ interference by fixing the $a_2(1320)$ contributions $|\alpha_{a_2}|^2$ to 5, 15 and 30% (fit D1, D2 and D3, respectively) and fitting all other parameters as for fit C. The results are listed in tables 14 and 15.

While the phase of $f_2(1275)$ only slightly depends on the a_2 contribution a strong correlation is observed for the amplitude $|\alpha_{f_2}|$. The relative phase between a_2 and f_2 is $\Delta\phi_{a_2,f_2} = 2.68$ for fit C and close to π for fit D3 which suggests that destructive interference is responsible for the compensation of the $a_2(1320)$ contribution. The χ^2 as a function of a_2 contributions is shown in figure 51. Fit C gives indeed the best χ^2.

A dramatic influence is observed on the mass and width of $f_2'(1525)$. At 30% a_2 contribution, the mass decreases from 1527 MeV/c^2 to 1446 MeV/c^2 while the width increases from 99 MeV/c^2 to 202 MeV/c^2.

Intermediate	Fit C		Fit D1	
state	$\|\alpha\|$	ϕ	$\|\alpha\|$	ϕ
$\pi^0 a_2^0(1320)$	0.291(16)	4.78(9)	$\|\alpha\|^2 = 5\%$	4.53(10)
$K^{*0}K^0$	0.241(6)	0	0.234(6)	0
$(K\pi^0)_S K$	0.175(8)	1.21(8)	0.168(8)	1.13(4)
$\pi^0 f_2(1275)$	0.238(16)	2.10(9)	0.207(15)	2.27(9)
$\pi^0 f_2'(1525)$	0.149(11)	5.19(10)	0.150(11)	5.24(10)
$\pi^0(K\overline{K})_S$	0.842(20)	5.08(4)	0.841(9)	5.03(4)
$\|\beta_r\|, \delta_r$	0.895(14)	0.71(4)	0.922(23)	0.71(5)
$\chi^2/N_{\rm dof}$	1010/767=1.32		1028/768 = 1.34	
Intermediate	Fit D2		Fit D3	
state	$\|\alpha\|$	ϕ	$\|\alpha\|$	ϕ
$\pi^0 a_2^0(1320)$	$\|\alpha\|^2 = 15\%$	4.95(6)	$\|\alpha\|^2 = 30\%$	5.20(7)
$K^{*0}K^0$	0.248(5)	0	0.255(8)	0
$(K\pi^0)_S K$	0.216(11)	1.44(4)	0.200(8)	1.01(6)
$\pi^0 f_2(1275)$	0.357(15)	1.94(6)	0.351(21)	1.74(8)
$\pi^0 f_2'(1525)$	0.149(10)	5.30(8)	0.328(25)	4.35(9)
$\pi^0(K\overline{K})_S$	0.898(17)	5.02(5)	0.736(17)	5.21(4)
$\|\beta_r\|, \delta_r$	0.814(10)	0.73(1)	0.932(24)	0.74(3)
$\chi^2/N_{\rm dof}$	1036/768=1.35		1236/768=1.61	

Table 14: *Scan of* $a_2^0(1320)$ *contributions: Amplitudes* $|\alpha|$ *and phases* ϕ*, with* $|alpha_{a_2}|^2$ *kept constant in fits D1-D3.*

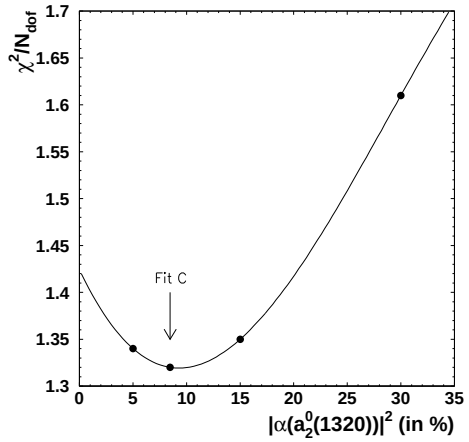

Figure 51: $\chi^2/N_{\rm dof}$ *as a function of* $|\alpha(a_2^0(1320))|^2$.

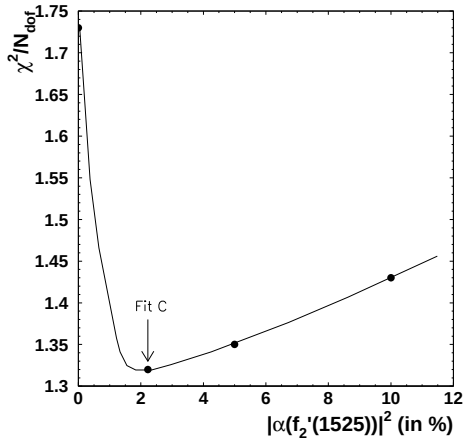

Figure 52: $\chi^2/N_{\rm dof}$ *as a function of* $|\alpha(f_2'(1525))|^2$.

Resonance	Fit C		Fit D1	
	m [MeV/c^2]	Γ [MeV/c^2]	m [MeV/c^2]	Γ [MeV/c^2]
$K^{*0}(896)$	899(2)	67(3)	901(2)	67(3)
$f_2'(1525)$	1527(5)	99(11)	1535(5)	106(12)
$(K\overline{K})_S$	1361(6)	264(10)	1369(6)	258(11)
(K-matrix parameters)	1571(5)	163(6)	1574(7)	165(12)
$(K\overline{K})_S$	1404	342	1415	332
(T-matrix poles)	1517	96	1519	100
Resonance	Fit D2		Fit D3	
	m [MeV/c^2]	Γ [MeV/c^2]	m [MeV/c^2]	Γ [MeV/c^2]
$K^{*0}(896)$	899(1)	68(3)	894(2)	64(3)
$f_2'(1525)$	1522(5)	95(9)	1446(8)	202(17)
$(K\overline{K})_S$	1336(4)	282(6)	1352(4)	275(9)
(K-matrix parameters)	1559(5)	143(15)	1579(6)	152(12)
$(K\overline{K})_S$	1363	356	1384	342
(T-matrix poles)	1512	90	1527	100

Table 15: *Scan of* $a_2^0(1320)$ *contributions: Masses and widths.*

9.5.4 Scan of f_2' Contribution

The high mass K-matrix pole of the $(K\overline{K})_S$ wave was found at 1571 MeV/c^2 (table 13) which is close to the Breit-Wigner pole of $f_2'(1525)$. The correlation between scalar and tensor intensities in this mass region was investigated by fixing the $f_2'(1525)$ contributions $|\alpha_{f_2'}|^2$ to 0% (fit E1), 5% (fit E2) and 10% (fit E3). Note that the fitted contribution is $|\alpha_{f_2'}|^2 = 2.2\%$ (fit C). The results are summarized in tables 16 and 17. The minimum χ^2 is found for fit C (fig. 52).

A tensor resonance around 1525 MeV/c^2 is obviously required otherwise a bad χ^2 of 1.73 is found (fit E1). While the mass of f_2' remains rather stable the width increases steadily from 99 MeV/c^2 (Fit C) to 264 MeV/c^2 for $|\alpha_{f_2'}|^2 = 10\%$. As a consequence the overall contribution of the $(K\overline{K})_S$ wave is reduced.

9.5.5 Scan of $a_0(1450)$ Contribution

The fit was able to describe the $a_2 - f_2$ interference and the contributions from scalar and tensor resonances at high $K\overline{K}$ masses without ambiguities since al-

Intermediate	Fit C		Fit E1	
state	$\lvert\alpha\rvert$	ϕ	$\lvert\alpha\rvert$	ϕ
$\pi^0 f_2'(1525)$	0.149(11)	5.19(10)	$\lvert\alpha\rvert^2 = 0\%$	-
$K^{*0}K^0$	0.241(6)	0	0.204(5)	0
$(K\pi^0)_S K$	0.175(8)	1.21(8)	0.200(6)	1.48(5)
$\pi^0 f_2(1275)$	0.238(16)	2.10(9)	0.191(14)	2.23(12)
$\pi^0 a_2^0(1320)$	0.291(16)	4.78(9)	0.272(15)	4.45(8)
$\pi^0(K\overline{K})_S$	0.842(20)	5.08(4)	0.936(12)	5.00(4)
$\lvert\beta_r\rvert, \delta_r$	0.895(14)	0.71(4)	0.885(11)	0.84(2)
$\chi^2/N_{\rm dof}$	1010/767=1.32		1331/771 = 1.73	
Intermediate	Fit E2		Fit E3	
state	$\lvert\alpha\rvert$	ϕ	$\lvert\alpha\rvert$	ϕ
$\pi^0 f_2'(1525)$	$\lvert\alpha\rvert^2 = 5\%$	4.99(9)	$\lvert\alpha\rvert^2 = 10\%$	4.89(9)
$K^{*0}K^0$	0.244(7)	0	0.237(5)	0
$(K\pi^0)_S K$	0.177(8)	0.97(7)	0.195(5)	0.85(4)
$\pi^0 f_2(1275)$	0.249(21)	2.10(8)	0.290(18)	2.08(9)
$\pi^0 a_2^0(1320)$	0.298(17)	4.89(8)	0.317(17)	5.17(8)
$\pi^0(K\overline{K})_S$	0.780(18)	5.10(4)	0.745(10)	5.08(4)
$\lvert\beta_r\rvert, \delta_r$	0.948(22)	0.72(5)	1.004(16)	0.73(2)
$\chi^2/N_{\rm dof}$	1035/768=1.35		1096/768 = 1.43	

Table 16: *Scan of* $f_2'(1525)$ *contributions: Amplitudes* $|\alpha|$ *and phases* ϕ.

Resonance	Fit C		Fit E1	
	m	Γ	m	Γ
	[MeV/c^2]	[MeV/c^2]	[MeV/c^2]	[MeV/c^2]
$K^{*0}(896)$	899(2)	67(3)	899(1)	62(2)
$f_2'(1525)$	1527(5)	99(11)	-	-
$(K\overline{K})_S$	1361(6)	264(10)	1350(3)	273(6)
(K-matrix parameters)	1571(5)	163(6)	1592(3)	171(8)
$(K\overline{K})_S$	1404	342	1389	342
(T-matrix poles)	1517	96	1539	117
Resonance	Fit E2		Fit E3	
	m	Γ	m	Γ
	[MeV/c^2]	[MeV/c^2]	[MeV/c^2]	[MeV/c^2]
$K^{*0}(896)$	898(2)	66(3)	897(1)	62(2)
$f_2'(1525)$	1528(7)	163(11)	1538(9)	264(15)
$(K\overline{K})_S$	1365(5)	263(10)	1363(4)	274(8)
(K-matrix parameters)	1578(6)	160(13)	1585(3)	160(13)
$(K\overline{K})_S$	1407	336	1402	334
(T-matrix poles)	1528	100	1528	108

Table 17: *Scan of* $f_2'(1525)$ *contributions: Masses and widths.*

ways a clear minimum for the χ^2 function was found. In the following it is discussed how interferences between nearby scalar resonances affect the results. The parametrization of two scalar resonances in the same K-matrix, i.e. two scalar resonances of the same isospin I, was motivated by the similarity of the resonance parameters to $f_0(1370)$ and $f_0(1500)$. However, an admixture of an isovector resonance such as $a_0(1450)$ cannot be excluded.

The $a_0(1450)$ decaying into $\pi^0\eta$ was discovered in the reaction $\overline{p}p \to \pi^0\pi^0\eta$ [43]. The branching ratio for $a_0^0(1450) \to K\overline{K}$, including all charge configurations of the $K\overline{K}$ system, can be calculated using SU(3) couplings for an $I = 1$ quarkonium state [25]:

$$\frac{B(a_0^0 \to K\overline{K})}{B(a_0^0 \to \pi^0\eta)} = \frac{\rho^2}{2\cos^2\phi}\,\frac{q_{K\overline{K}}}{q_{\pi^0\eta}}, \tag{132}$$

where ρ is the flavour symmetry factor describing the relative coupling strength of an $n\overline{n} \equiv 1/\sqrt{2}(u\overline{u} + d\overline{d})$ or an $s\overline{s}$ pair to the vacuum and $\phi = 54.7^\circ + \theta_{PS}$. With $\rho = 1$ and the pseudoscalar mixing angle $\theta_{PS} = -17.3^\circ$ [58] one obtains for

a mass of 1470 MeV/c^2 [43]

$$\frac{B(a_0^0 \to K\overline{K})}{B(a_0^0 \to \pi^0\eta)} \quad = \quad 0.69. \tag{133}$$

The contribution $|\alpha_{a_0(1450)}|^2$ of $a_0(1450)$ in $\pi^0 K_L K_L$ can be deduced using $B(\overline{p}p \to \pi^0 a_0(1450), a_0(1450) \to \pi^0\eta) = (3.35 \pm 0.90) \times 10^{-4}$ [43] and $B(\overline{p}p \to \pi^0 K_L K_L) = B(\overline{p}p \to \pi^0 K_S K_S) = (7.5 \pm 0.3) \times 10^{-4}$ [30][32]:

$$\begin{aligned} |\alpha_{a_0(1450)}|^2 &= \frac{1}{4}\frac{B(a_0^0 \to K\overline{K})}{B(a_0^0 \to \pi^0\eta)}\frac{B(\overline{p}p \to \pi^0 a_0(1450), a_0(1450) \to \pi^0\eta)}{B(\overline{p}p \to \pi^0 K_L K_L)} \\ &= (7.7 \pm 2.1) \times 10^{-2}. \end{aligned} \tag{134}$$

The $\pi^0 K_L K_L$ Dalitz plot was fitted with $a_0(1450)$ contributions of 5% (fit F1), 10% (fit F1) and 15% (fit F3). Note that fit C assumes no $a_0(1450)$. A relativistic Breit-Wigner amplitude was used for $a_0(1450)$ with fixed mass and width of 1470 MeV/c^2 and 265 MeV/c^2, respectively (from solution A in [43]). The results are given in tables 18 and 19.

The most remarkable result is that the χ^2 is the same for all hypotheses which shows that the $(K\overline{K})_S$ wave can be equally well described with two or three scalar resonances. Hence, a fit with a free $a_0(1450)$ contribution does not work since the parameters determining the $(K\overline{K})_S$ wave are highly correlated.

It is important to note that all parameters except those of the $(K\overline{K})_S$ wave remain within errors. In particular, it is found that

$$|\sum_i \alpha_i|^2 \quad = \quad \text{constant for i} \neq (\mathrm{K\overline{K}})_{\mathrm{S}}^{\mathrm{I=0}}, \mathrm{a_0(1450)}, \tag{135}$$

i.e. independent of the $a_0(1450)$ contribution. On the other hand, the coherent sum of the different isospin contributions within the $(K\overline{K})_S$ wave is also constant and independent of the $a_0(1450) = (K\overline{K})_S^{I=1}$ contribution:

$$|\alpha_{(K\overline{K})_S^{I=0}} + \alpha_{(K\overline{K})_S^{I=1}}|^2 \quad = \quad 0.71 \pm 0.03. \tag{136}$$

In other words, the $(K\overline{K})_S$ wave can be separated from all other contributions!

With increasing $\alpha_{a_0(1450)}$, the overall amplitude $\alpha_{(K\overline{K})_S^{I=0}}$, which includes both $f_0(1370)$ and $f_0(1500)$, decreases due to constructive interference between the

two isospin states. Within $I = 0$ $(K\overline{K})_S$ wave one notices that the production strength $|\beta_r|$ of the high mass pole increases with increasing $|\alpha_{a_0(1450)}|^2$. This reflects the decreasing contribution of the low mass pole since part of the total ($I = 0$ and $I = 1$) $(K\overline{K})_S$ wave is now described by the $a_0(1450)$.

The $a_0(1450)$ has also an effect on the resonance parameters (T-matrix poles) of the $I = 0$ $(K\overline{K})_S$ wave (table 19). The $f_0(1370)$ moves downwards in mass while the width increases slightly with increasing $|\alpha_{a_0(1450)}|^2$. The mass and width of $f_0(1500)$ remain stable.

Intermediate	Fit C		Fit F1	
state	$\lvert\alpha\rvert$	ϕ	$\lvert\alpha\rvert$	ϕ
$\pi^0 a_0(1450)$	-	-	$\lvert\alpha\rvert^2 = 5\%$	5.94(32)
$m = 1470$ MeV/c^2				
$\Gamma = 265$ MeV/c^2				
$K^{*0}K^0$	0.241(6)	0	0.241(7)	0
$(K\pi^0)_S K$	0.175(8)	1.21(8)	0.176(9)	1.20(10)
$\pi^0 f_2(1275)$	0.238(16)	2.10(9)	0.238(21)	2.13(9)
$\pi^0 a_2^0(1320)$	0.291(16)	4.78(9)	0.290(16)	4.72(9)
$\pi^0 f_2'(1525)$	0.149(11)	5.19(10)	0.149(12)	5.19(12)
$\pi^0(K\overline{K})_S$	0.842(20)	5.08(4)	0.656(40)	4.95(10)
$\lvert\beta_r\rvert, \delta_r$	0.895(14)	0.71(4)	0.981(67)	0.59(7)
$\chi^2/N_{\rm dof}$	1010/767=1.32		1007/766 = 1.31	
Intermediate	Fit F2		Fit F3	
state	$\lvert\alpha\rvert$	ϕ	$\lvert\alpha\rvert$	ϕ
$\pi^0 a_0(1450)$	$\lvert\alpha\rvert^2 = 10\%$	5.88(19)	$\lvert\alpha\rvert^2 = 15\%$	5.83(10)
$K^{*0}K^0$	0.240(8)	0	0.240(7)	0
$(K\pi^0)_S K$	0.176(7)	1.19(9)	0.176(7)	1.19(9)
$\pi^0 f_2(1275)$	0.237(19)	2.14(9)	0.236(20)	2.15(9)
$\pi^0 a_2^0(1320)$	0.289(15)	4.72(9)	0.288(14)	4.73(8)
$\pi^0 f_2'(1525)$	0.149(11)	5.19(11)	0.149(12)	5.18(11)
$\pi^0(K\overline{K})_S$	0.576(36)	4.90(11)	0.516(26)	4.87(6)
$\lvert\beta_r\rvert, \delta_r$	1.028(77)	0.50(8)	1.071(58)	0.41(2)
$\chi^2/N_{\rm dof}$	1005/766=1.31		1004/766 = 1.31	

Table 18: *Scan of* $a_0(1450)$ *contributions: Amplitudes* $|\alpha|$ *and phases* ϕ.

Resonance	Fit C		Fit F1	
	m	Γ	m	Γ
	[MeV/c^2]	[MeV/c^2]	[MeV/c^2]	[MeV/c^2]
$K^{*0}(896)$	899(2)	67(3)	899(2)	68(3)
$f_2'(1525)$	1527(5)	99(11)	1527(6)	99(11)
$(K\overline{K})_S$	1361(6)	264(10)	1346(7)	278(14)
(K-matrix parameters)	1571(5)	163(6)	1570(5)	165(12)
$(K\overline{K})_S$	1404	342	1383	360
(T-matrix poles)	1517	96	1515	102
Resonance	Fit F2		Fit F3	
	m	Γ	m	Γ
	[MeV/c^2]	[MeV/c^2]	[MeV/c^2]	[MeV/c^2]
$K^{*0}(896)$	899(2)	68(3)	899(2)	68(3)
$f_2'(1525)$	1527(6)	99(12)	1526(6)	100(11)
$(K\overline{K})_S$	1338(7)	282(16)	1330(5)	283(13)
(K-matrix parameters)	1568(5)	164(12)	1566(3)	163(8)
$(K\overline{K})_S$	1373	362	1365	362
(T-matrix poles)	1515	106	1514	107

Table 19: *Scan of* $a_0(1450)$ *contributions: Masses and widths.*

9.5.6 Resonance Contributions from the $(I = 0)$ $(K\overline{K})$ S-Wave

The $I = 0$ $(K\overline{K})_S$ wave is characterized by a large overlap of the two resonances $f_0(1370)$ and $f_0(1500)$. The total intensity depends strongly on the resulting interference effects. Figure 53 shows the production amplitude $|\hat{F}|^2$ (eqn. 102) of the $(K\overline{K})_S$ wave from fit C multiplied by the $\pi^0 K_L K_L$ phase space ρ as a function of the squared $K\overline{K}$ invariant mass (curve A) [9]. The individual contributions of $f_0(1370)$ and $f_0(1500)$ within the $I = 0$ $(K\overline{K})_S$ wave are given by ignoring the non-regarded pole term of the K-matrix (eqn. 130), i.e.

$$\hat{F}(f_0(1370)) \;=\; \frac{m_1\Gamma_1/\rho_1^0}{m_1^2 - m^2 - i\rho(m_1\Gamma_1/\rho_1^0 + \Delta_{12})} \tag{137}$$

and

$$\hat{F}(f_0(1500)) \;=\; \beta_r \frac{m_2\Gamma_2/\rho_2^0}{m_2^2 - m^2 - i\rho(m_2\Gamma_2/\rho_2^0 + \Delta_{21})}. \tag{138}$$

[9] This is the projection of the $\pi^0 K_L K_L$ Dalitz plot for the case of pure $(K\overline{K})_S$ production, i.e. ignoring all other amplitudes.

These individual squared production amplitudes multiplied by the $\pi^0 K_L K_L$ phase space are superimposed on the total production amplitude of the $(K\overline{K})_S$ wave in figure 53 where $\rho|\hat{F}(f_0(1370))|^2$ and $\rho|\hat{F}(f_0(1500))|^2$ are labelled with B and C, respectively. The relative contribution r_i of either of the two resonances i to

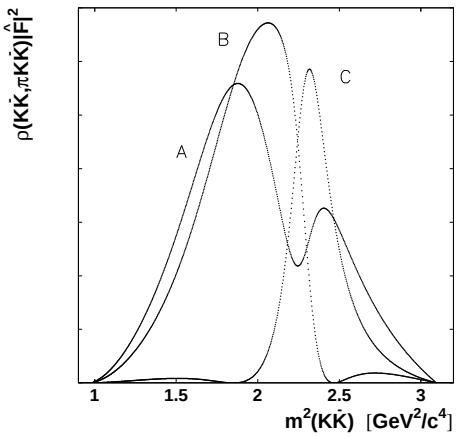

Figure 53: *$m^2(K\overline{K})$ for the $(K\overline{K})_S$ wave with parameters obtained from fit C (curve A). The individual contributions of $f_0(1370)$ (curve B) and $f_0(1500)$ (curve C) are superimposed.*

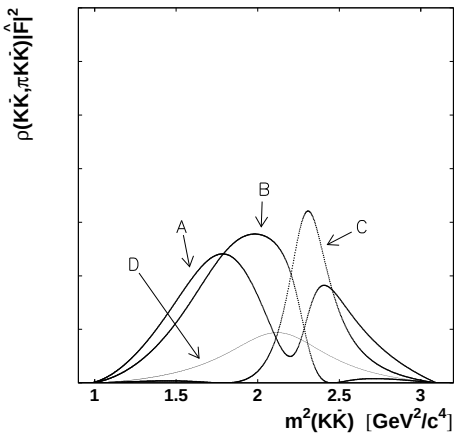

Figure 54: *Same as in figure 53 but with 15% $a_0(1450)$ contribution to $\pi^0 K_L K_L$ (curve D) . The $I = 0$ $(K\overline{K})_S$ wave with parameters obtained in fit F2 (curve A). The individual contributions of $f_0(1370)$ (curve B) and $f_0(1500)$ (curve C) are superimposed.*

the $(K\overline{K})_S$ wave is obtained by integration over the squared invariant $K\overline{K}$ mass normalized to the total $(K\overline{K})_S$ wave:

$$r_{f_0(1370)} = \frac{\int |\hat{F}(f_0(1370))|^2 d\rho}{\int |\hat{F}((K\overline{K})_S)|^2 d\rho}, r_{f_0(1500)} = \frac{\int |\hat{F}(f_0(1500))|^2 d\rho}{\int |\hat{F}((K\overline{K})_S)|^2 d\rho}. \qquad (139)$$

The absolute contribution $|\alpha_i|^2$ is then given by

$$|\alpha_i|^2 \equiv r_i \, |\alpha_{(K\overline{K})_S}|^2. \qquad (140)$$

This has been done for fit C and fits F1 to F3 in order to follow the dependence on $|\alpha_{a_0(1450)}|^2$. The effect of $a_0(1450)$ on the $I = 0$ $(K\overline{K})_S$ wave is shown for fit F2 in figure 54. The results are given in table 20. Notice that the sum $r_1 + r_2$ of the

	Fit C	Fit F1	Fit F2	Fit F3
$\lvert\alpha_{a_0(1450)}\rvert^2$	0%	5%	10%	15%
$\lvert\alpha_{(K\overline{K})_S}\rvert^2$	0.709(34)	0.430(52)	0.332(41)	0.266(27)
$r_{f_0(1370)}$	0.885	0.880	0.877	0.871
$r_{f_0(1500)}$	0.360	0.417	0.451	0.484
$\lvert\alpha_{f_0(1370)}\rvert^2$	0.627(30)	0.378(46)	0.291(36)	0.232(24)
$\lvert\alpha_{f_0(1500)}\rvert^2$	0.255(12)	0.179(22)	0.150(18)	0.129(13)

Table 20: *Relative $f_0(1370)$ and $f_0(1500)$ contributions to the $I = 0$ $(K\overline{K})_S$ wave (r_i) and in the $\pi^0 K_L K_L$ data ($|\alpha_i|^2$).*

two individual contributions is more than 100% due to interference between the two scalars. The contributions $|\alpha_i|^2$ decrease for both resonances as $|\alpha_{a_0(1450)}|^2$ increases.

9.5.7 Other Tests

In the analysis of Conforto et al. [31], the $(K\pi)_S$ wave was parametrized with a scattering length. This is very different to the analysis of the present work. Here, the parametrization of the dynamical amplitude for the $(K\pi)_S$ wave considers the production of $K_0^{*0}(1430)$. When the $(K\pi)_S$ wave was omitted from the hypothesis of fit C, a drastic effect was observed for the $(K\overline{K})_S$ wave: The K-matrix poles moved to 1285 MeV/c^2 for the low mass pole and to 2193 MeV/c^2 for the high mass pole. The widths were 214 MeV/c^2 and 196 MeV/c^2, respectively. Figure 55 shows the invariant mass squared spectrum $m^2(K\overline{K})$ where the curve gives the result of the fit without $(K\pi)_S$ wave. The dip corresponding to a mass of about 1500 MeV/c^2 could not be described from which a bad χ^2 of $1180/788 - 19 = 1.53$ resulted. It is concluded that only if the $K_0^{*0}(1430)$ is produced, the $(K\overline{K})_S$ wave is able to describe the rapid change in the intensity of $m^2(K\overline{K})$ around 2.25 GeV$^2/c^4$.

In the previous fits it was assumed that K^*K production from $I = 0$ $\overline{p}p$ initial state dominates the production from $I = 1$ due to the observation of constructive interference in the crossing region of the two $K^{*0}(896)$ bands. This assumption was tested by adding the $I = 1$ $K^{*0}(896)K^0$ intermediate state to the hypothesis of fit C. This amplitude affects only the density distribution in the

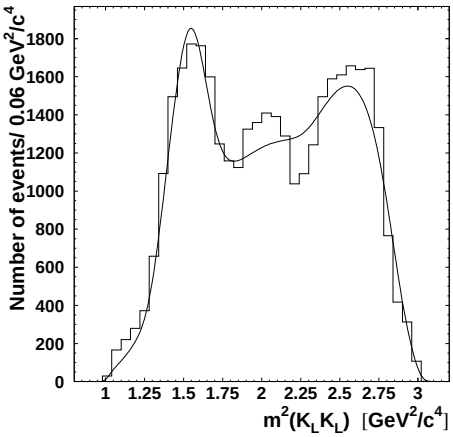

Figure 55: *Invariant mass* $m^2(K\overline{K})$. *The curve shows the result of the fit without* $(K\pi)_S$ *wave.*

crossing region of the $K^{*0}(896)$ bands. In this region only the K^*K amplitudes from $I = 0$ contribute since those from $I = 1$ initial $\overline{p}p$ state interfere destructive. Far off the crossing region the K^*K intensity is given by the coherent sum of both transition amplitudes $A^{I=0}_{K^{*0}(896)}$ and $A^{I=1}_{K^{*0}(896)}$.

The χ^2 improved slightly (988/788-23=1.29). The results are given in table 21. For the $K^{*0}(896)$ contribution from the $I = 1$ $\overline{p}p$ initial state one finds:

$$2 \times |\alpha^{I=1}_{K^{*0}(896)}|^2 \quad = \quad (1.3 \pm 0.5) \times 10^{-3}, \tag{141}$$

where the factor 2 accounts for the two amplitudes $K^{*0}(896)K$ and $KK^{*0}(896)$. All other parameters, in particular the corresponding $K^{*0}(896)K^0$ amplitudes from $I = 0$ initial state are consistent with those from fit C for which

$$2 \times |\alpha^{I=0}_{K^{*0}(896)}|^2 \quad = \quad (11.6 \pm 0.5) \times 10^{-2}. \tag{142}$$

Hence, the assumption of $I = 0$ dominance for $K^{*0}(896)K^0$ production from $^1S_0$ initial state is justified.

Also the $(K\pi)_S$ wave can contribute from both $I = 0$ and $I = 1$ initial states. No significant contribution from the $I = 1$ initial state was observed.

Intermediate state	$\|\alpha\|$	Phase ϕ [rad]	Mass [MeV/c^2]	Width [MeV/c^2]
$K^{*0}(896)K^0$ $I=0$	0.242(6)	0.	900(2)	69(3)
$K^{*0}(896)K^0$ $I=1$	0.025(5)	4.84(24)	dito	dito
$K_0^{*0}(1430)K^0$	0.180(7)	1.24(8)	$K\pi$ S-wave	
$f_2(1275)\pi$	0.234(19)	2.13(8)	1275	185
$a_2(1320)\pi$	0.290(15)	4.73(8)	1320	105
$f_2'(1525)\pi$	0.148(11)	5.22(10)	1527(5)	99(11)
$(K\overline{K})_S\pi$	0.849(22)	5.08(3)	K-matrix pole 1:	
			1358(3)	272(8)
			K-matrix pole 2:	
	$\|\beta_r\| = 0.88(2)$	$\delta_r = 0.70(2)$	1568(4)	160(7)
$\chi^2/N_{dof} = 988/(788-23) = 1.29$				

Table 21: *Results for the hypothesis including $K^{*0}(896)K$ from $I=1$ $\overline{p}p$ initial state*

The low mass $K\overline{K}$ region could not be explained in a satisfactory way with any of the previous hypotheses. The difficulties in introducing $a_0(980)$ and $f_0(980)$ are the following:

1. Both resonances have to be considered simultaneously since they are produced in their decay into $\pi\eta$ and $\pi\pi$ in the reactions $\overline{p}p \to 2\pi^0\eta$ [43] and $\overline{p}p \to 3\pi^0$ [12], respectively.

2. They interfere among themselves. No prominent threshold enhancement due to $f_0(980)$ and/or $a_0(980)$ is observed in the Dalitz plot of figure 39. This is very much in contrast to the final state $\pi^{\pm}K^{\mp}K_S$ [31] where $a_0(980)$ generates a threshold enhancement at low $K\overline{K}$ mass. The absence of signal in $\pi^0K_SK_S$ [31] and in $\pi^0K_LK_L$ points to destructive interference between $a_0(980)$ and $f_0(980)$, similar to $a_2(1320)$ and $f_2(1270)$ (see section 9.5.3).

3. They interfere with the $(K\pi)_S$ wave which, due to constructive self-interference, can also produce a $K\overline{K}$ threshold enhancement.

Two 2×2 K-matrices would have to be used to account for the couplings to $\pi\eta$ and $\pi\pi$. For the $a_0(980)$, the couplings to the decay channels are not well known. The same is true for $f_0(980)$.

Any attempt to account for a $K\overline{K}$ resonance at threshold, by using $a_0(980)$ with fixed couplings from ref. [59], failed since high correlations with the $(K\pi)_S$ wave occurred which prevented the fit to converge properly.

9.6 Interferences

The minimum number of resonances needed to describe the $\pi^0 K_L K_L$ Dalitz plot was therefore seven:

1. $K^{*0}(896)$,
2. $K^{*0}(1430)$ within the $(K\pi)_S$ wave,
3. $f_2(1275)$,
4. $a_2(1320)$,
5. $f_2'(1525)$,
6. $f_0(1370)$ within the $(K\overline{K})_S$ wave and
7. $f_0(1500)$ also within the $(K\overline{K})_S$ wave.

Figures 56 to 60 show Monte Carlo simulations of the individual transition amplitudes $|A_i|^2$ (section 9.3). Masses and widths are taken from the results of fit C.

The simulation of $\overline{p}p(^1S_0, I = 0) \rightarrow K^*K, KK^*$ shows the decay angular distribution proportional to $\cos^2\theta$ of the $K^*(896)$ which results in enhancements at the borders of the Dalitz plot (figure 56). The constructive interference between the K^*K and KK^* amplitudes manifestes itself by the accumulation of events in the crossing region of the $K^*(896)$ bands.

The amplitudes from $\overline{p}p(^1S_0, I = 0) \rightarrow (K\pi)_S K', (K'\pi)_S K$ (figure 57) contribute to any region of the Dalitz plot. The accumulation of events at low $K\overline{K}$ masses results from the constructive interference between the two amplitudes $(K\pi)_S K'$ and $(K'\pi)_S K$.

The tensor resonances $a_2(1320)$, $f_2(1270)$ and $f_2'(1525)$ are responsible for enhancements of events at the border and in the center of the Dalitz plot due to

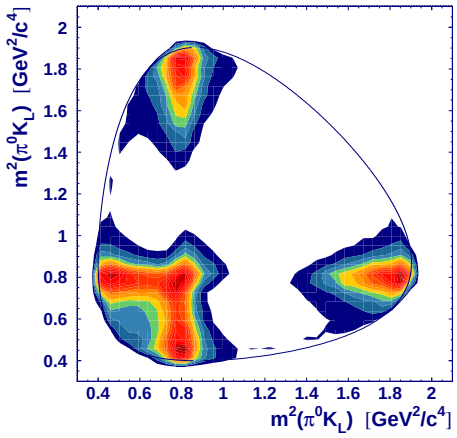

Figure 56: *Monte Carlo simulation of* $K^{*0}(896)$ *in* $\pi^0 K_L K_L$.

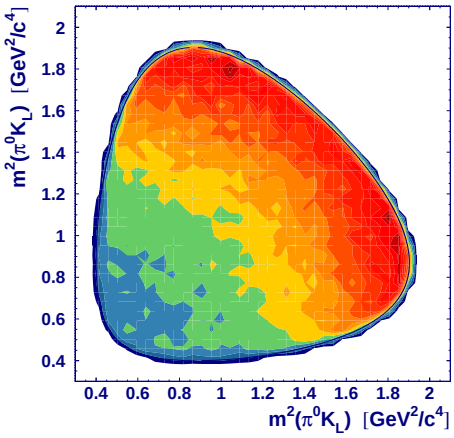

Figure 57: *Monte Carlo simulation of* $(K\pi)_S$ *wave in* $\pi^0 K_L K_L$.

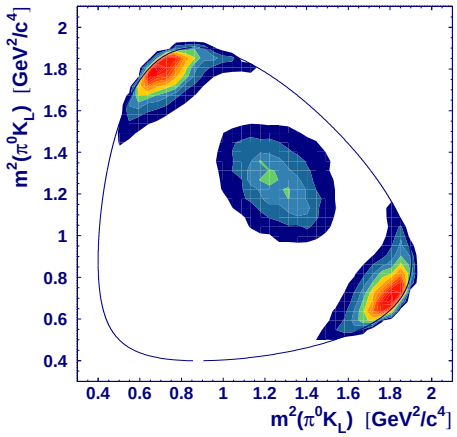

Figure 58: *Monte Carlo simulation of* $f_2(1270)$ *in* $\pi^0 K_L K_L$.

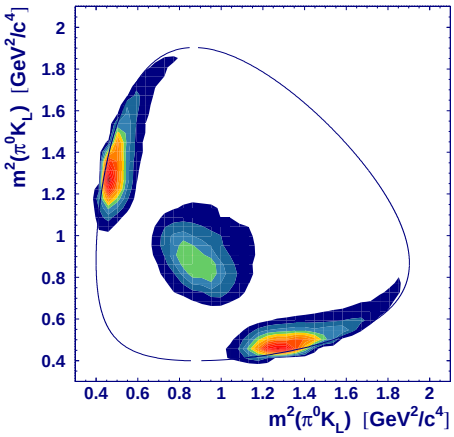

Figure 59: *Monte Carlo simulation of* $f_2'(1525)$ *in* $\pi^0 K_L K_L$.

the decay angular distribution which is proportional to $(9\cos^4\theta - 6\cos^2\theta + 1)$ (figures 58 and 59).

The simulation of the $(K\overline{K})_S$ wave with parameters obtained from fit C is shown in figure 60. The maximum intensities occur at $K\overline{K}$ masses corresponding to the K-matrix poles 1361 MeV/c^2 and 1571 MeV/c^2.

It shall now be discussed, how the positions of these maxima change when the $(K\overline{K})_S$ wave interferes with other resonances. In order to understand the effects of interferences, it is necessary to emphazise that the observed intensity is the coherent sum of complex amplitudes. Consider the interference of two resonances with masses m_1 and m_2, parametrized as Breit-Wigner amplitudes BW_1 and BW_2, decaying both into the same two-body final state (e.g. $K\overline{K}$). Suppose $\alpha_1 = \alpha_2 = 1$, i.e. $\phi_1 = \phi_2 = 0$, then the total observed intensity is

$$I = |BW_1 + BW_2|^2 = |BW_1|^2 + |BW_2|^2 + 2Re(BW_1)Re(BW_2). \qquad (143)$$

The real part of a Breit-Wigner amplitude is

$$Re(BW_i) = \frac{m_i\Gamma_i/\rho_i^0}{(m_i^2 - m^2)^2 + m_i^2\Gamma_i^2(m)}(m_i^2 - m^2)\begin{cases} > 0 \text{ for } m_i > m \\ < 0 \text{ for } m_i < m \end{cases} \qquad (144)$$

and hence the total intensity I in eqn. 143 at the mass m is increased if $m > m_1, m_2$ or $m < m_1, m_2$ or is decreased if $m_1 < m < m_2$.

First, interference with $f_2'(1525)$ is considered. The density distribution in the $K\overline{K}$ system is modified such that the depletion around 1500 MeV/c^2, already present in the $(K\overline{K})_S$ wave, is now even more pronounced in the center of the Dalitz plot (figure 61).

The destructive interference between the $(K\overline{K})_S$ wave and $f_2(1270)$ (table 13) results in a strongly reduced intensity at the border of the Dalitz plot at the mass of $f_2(1270)$ (figure 62).

The relative phase between $a_2(1320)$ and the $(K\overline{K})_S$ wave is close to zero and the interference behaves similar to eqn. 143. The low mass K-matrix pole lies at 1361 MeV/c^2 and thus, for $1320 < m < 1361$ MeV/c^2, the total intensity is reduced which results in a second depletion in the center of the Dalitz plot (figure 63). The interference between $a_2(1320)$ and the $(K\overline{K})_S$ wave is responsible for the (narrow) peak around 1450 MeV/c^2 observed in $K\overline{K}$.

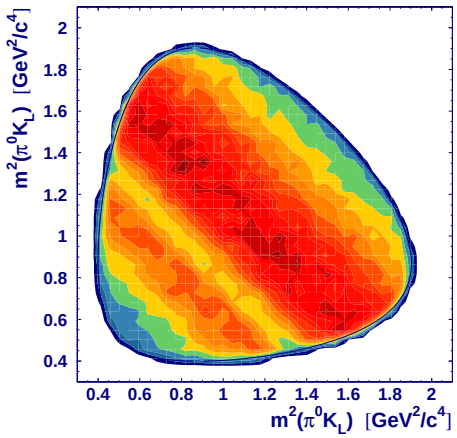

Figure 60: *MC simulation of* $(K\overline{K})_S$ *wave in* $\pi^0 K_L K_L$ *. The K-matrix parameters are taken from fit C.*

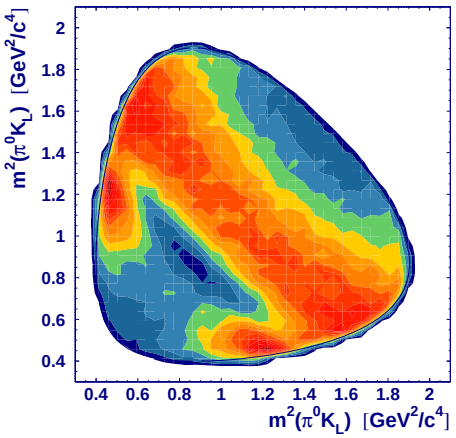

Figure 61: $(K\overline{K})_S$ *wave and* $f_2'(1525)$.

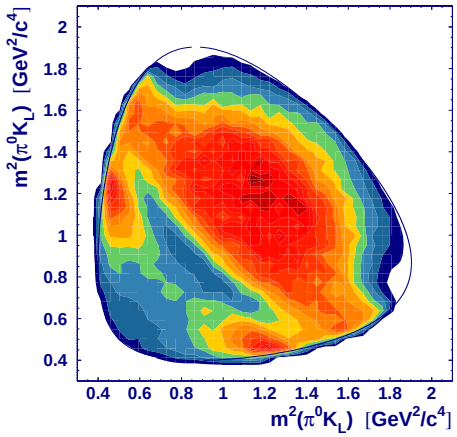

Figure 62: $(K\overline{K})_S$, $f_2'(1525)$ *and* $f_2(1275)$.

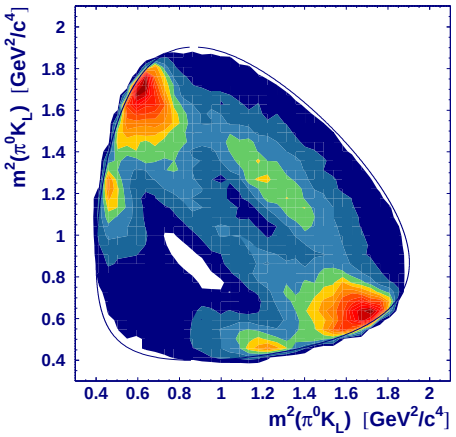

Figure 63: $(K\overline{K})_S$ *wave,* $f_2'(1525)$, $f_2(1275)$ *and* $a_2(1320)$.

Figure 64 shows the situation including the $K^{*0}(896)$. The depletion around 1500 MeV/c^2 is less pronounced due to the strong contribution of the crossing of the two K^* bands. An important effect has also the $(K\pi)_S$ wave which, due to

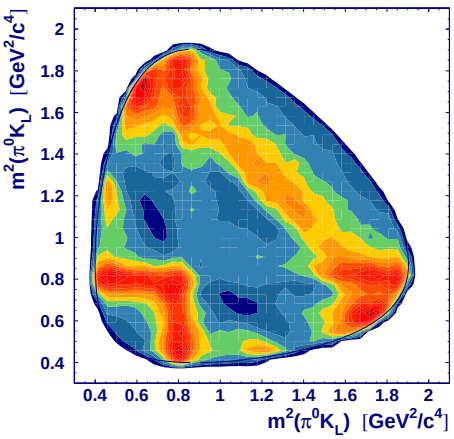

Figure 64: $(K\overline{K})_S$ *wave,* $f_2(1275)$, $a_2(1320)$, $f_2'(1525)$ *and* $K^{*0}(896)$.

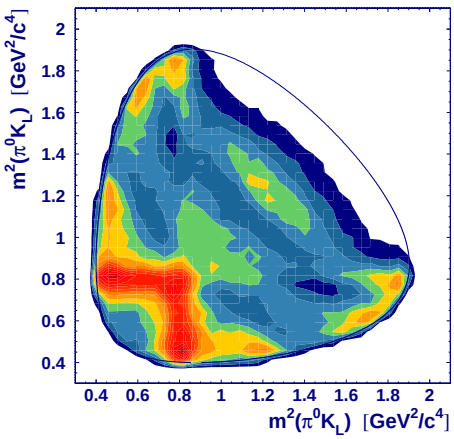

Figure 65: $(K\overline{K})_S$ *wave,* $f_2(1275)$, $a_2(1320)$, $f_2'(1525)$, $K^{*0}(896)$ *and* $(K\pi)_S$ *wave (Result of Fit C).*

destructive interference with the $(K\overline{K})_S$ wave, reduces appreciably the intensity at low $K\overline{K}$ masses (figure 65). This figure represents the final result of fit C. The original structure of the $(K\overline{K})_S$ wave is no more visible and hidden by interferences with all other partial waves.

10 Branching Ratios

The absolute reconstruction efficiency for $\overline{p}p \to \pi^0 K_L K_L$ could not be derived from GEANT simulations since the hadronic interactions of K_L are not well described at low energies. Hence, the weighted average of $B(\overline{p}p \to \pi^0 K_S K_S)$ from Barash et al. [32] and Armenteros et al. [30] was used to deduce branching ratios for the intermediate states in $\pi^0 K_L K_L$:

$$B(\overline{p}p \to \pi^0 K_S K_S) = B(\overline{p}p \to \pi^0 K_L K_L) = (7.5 \pm 0.3) \times 10^{-4}. \qquad (145)$$

The density in the $\pi^0 K_L K_L$ Dalitz plot is a result of interferences between all partial waves. Thus, the number of produced events is in general different the number of observed events which means that

$$\sum_i |\alpha_i|^2 \neq 1 \tag{146}$$

where the sum extends over all (normalized) partial waves. A particular example is the $(K\overline{K})_S$ wave for which the sum of the individual contributions of $f_0(1370)$ and $f_0(1500)$ is greater than the total contribution of the $(K\overline{K})_S$ wave (table 22). In this work, branching ratios are given by neglecting the interferences and hence, the branching ratio B_i for a partial wave i is

$$B_i = |\alpha_i|^2 \times B(\overline{p}p \to \pi^0 K_L K_L). \tag{147}$$

All branching ratios are based on the results from fit C with in addition fits F1, F2 and F3 with fixed $a_0(1450)$ contributions since the latter influence appreciably the branching ratios for $f_0(1370)$ and $f_0(1500)$.

10.1 K^*K Production

Since also the self-interference of the two partial waves $K^{*0}\overline{K}^0$ and $\overline{K}^{*0}K^0$ is neglected, the total contribution of $K^{*0}K^0 = K^{*0}\overline{K^0} + \overline{K}^{*0}K^0$ in $\pi^0 K_L K_L$ is given by

$$|\alpha|^2 = 2 \times |\alpha_{(K^{*0}K^0)}|^2 \tag{148}$$

from which with $|\alpha_{(K^{*0}K^0)}|^2 = (5.81 \pm 0.29) \times 10^{-2}$ follows:

$$B(\overline{p}p(^1S_0) \to K^{*0}K_L \to \pi^0 K_L K_L) = (8.71 \pm 0.68) \times 10^{-5}. \tag{149}$$

According to the isospin decomposition (section 9.1), this result has to be multiplied by 12 in order to obtain the production rate for K^*K including all charge configurations from the $^1S_0$ $\overline{p}p$ initial state:

$$B(\overline{p}p(^1S_0, I=0) \to K^*K) = (10.45 \pm 0.82) \times 10^{-4}, \tag{150}$$

which is in good agreement with $B(\overline{p}p(^1S_0, I=0) \to K^*K) = (8.4 \pm 1.4) \times 10^{-4}$ from Conforto et al.[31]. It is noted, that this production rate depends slightly

Reaction	Contribution $\|\alpha\|^2$
$\overline{p}p(^1S_0, I=0) \to K^{*0}K_L, K^{*0} \to K_L\pi^0$	$(5.81 \pm 0.29) \times 10^{-2}$
$\overline{p}p(^1S_0, I=0) \to K_L K^{*0}, K^{*0} \to K_L\pi^0$	$(5.81 \pm 0.29) \times 10^{-2}$
$\overline{p}p(^1S_0, I=1) \to K^{*0}K_L, K^{*0} \to K_L\pi^0$	$(0.65 \pm 0.25) \times 10^{-2}$
$\overline{p}p(^1S_0, I=1) \to K_L K^{*0}, K^{*0} \to K_L\pi^0$	$(0.65 \pm 0.25) \times 10^{-2}$
$\overline{p}p(^1S_0, I=0) \to (K_L\pi^0)_S K_L, (K_L\pi^0)_S \to K_L\pi^0$	$(3.06 \pm 0.28) \times 10^{-2}$
$\overline{p}p(^1S_0, I=0) \to K_L (K_L\pi^0)_S, (K_L\pi^0)_S \to K_L\pi^0$	$(3.06 \pm 0.28) \times 10^{-2}$
$\overline{p}p(^1S_0, I=0) \to \pi^0 a_2(1320), a_2(1320) \to K_L K_L$	$(8.47 \pm 0.93) \times 10^{-2}$
$\overline{p}p(^1S_0, I=1) \to \pi^0 f_2(1270), f_2(1270) \to K_L K_L$	$(5.66 \pm 0.76) \times 10^{-2}$
$\overline{p}p(^1S_0, I=1) \to \pi^0 f_2'(1525), f_2'(1525) \to K_L K_L$	$(2.22 \pm 0.33) \times 10^{-2}$
$\overline{p}p(^1S_0) \to \pi^0 (K\overline{K})_S, (K\overline{K})_S \to K_L K_L$	$(70.9 \pm 3.4) \times 10^{-2}$

$\|\alpha_{a_0(1450)}\|^2$	$\|\alpha_{f_0(1370)}\|^2$	$\|\alpha_{f_0(1500)}\|^2$
0 %	$(62.7 \pm 3.0) \times 10^{-2}$	$(25.5 \pm 1.2) \times 10^{-2}$
5 %	$(37.8 \pm 4.6) \times 10^{-2}$	$(17.9 \pm 2.2) \times 10^{-2}$
10 %	$(29.1 \pm 3.6) \times 10^{-2}$	$(15.0 \pm 1.8) \times 10^{-2}$
15 %	$(23.2 \pm 2.4) \times 10^{-2}$	$(12.9 \pm 1.3) \times 10^{-2}$

Table 22: *Contributions $|\alpha|^2$ of all measured reactions leading to the $\pi^0 K_L K_L$ final state. Note that $\sum_i |\alpha|^2 \neq 1$. The lower part of the table gives the contributions $|\alpha_{f_0(1370)}|^2$ and $|\alpha_{f_0(1500)}|^2$ as a function of $a_0(1450)$ contribution $|\alpha_{a_0(1450)}|^2$ to $\pi^0 K_L K_L$.*

on the assumption made on the $(K\pi)_S$ wave for which Conforto et al. [31] used a scattering length approximation without the (at that time unknown) $K^{*0}(1430)$.

The production rate for K^*K from $I = 1$ $\overline{p}p$ initial state is small. One finds (see section 9.5.7):

$$B(\overline{p}p(^1S_0, I=1) \to K^*K) = (1.17 \pm 0.45) \times 10^{-5}. \qquad (151)$$

The corresponding value[10] from Conforto et al. depends strongly on the choice of the scattering length for the $(K\pi)_S$ wave [31] and varies between 9.9×10^{-5} and 9.1×10^{-4}.

10.2 $K_0^*(1430)K$ Production

The formulation of the dynamical amplitude of the $(K\pi)_S$ wave assumes the production of the resonance $K_0^*(1430)$. The decay is modified by $K\pi$ interactions at low energies which is parametrized by the K-matrix including the effective

[10]From the analysis of $\overline{p}p \to \pi^0 K_S K_S$ (*p.* 499 of ref. [31]).

range approximation. It is the first time that $K_0^*(1430)$ is considered in this form in the analysis of $\overline{p}p$ annihilation into $\pi K\overline{K}$. The branching ratio is, with $|\alpha_{(K\pi)_S}|^2 = (3.06 \pm 0.28) \times 10^{-2}$ multiplied by 2,

$$B(\overline{p}p(^1S_0) \to K_0^{*0}(1430)K_L \to \pi^0 K_L K_L) = (4.59 \pm 0.46) \times 10^{-5}. \qquad (152)$$

The production rate is given by multiplying this result by 12 to account for all charge configrations:

$$B(\overline{p}p(^1S_0, I = 0) \to K_0^*(1430)K) = (5.51 \pm 0.55) \times 10^{-4}. \qquad (153)$$

It is reminded that the $(K\pi)_S$ wave describes the behaviour at low $K\overline{K}$ masses in the $\pi^0 K_L K_L$ Dalitz plot. From the $\pi^0 K_L K_L$ data alone it is not possible to determine the contributions of $a_0(980)$ and $f_0(980)$ due to large correlations with the $(K\pi)_S$ wave. A coupled channel fit to other final states (e.g. $\pi^{\pm}K^{\mp}K_S$) would constrain the $a_0(980)$ and $f_0(980)$ production amplitudes and couplings to $K\overline{K}$ and might therefore change the result on the $K_0^*(1430)K$ production rate from both $I = 0$ and $I = 1$ (which is not given here) initial states.

10.3 $a_2(1320)$ Production

Since both $a_2(1320)$ and the recoiling π^0 are isovectors, the annihilation into $\pi^0 a_2^0(1320)$ proceeds from the $I = 0$ $\overline{p}p$ initial state (see section 9.1). The branching ratio for $\overline{p}p$ annihilation into $\pi^0 a_2^0(1320)$ ($a_2^0(1320) \to K_L K_L$) is, with $|\alpha_{a_2}|^2 = (8.47 \pm 0.93) \times 10^{-2}$,

$$B(\overline{p}p(^1S_0) \to \pi^0 a_2^0(1320) \to \pi^0 K_L K_L) \;=\; (6.35 \pm 0.74) \times 10^{-5}. \qquad (154)$$

The total production rate, including annihilations from the $^1S_0$ $\overline{p}p$ initial state into $\pi^+ a_2^-$, $\pi^- a_2^+$ and $\pi^0 a_2^0$, is again obtained by multiplying by 12:

$$B(\overline{p}p(^1S_0) \to \pi a_2(1320) \to \pi K\overline{K}) \;=\; (7.62 \pm 0.89) \times 10^{-4} \qquad (155)$$

which is consistent with $B(\overline{p}p(^1S_0, I = 0) \to \pi a_2(1320) \to \pi K\overline{K}) = (6.5 \pm 1.8) \times 10^{-4}$ from Conforto et al [31]. Correcting the production rate from eqn. 155 for

the unseen decays by dividing the production rate in eqn. 155 by $B(a_2(1320) \to K\overline{K}) = (4.9 \pm 0.8) \times 10^{-2}$ [29], one then obtains

$$B(\overline{p}p(^1S_0) \to \pi a_2(1320)) \quad = \quad (1.55 \pm 0.31) \times 10^{-2}. \tag{156}$$

This result is compared to the production rate of $B(\overline{p}p(^1S_0) \to \pi a_2(1320)) = (3.95 \pm 1.01) \times 10^{-2}$ deduced from the reaction $\overline{p}p \to \pi^0 a_2^0(1320)$ where $a_2^0(1320) \to \pi^0\eta$ [43]. The two results differ in the order of two standard deviations.

10.4 $f_2(1270)$ Production

The annihilation into $\pi^0 f_2(1270)$ proceeds, in contrast to $\pi^0 a_2^0(1320)$, only from the $I = 1$ $\overline{p}p$ initial state. Considering only the decay $f_2(1270) \to K_L K_L$ one finds with $|\alpha_{f_2}|^2 = (5.66 \pm 0.76) \times 10^{-2}$ a branching ratio of

$$B(\overline{p}p(^1S_0) \to \pi^0 f_2(1270) \to \pi^0 K_L K_L) \quad = \quad (4.25 \pm 0.59) \times 10^{-5}. \tag{157}$$

With $B(f_2(1270) \to K\overline{K}) = (4.6 \pm 0.5) \times 10^{-2}$ [29] and correcting for all kaonic decay modes, one obtains the total production rate for $\overline{p}p$ annihilations from $^1S_0$ $\overline{p}p$ initial state into $f_2(1270)\pi^0$

$$\begin{aligned} B(\overline{p}p(^1S_0) \to \pi^0 f_2(1270)) \quad &= \quad \frac{4B(\overline{p}p \to \pi^0 f_2(1270) \to \pi^0 K_L K_L)}{B(f_2(1270) \to K\overline{K})} \\ &= \quad (3.70 \pm 0.66) \times 10^{-3}, \end{aligned} \tag{158}$$

which agrees perfectly with previous measurements: The ASTERIX collaboration analyzed $\overline{p}p \to \pi^+\pi^-\pi^0$ and found $B(\overline{p}p(^1S_0) \to \pi^0 f_2(1270)) = (3.9 \pm 1.1) \times 10^{-3}$ [61]. Assuming annihilation from $^1S_0$ $\overline{p}p$ initial state, the Crystal Barrel collaboration measured in the reaction $\overline{p}p \to 3\pi^0$ a production rate of $B(\overline{p}p(^1S_0) \to \pi^0 f_2(1270)) = (4.05 \pm 1.97) \times 10^{-3}$ [62]. It is noted that the branching ratios derived from the $3\pi^0$ final state vary slightly with the assumptions made on the contributing initial states.

10.5 $f_2'(1525)$ Production

The contribution of $f_2'(1525)$ to $\pi^0 K_L K_L$ was very stable with respect to the different hypotheses which have been tested. The scan with fixed $f_2'(1525)$ contributions has shown that, even if the contribution is small ($|\alpha_{f_2'}|^2 = (2.22 \pm$

$0.33) \times 10^{-2}$), the total χ^2 is very sensitive to different values of $|\alpha_{f_2'}|^2$ (section 9.5.4).

The branching ratio is

$$B(\overline{p}p(^1S_0) \to \pi^0 f_2'(1525) \to \pi^0 K_L K_L) \quad = \quad (1.67 \pm 0.26) \times 10^{-5}. \quad (159)$$

Multiplying this result by 4 to account for all kaonic decay modes and correcting also for unseen decays of $f_2'(1525)$ by considering the branching ratio $B(f_2'(1525) \to K\overline{K}) = (71.2 \pm^{2.5}_{2.0}) \times 10^{-2}$ [29], one obtains the total production rate:

$$\begin{aligned} B(\overline{p}p(^1S_0) \to \pi^0 f_2'(1525)) &= \frac{4B(\overline{p}p(^1S_0) \to \pi^0 f_2'(1525) \to \pi^0 K_L K_L)}{B(f_2'(1525) \to K\overline{K})} \\ &= (9.38 \pm 1.49) \times 10^{-5}, \end{aligned} \quad (160)$$

which is measured for the first time, since $f_2'(1525)$ has not been observed so far in $\overline{p}p$ annihilation at rest. The Quark Line Rule states that the production of neutral resonances in $\overline{p}p$ annihilation occurs only through the $u\overline{u}$ or $d\overline{d}$ part of their quark wave function. The ratio of the production rates of the two isoscalar members is related to the mixing angle of the corresponding nonet [63]. For the tensor mesons $f_2(1270)$ and $f_2'(1525)$ the ratio is

$$\frac{B(\overline{p}p \to f_2'\pi^0)}{B(\overline{p}p \to f_2\pi^0)} \quad = \quad \tan^2(\theta_{2^{++}} - \theta_{ideal}), \quad (161)$$

where $\theta_{2^{++}}$ denotes the mixing angle of the 2^{++} meson nonet. The ideal mixing angle is $\theta_{ideal} = 35.3°$. In the case of ideal mixing, i.e. $\theta_{2^{++}} = \theta_{ideal}$, the production of $f_2'(1525)$ would vanish exactly. With the results from eqn. 158 and 160, the deviation from ideal mixing is

$$\theta_{2^{++}} - \theta_{ideal} \quad = \quad \pm(9.1 \pm 1.1)°. \quad (162)$$

The negative solution yields for the 2^{++} mixing angle

$$\theta_{2^{++}} \quad = \quad (26.2 \pm 1.1)°, \quad (163)$$

which agrees perfectly with the PDG value $\theta_{2^{++}} = 26°$ [29] from the linear mass formula.

10.6 $f_0(1370) - f_0(1500)$ Production

The $(K\overline{K})_S$ wave is characterized by strong interferences between the two isoscalar states $f_0(1370)$ and $f_0(1500)$ and the isovector state $a_0(1450)$. The $\pi^0 K_L K_L$ final state alone is not sufficient to fix the fraction of $a_0(1450)$ since any contribution of the expected magnitude up to 15% in $\pi^0 K_L K_L$ yields the same χ^2 without affecting the other partial waves. It was mentionned in section 9.5.5 that the total contribution of the $(K\overline{K})_S$ wave including both isospin states $I = 0$ and $I = 1$ is constant and independent of the magnitude of the $a_0(1450)$ contribution. The production rate for the total $(K\overline{K})_S$ wave is, with $|\alpha(K\overline{K})_S|^2 = (70.9 \pm 3.4) \times 10^{-2}$,

$$\begin{aligned} B(\overline{p}p(^1S_0) \to \pi^0(K\overline{K})_S) &= 4\, B(\overline{p}p(^1S_0) \to \pi^0 K_L K_L) \times |\alpha_{(K\overline{K})_S}|^2 \\ &= (2.1 \pm 0.2) \times 10^{-3}, \end{aligned} \tag{164}$$

where the error includes the uncertainties in the different fits.

The results from fit C and fits F1, F2 and F3 are used to derive the production rates which are listed in table 23. They include all $K\overline{K}$ decay modes and have been calculated by

$$B(\overline{p}p(^1S_0) \to \pi^0 f_0, f_0 \to K\overline{K}) = 4\, B(\overline{p}p(^1S_0) \to \pi^0 K_L K_L) \times |\alpha_{f_0}|^2, \tag{165}$$

where f_0 stands for either of the two scalars and $|\alpha_{f_0}|^2$ is the fraction of the corresponding state in $\pi^0 K_L K_L$ from table 22. The production rates are also shown as a function of $a_0(1450)$ contribution in $\pi^0 K_L K_L$ in figure 66. The rates

$a_0(1450)$ contribution in $\pi^0 K_L K_L$	$B(\overline{p}p(^1S_0) \to f_0(1370)\pi^0$	$B(\overline{p}p(^1S_0) \to f_0(1500)\pi^0$
0% (Fit C)	$(18.8 \pm 1.2) \times 10^{-4}$	$(7.7 \pm 0.5) \times 10^{-4}$
5% (Fit F1)	$(11.3 \pm 1.5) \times 10^{-4}$	$(5.4 \pm 0.7) \times 10^{-4}$
10% (Fit F2)	$(8.7 \pm 1.1) \times 10^{-4}$	$(4.5 \pm 0.3) \times 10^{-4}$
15% (Fit F3)	$(7.0 \pm 0.8) \times 10^{-4}$	$(3.9 \pm 0.4) \times 10^{-4}$

Table 23: *Production rates for $f_0(1370)$ and $f_0(1500)$ in their $K\overline{K}$ decay mode as a function of $a_0(1450)$ contribution to the full $\pi^0 K_L K_L$ Dalitz plot.*

for $f_0(1370)$ can be compared with the analysis of $\overline{p}p \to 3\pi^0$ where the branching ratio $B(\overline{p}p \to f_0(1370)\pi^0, f_0(1370) \to \pi^0\pi^0) < (2.6 \pm 0.4) \times 10^{-3}$ was measured

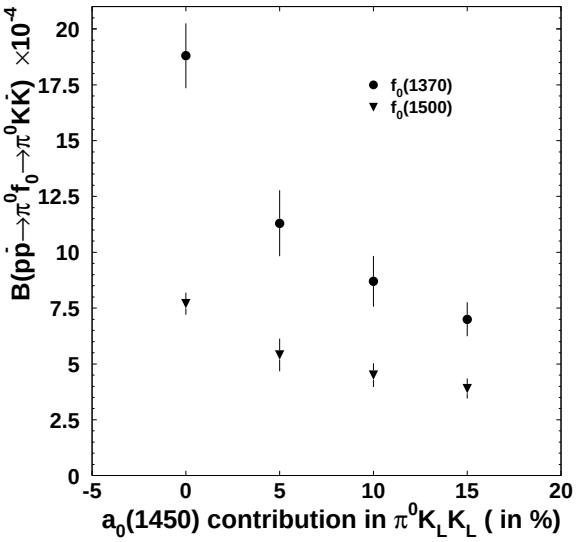

Figure 66: *Production rates of* $f_0(1370)$ *and* $f_0(1500)$ *as a function of* $a_0(1450)$ *contribution to* $\pi^0 K_L K_L$.

[12]. This is an upper limit since the measured branching ratio also includes some contribution from $f_0(980)$.

The invariant couplings (in absence of phase space and form factors) of an isoscalar $(u\overline{u} + d\overline{d})$ state decaying into $K\overline{K}$ relative to $\pi\pi$ is [25]

$$\frac{\gamma^2(f \to K\overline{K})}{\gamma^2(f \to \pi\pi)} = \frac{1}{3}, \tag{166}$$

when flavour symmetry and ideal mixing in the 0^{++} nonet are assumed. The branching ratios are related to the invariant couplings via

$$\frac{\gamma^2(f_0 \to K\overline{K})}{\gamma^2(f_0 \to \pi\pi)} = \frac{1}{3}\frac{B(\overline{p}p \to f_0\pi^0, f_0 \to K\overline{K})}{B(\overline{p}p \to f_0\pi^0, f_0 \to \pi^0\pi^0)}\frac{q_{\pi\pi}}{q_{K\overline{K}}}\frac{F_{\pi\pi}}{F_{K\overline{K}}}. \tag{167}$$

where F is a form factor [64]:

$$F(q) = e^{-q^2/8\beta^2}. \tag{168}$$

The factor 3 in the numerator of eqn. 167 accounts for the three charge combinations $\pi^0\pi^0$, $\pi^+\pi^-$ and $\pi^-\pi^+$. With $B(\overline{p}p \to f_0(1370)\pi^0, f_0 \to \pi^0\pi^0) <$

$(2.6 \pm 0.4) \times 10^{-3}$ [12][25], $\beta = 0.5$ GeV/c [25] and the break-up momenta $q_{K\overline{K}} = 0.471$ GeV/c and $q_{\pi^0\pi^0} = 0.672$ GeV/c one obtains

$$\frac{\gamma^2(f_0(1370) \to K\overline{K})}{\gamma^2(f_0(1370) \to \pi\pi)} \quad > \quad (163.1 \pm 25.1)\, B(\overline{p}p \to f_0\pi^0, f_0 \to K\overline{K}), \quad (169)$$

where f_0 stands for $f_0(1370)$. The couplings obtained from fits C, F1, F2 and F3 are listed in table 24.

The result from fit C with no $a_0(1450)$ contribution is consistent with the expectations from SU(3) couplings (assuming ideal mixing in the 0^{++} nonet). Note that $(7.7 \pm 2.1)\%$ is the expected contribution from $a_0(1450)$ deduced from $B(\overline{p}p \to a_0^0(1450)\pi^0)$ where $a_0^0(1450) \to \pi^0\eta$ (see eqn. 134). In this case, the coupling of $f_0(1370)$ to $K\overline{K}$ is suppressed. The mass and width of $f_0(1370)$ from fit C are $(m, \Gamma) = (1404 \pm 10, 342 \pm 25)$ MeV/c^2, consistent with the values found in $\overline{p}p \to 3\pi^0$ [12] and $\overline{p}p \to \pi^0\eta\eta$ [13], namely $(m, \Gamma) = (1330 \pm 50, 300 \pm 80)$ MeV/c^2 and $(m, \Gamma) = (1360 \pm 35, 300 - 600)$ MeV/c^2, respectively. The relative invariant couplings of $f_0(1370)$ as a function of $a_0(1450)$ contribution are shown in figure 67. The expected value for an isoscalar $(u\overline{u}+d\overline{d})$ state (eqn. 166), assuming ideal mixing in the 0^{++} $q\overline{q}$-nonet, is given in figure 68 by the line labelled 'SU(3)'.

The production rate of $f_0(1500)$ is compared with the upper limit $B(\overline{p}p \to \pi^0 f_0(1500), f_0(1500) \to K\overline{K}) < 3.4 \times 10^{-4}$ at 95% C.L. from Gray et al. [27] which is based on the number of observed events between 2.2 GeV$^2/c^4$ and 2.4 GeV$^2/c^4$ of $m^2(K\overline{K})$ and assuming that all events are due to $f_0(1500)$. The upper limit was deduced by adding 2σ to the found value. Applying the same method to the present $\pi^0 K_L K_L$ data, one observes in the corresponding mass region $3,930 \pm 76$ events after background subtraction. From a total of 37,358 $\pi^0 K_L K_L$ events, an upper limit of

$$B(\overline{p}p \to f'\pi^0) \quad < \quad 3.3 \times 10^{-4}\,(95\%\, C.L.) \qquad (170)$$

is obtained which confirms the result of Gray et al.. However, the number of observed events is different to the number of produced events due to interferences between the partial waves. Hence, the production rate for $f_0(1500)$ may be larger than the naive upper limit given in eqn. 170, as shown in table 23.

	Fit C	Fit F1	Fit F2	Fit F3
$\frac{\gamma^2(f_0(1370)\to K\overline{K})}{\gamma^2(f_0(1370)\to\pi\pi)}$	0.31 ± 0.05	0.18 ± 0.04	0.14 ± 0.02	0.11 ± 0.02
$\frac{\gamma^2(f_0(1500)\to K\overline{K})}{\gamma^2(f_0(1500)\to\pi\pi)}$	0.37 ± 0.12	0.26 ± 0.10	0.22 ± 0.08	0.19 ± 0.07

Table 24: *Relative invariant couplings of* $f_0(1370)$ *and* $f_0(1500)$ *from different fits.*

The relative invariant coupling for $f_0(1500)$ is calculated in the same way as for $f_0(1370)$ (eqn. 167). Using the average mass of 1509 MeV/c^2 [25] for $f_0(1500)$, $B(\overline{p}p \to f_0(1500)\pi^0, f_0(1500) \to \pi^0\pi^0) = (8.1 \pm 2.8) \times 10^{-4}$ [12][25] and the break-up momenta $q_{K\overline{K}} = 0.568$ GeV/c and $q_{\pi^0\pi^0} = 0.742$ GeV/c in the corresponding decay channels of $f_0(1500)$, one obtains

$$\frac{\gamma^2(f_0(1500) \to K\overline{K})}{\gamma^2(f_0(1500) \to \pi\pi)} \quad = \quad (479.7 \pm 165.8)\, B(\overline{p}p \to f_0\pi^0, f_0 \to K\overline{K}). \quad (171)$$

Here, f_0 is $f_0(1500)$. The relative couplings from the results of fits C, F1, F2 and F3 are given in table 24. Figure 68 shows the relative coupling as a function of $a_0(1450)$ contribution in $\pi^0 K_L K_L$. The expected value for an isoscalar $(u\overline{u} + d\overline{d})$ state (eqn. 166) is given in figure 68 by the line labelled 'SU(3)'. Line A shows the relative coupling deduced from the upper limit of Gray et al. [27]. The value obtained without $a_0(1450)$ is, as for $f_0(1370)$, consistent with expectations from SU(3) couplings for an $(u\overline{u} + d\overline{d})$ state. All other results show a suppression of $f_0(1500)$ decay into $K\overline{K}$ which is even more pronounced as the $a_0(1450)$ contribution increases.

These conclusions are based on the assumption that the 0^{++} $q\overline{q}$-nonet is ideally mixed. For 7.7% expected contribution from $a_0(1450)$ a suppression of a factor of two can be achieved by tuning the mixing angle accordingly. From ref. [25] one finds $\alpha \approx 10^\circ$ and hence $\theta_{0^{++}} \approx +45^\circ$.

11 Conclusions

The results are summarized in table 25. The analysis of $\overline{p}p \to \pi^0 K_L K_L$ revealed at least two scalar ($J^{PC} = 0^{++}$) resonances $f_0(1370)$ and $f_0(1500)$ decaying into $K\overline{K}$. The branching ratios could be quantified and hence the ex-

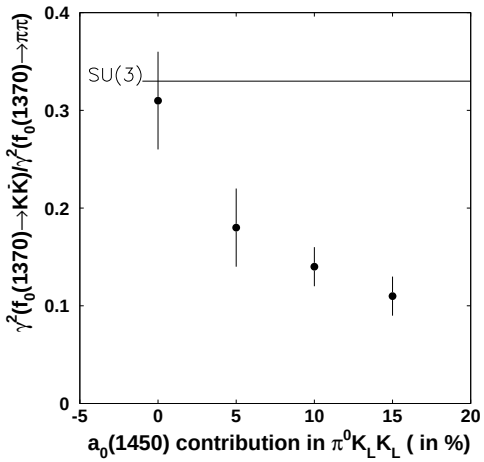

Figure 67: *Relative invariant coupling of* $f_0(1370)$ *to* $K\overline{K}$ *as a function of* $a_0(1450)$ *contributions in* $\pi^0 K_L K_L$ *. The data points are lower limits. The line gives the expected value from SU(3) for an isoscalar* $(u\overline{u} + d\overline{d})$ *state.*

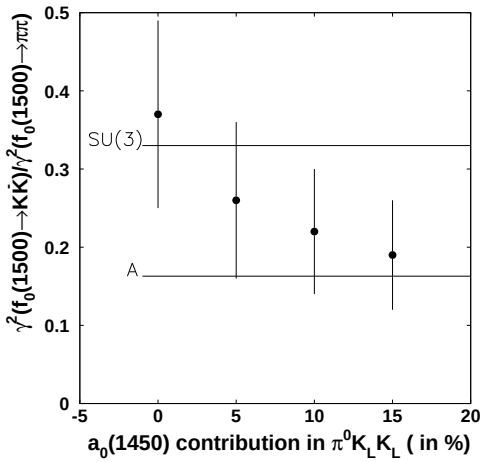

Figure 68: *Invariant relative coupling of* $f_0(1500)$ *to* $K\overline{K}$ *as a function of* $a_0(1450)$ *contributions in* $\pi^0 K_L K_L$ *. The expected coupling for an isoscalar* $(u\overline{u} + d\overline{d})$ *state is labelled with 'SU(3)'. The value obtained by the upper limit of Gray et al.[27] is given by line A.*

isting upper limit for $\overline{p}p \to \pi^0 f_0(1500), f_0(1500) \to K\overline{K}$ from Gray et al. [27] is obsolete. It is the first time that the $f_0(1500)$ has been observed in its $K\overline{K}$ decay mode. The $a_0(1450)$, recently discovered by the Crystal Barrel Collaboration [43], could neither be confirmed nor excluded, since any contribution of the expected magnitude yields the same χ^2 in the partial wave analysis of $\pi^0 K_L K_L$. However, the branching ratios $B(\overline{p}p \to \pi^0 f_0(1370), f_0(1370) \to K\overline{K})$ and $B(\overline{p}p \to \pi^0 f_0(1500), f_0(1500) \to K\overline{K})$ depend somewhat on the magnitude of $a_0(1450)$ contribution to $\pi^0 K_L K_L$.

If the $a_0(1450)$ exists and contributes the expected 7.5% to the $\pi^0 K_L K_L$ data, then the branching ratios for $f_0(1370)$ and $f_0(1500)$ are[11]

$$\begin{aligned} B(\overline{p}p(^1S_0, I=1) \to \pi^0 f_0(1370), f_0(1370) \to K\overline{K}) &= (10.0 \pm 1.3) \times 10^{-4}, \\ B(\overline{p}p(^1S_0, I=1) \to \pi^0 f_0(1500), f_0(1500) \to K\overline{K}) &= (5.0 \pm 0.5) \times 10^{-4}. \end{aligned}$$

The branching ratio for $f_0(1500)$ is close to the upper limit of 3.4×10^{-4} from Gray et al. [27]. The invariant couplings to $K\overline{K}$ relative to $\pi\pi$ are then

$$\begin{aligned} \frac{\gamma^2(f_0(1370) \to K\overline{K})}{\gamma^2(f_0(1370) \to \pi\pi)} &> (0.16 \pm 0.03), \\ \frac{\gamma^2(f_0(1500) \to K\overline{K})}{\gamma^2(f_0(1500) \to \pi\pi)} &= (0.24 \pm 0.09). \end{aligned}$$

The suppression of the $K\overline{K}$ decay for both $f_0(1370)$ and $f_0(1500)$ is consistent with a mainly $(u\overline{u} + d\overline{d})$ state in the 0^{++} $q\overline{q}$-nonet with a small deviation from ideal mixing. Hence neither $f_0(1370)$ nor $f_0(1500)$ is the scalar $s\overline{s}$ state. The masses and widths of $f_0(1370)$ and $f_0(1500)$ are:

$$\begin{aligned} f_0(1370): &\quad m = (1378 \pm 10)\ \mathrm{MeV}/c^2, \quad \Gamma = (361 \pm 25)\ \mathrm{MeV}/c^2, \\ f_0(1500): &\quad m = (1515 \pm 12)\ \mathrm{MeV}/c^2, \quad \Gamma = (104 \pm 12)\ \mathrm{MeV}/c^2, \end{aligned}$$

which are in perfect agreement with the values found from the decays into $\pi^0\pi^0$ [12][16], $\eta\eta$ [13] and $\eta\eta'$ [14] (for $f_0(1500)$).

From SU(3), the widths of the members of the 0^{++} $q\overline{q}$-nonet are ordered as $\Gamma(f_0^n) > \Gamma(a_0) \geq \Gamma(K_0^*)$ [25] where f_0^n denotes the $(u\overline{u} + d\overline{d})$ member of the

[11] These are interpolated values between 5 and 10% contribution of $a_0(1450)$ to $\pi^0 K_L K_L$.

nonet. With $\Gamma(a_0) = (270 \pm 40)$ MeV/c^2 [43] and $\Gamma(K_0^*) = 277 \pm 17$ MeV/c^2, this relation holds for $f_0(1370)$. In contrast, the $f_0(1500)$ is too narrow to fit into this picture and hence remains isolated from the 0^{++} $q\overline{q}$-nonet.

In the quarkonium-glueball mixing scheme of ref.[25], the coupling of a glueball to $K\overline{K}$ relative to $\pi\pi$ is related to the ratio ω of mass splittings between the glueball and the quarkonium states:

$$\omega \;=\; \frac{m_G - m_{n\overline{n}}}{m_G - m_{s\overline{s}}}\,,$$

where $n\overline{n} \equiv 1/\sqrt{2}(u\overline{u} + d\overline{d})$. Assuming equal couplings of gluons to non-strange and strange quarks, the ratio of invariant couplings for a glueball G is given by [25]:

$$\frac{\gamma^2(G \to K\overline{K})}{\gamma^2(G \to \pi\pi)} \;\approx\; \frac{(1+\omega)^2}{3}\,.$$

With $G = f_0(1500)$ and $n\overline{n} = f_0(1370)$, the still missing 0^{++} $s\overline{s}$ state is predicted to be at (1585 ± 20) MeV/c^2 or above 2300 MeV/c^2 since there are two solutions for ω.

This state is not observed in the present data set either because it lies at the limit of phase space or because the 0^{++} mixing angle is close to ideal. The Quark Line Rule then prevents the production of an $s\overline{s}$ state in $\overline{p}p$ annihilation.

Branching ratios		
$B(\overline{p}p(^1S_0, I=0) \to K^*(892)K)$	=	$(10.45 \pm 0.82) \times 10^{-4}$
$B(\overline{p}p(^1S_0, I=1) \to K^*(892)K)$	=	$(1.17 \pm 0.45) \times 10^{-5}$
$B(\overline{p}p(^1S_0, I=0) \to K^*(1430)K)$	=	$(5.51 \pm 0.55) \times 10^{-4}$
$B(\overline{p}p(^1S_0, I=0) \to \pi a_2(1320))$	=	$(1.55 \pm 0.31) \times 10^{-2}$
$B(\overline{p}p(^1S_0, I=1) \to \pi^0 f_2(1270))$	=	$(3.70 \pm 0.66) \times 10^{-3}$
$B(\overline{p}p(^1S_0, I=1) \to \pi^0 f_2'(1525))$	=	$(9.38 \pm 1.49) \times 10^{-5}$
$B(\overline{p}p(^1S_0) \to \pi^0 (K\overline{K})_S)$	=	$(2.1 \pm 0.2) \times 10^{-3}$
$B(\overline{p}p(^1S_0, I=1) \to \pi^0 f_0(1370), f_0(1370) \to K\overline{K})$	=	$(18.8 \pm 1.2) \times 10^{-4}$ †
$B(\overline{p}p(^1S_0, I=1) \to \pi^0 f_0(1500), f_0(1500) \to K\overline{K})$	=	$(7.7 \pm 0.5) \times 10^{-4}$ †
$B(\overline{p}p(^1S_0, I=1) \to \pi^0 f_0(1370), f_0(1370) \to K\overline{K})$	=	$(10.0 \pm 1.3) \times 10^{-4}$ ‡
$B(\overline{p}p(^1S_0, I=1) \to \pi^0 f_0(1500), f_0(1500) \to K\overline{K})$	=	$(5.0 \pm 0.5) \times 10^{-4}$ ‡
Masses and widths		
$K^{*0}(896)$: $m = (899 \pm 2)$ MeV/c^2		$\Gamma = (67 \pm 3)$ MeV/c^2
$K^*(1430)$: $m = (1423 \pm 10)$ MeV/c^2		$\Gamma = (277 \pm 17)$ MeV/c^2 §
$f_2'(1525)$: $m = (1527 \pm 5)$ MeV/c^2		$\Gamma = (99 \pm 11)$ MeV/c^2
$f_0(1370)$: $m = (1404 \pm 10)$ MeV/c^2		$\Gamma = (342 \pm 25)$ MeV/c^2 †
$f_0(1500)$: $m = (1517 \pm 12)$ MeV/c^2		$\Gamma = (96 \pm 12)$ MeV/c^2 †
$f_0(1370)$: $m = (1378 \pm 10)$ MeV/c^2		$\Gamma = (361 \pm 25)$ MeV/c^2 ‡
$f_0(1500)$: $m = (1515 \pm 12)$ MeV/c^2		$\Gamma = (104 \pm 12)$ MeV/c^2 ‡
Mixing angle of the 2^{++} $q\overline{q}$-nonet		
$\theta_{2^{++}} = (26.2 \pm 1.1)^\circ$		

†Results assuming a vanishing $a_0(1450)$ contribution.

‡Interpolated results for expected $a_0(1450)$ contribution to $\pi^0 K_L K_L$ of 7.5%.

§From the fit to the $I = 1/2$ $(K\pi)_S$ scattering data of Aston et al. [57].

Table 25: *Summary of the results from the analysis of* $\overline{p}p \to \pi^0 K_L K_L$.

References

[1] M. Gell-Mann, *Phys. Lett.* **8**(1964) 214

[2] G. Zweig, CERN preprint 8182/Th 401, unpublished

[3] Y. Ne'eman, *Nucl. Phys.* **26**(1961) 222

[4] M.Y. Han and Y. Nambu, *Phys. Rev.* **139B**(1965) 1006

[5] D.J. Gross and F. Wilczek, *Phys. Rev. Lett.* **30**(1973) 1343

[6] H.D. Politzer, *Phys. Rev. Lett.* **30**(1973) 1346

[7] S. Coleman and D.J. Gross, *Phys. Rev. Lett.* **31**(1973) 851

[8] D. Weingarten, *Nucl.Phys.* **B**(Proc.Suppl.)**34**(1994) 29

[9] M. Teper, Oxford University report OUTP-95-06P(1995), unpublished

[10] G. Bali et al., *Phys. Lett.* **B 309**(1993) 378

[11] V.V. Anisovich et al. *Phys. Lett.* **B 323**(1994) 233

[12] C. Amsler et al., *Phys. Lett.* **B 342**(1995) 433

[13] C. Amsler et al., *Phys. Lett.* **B 353**(1995) 571

[14] C. Amsler et al., *Phys. Lett.* **B 340**(1994) 259

[15] S. Resag, Proc. Hadron95, July 1995, unpublished

[16] C. Amsler et al., *Phys. Lett.* **B 355**(1995) 425

[17] T.A. Armstrong et al., *Phys. Lett.* **B 307**(1993) 399

[18] T.A. Armstrong et al., *Phys. Lett.* **B 307**(1993) 394

[19] D. Alde et al., *Phys. Lett.* **B 201**(1988) 160

[20] E. Hasan, Proc. $\overline{p}p$ Conference LEAP'94, Bled, Slovenia, 1994

[21] S. Abatzis et al., *Phys. Lett.* **B 324**(1994) 509

[22] D.V. Bugg et al., *Phys. Lett.* **B 353**(1995) 378

[23] L. Chen, Hadron91 (World Scientific 1992; S. Oneda and D. Peaslee eds.)

[24] C. Amsler, F.E. Close, *Phys. Lett.* **B 353**(1995) 385

[25] C. Amsler, F.E. Close, *Phys. Rev.* **D**, January 1996

[26] F.E. Close, *Rep. Prog. Phys.* **51**(1988) 833

[27] L. Gray et al., *Phys. Rev.* **D 27**(1983) 307

[28] D. Aston et al., *Nucl. Phys.* **B 301**(1988) 525

[29] Review of Particle Properties, *Phys Rev.* **D 50**(1994)

[30] R. Armenteros et al., *Phys. Lett.* **17**(1965) 170

[31] B. Conforto et al., *Nucl. Phys.* **B 3**(1967) 469

[32] N. Barash et al., *Phys. Rev.* **6 B**(1965) 1659

[33] E. Aker et al., *Nucl. Instr.* **A 321**(1992) 69

[34] C. Amsler et al, *Phys. Lett.* **B 358**(1995) 389

[35] C. Amsler et al, *Phys. Lett.* **B 322**(1994) 431

[36] O. Cramer, Protonium-Vernichtung in $K_S K_L$, Diplomarbeit, Universität München, 1993

[37] C. Amsler et al., *Z. Phys.* **C 58**(1993) 175

[38] Sven von Dombrowski, Proton-Antiproton Annihilation in $\omega\pi^0\pi^0$, Diplomarbeit, Universität Zürich, 1991

[39] R. Brun et al. GEANT 3, Internal Report, CERN-DD/EE/84-1, CERN, 1987

[40] C. Amsler et al., *Phys. Lett.* **B 327**(1994) 425

[41] C. Amsler et al., *Phys. Lett.* **B 311**(1993) 362

[42] R. Bizzari et al., *Nucl. Phys.* **B 27**(1971) 140

[43] C. Amsler et al., *Phys. Lett.* **B 333** (1994) 277

[44] T. Noble, A Study of Hadronic Interactions in CBGEANT, FLUKA vs GHEISHA. Crystal Barrel internal note, CB Note 258, July 1994, unpublished

[45] P.A. Aarnio et al., Fluka users guide. Technical Report TIS-RP-190, CERN, 1990.

[46] H.C. Fesefeldt, Simulation of hadronic showers, physics and applications. Technical Report PITHA 85-02, III Physikalisches Institut, RWTH Aachen, September 1985.

[47] C. Amsler et al., *Phys. Lett.* **B 319**(1993) 373

[48] M. Jacob, and G.C. Wick,, *Ann. Phys. (NY)* **7**(1959) 401

[49] D. Herndorn, P. Söding and R.J. Cashmore *Phys. Rev.* **D 11**(1975) 3165

[50] C. Amsler, J.C. Bizot, *Comp. Phys. Comm.* **30**(1983) 21

[51] I.J.R. Aitchison, *Nucl. Phys.* **A 189**(1972) 417

[52] S.U. Chung, Partial Wave analysis in K-matrix formalism, in preparation.

[53] G. Reifenröther and E. Klempt, *Phys. Lett.* **B 245**(1990) 129

[54] F. v. Hippel and C. Quigg, *Phys. Rev.* **D 5**(1972) 624

[55] S.M. Flatté et al., *Phys. Lett.* **B 38**(1972) 232

[56] D. Morgan, M.R. Pennington, *Phys. Rev.* **D 48**(1993) 1185

[57] D. Aston et al., *Nucl.Phys.* **B 296** (1988) 491

[58] C. Amsler et al., *Phys. Lett.* **B 294**(1992) 451

[59] S. Spanier, Die Beobachtung einer isovektoriellen 0^{++}-Resonanz mit einer Masse von 1470 MeV/c^2 im $\pi^0\pi^0\eta$-Endzustand der Proton-Antiproton-Vernichtung in Ruhe, Dissertation, Universität Mainz, 1994.

[60] F. James and M. Roos, CERN program Library (1989) D506

[61] C. Amsler , F. Myhrer, *Ann. Rev. Nucl. Part. Sci.* **41**(1991) 219

[62] J. Brose, Technical report on the high-statistics partial wave analysis of $\overline{p}p \to \pi^0\pi^0\pi^0$ at rest, Crystal Barrel internal note CB 255, 1994, unpublished

[63] H. Genz, *Phys. Rev.* **D 28**(1983) 1094

[64] S. Godfrey and N. Isgur, *Phys. Rev.* **D 32**(1985) 189